"Mixed-Matrix Membranes for CO_2 and H_2 Gas Separations Using
Metal-Organic Frameworks and Mesoporous Hybrid Silicas"

FINAL SCIENTIFIC/TECHNICAL REPORT

Period Covered by Report: September 2004 – August 2008

Inga H. Musselman (PI), Kenneth J. Balkus, Jr. (co-PI), John P. Ferraris (co-PI)

Date of Report: December 3, 2008

DE-FG26-04NT42173

The University of Texas at Dallas
800 West Campbell Rd. MS BE26
Richardson, TX 75080

DISCLAIMER

"This report was prepared as an account of work sponsored by an agency of the United States Government. Neither the United States Government nor any agency thereof, nor any of their employees, makes any warranty, express or implied, or assumes any legal liability or responsibility for the accuracy, completeness, or usefulness of any information, apparatus, product, or process disclosed, or represents that its use would not infringe privately owned rights. Reference herein to any specific commercial product, process, or service by trade name, trademark, manufacturer, or otherwise does not necessarily constitute or imply its endorsement, recommendation, or favoring by the United States Government or any agency thereof. The views and opinions of authors expressed herein do not necessarily state or reflect those of the United States Government or any agency thereof."

ABSTRACT

In this work, we have investigated the separation performance of polymer-based mixed-matrix membranes containing metal-organic frameworks and mesoporous hybrid silicas.

The MOF/Matrimid® and MOP-18/Matrimid® membranes exhibited improved dispersion and mechanical strength that allowed high additive loadings with reduced aggregation, as is the case of the 80 wt% MOP-18/Matrimid® and the 80% (w/w) Cu-MOF/Matrimid® membranes. Membranes with up to 60% (w/w) ZIF-8 content exhibited similar mechanical strength and improved dispersion.

The H_2/CO_2 separation properties of MOF/Matrimid® mixed-matrix membranes was improved by either keeping the selectivity constant and increasing the permeability (MOF-5, Cu-MOF) or by improving both selectivity and permeability (ZIF-8). In the case of MOF-5/Matrimid® mixed-matrix membranes, the H_2/CO_2 selectivity was kept at 2.6 and the H_2 permeability increased from 24.4 to 53.8 Barrers. For the Cu-MOF/Matrimid® mixed-matrix membranes, the H_2/CO_2 selectivity was kept at 2.05 and the H_2 permeability increased from 17.1 to 158 Barrers. These two materials introduced porosity and uniform paths that enhanced the gas transport in the membranes. When ZIF-8/Matrimid® mixed-matrix membranes were studied, the H_2/CO_2 selectivity increased from 2.9 to 4.4 and the permeability of H_2 increased from 26.5 to 35.8 Barrers. The increased H_2/CO_2 selectivity in ZIF-8/Matrimid® membranes was explained by the sieving effect introduced by the ZIF-8 crystals (pore window 0.34 nm) that restricted the transport of molecules larger than H_2.

Materials with microporous and/or mesoporous cavities like carbon aerogel composites with zeolite A and zeolite Y, and membranes containing mesoporous ZSM-5 showed sieving effects for small molecules (e.g. H_2 and CO_2), however, the membranes were most selective for CO_2 due to the strong interaction of the zeolites with CO_2. For example, at 30 wt% ZSM-5 loading, the CO_2/CH_4 selectivity increased from 34.7 (Matrimid®) to 56.4. The large increase in selectivity was the result of the increase in CO_2 permeability from 7.3 (Matrimid®) to 14.6 Barrers. At 30 wt% ZSM-5 loading, the H_2/CH_4 separation was also improved from 83.3 (Matrimid®) to 136.7 with an increase in H_2 permeability from 17.5 (Matrimid®) to 35.3 Barrers. The 10% carbon aerogel-zeolite A and -zeolite Y composite/Matrimid® membranes exhibited an increase in the CO_2/CH_4 separation from 34.7 to 71.5 (zeolite A composite) and to 57.4 (zeolite Y composite); in addition, the membrane exhibited an increase in the CO_2/N_2 separation from 33.1 to 50 (zeolite A composite) and to 49.4 (zeolite Y composite), indicating that these type of materials have affinity for CO_2. The inclusion of mesoporosity enhanced the dispersion of the additive allowing loadings of up to 30% (w/w) without the formation of non-selective voids.

TABLE OF CONTENTS

EXECUTIVE SUMMARY

Alternative materials for the preparation of mixed-matrix membranes (MMMs) for gas separation were synthesized and tested using Matrimid® as the common polymer matrix. Nanocrystals of metal-organic frameworks (MOFs), such as MOF-5, Cu-MOF, and Cu-BPY-HFS, were synthesized under mild conditions in gram quantities with highly reproducible properties, such as size, surface area, and crystallinity, which arose from the activation of these materials after their synthesis. Activation was important to expose the sorption sites of the crystals to the gases tested in separation (also applicable to gas storage). The scalability of the synthesis procedures of these materials to industrial levels encourages the exploration of these additives in gas separation in large scales. Similarly, the synthesis and the sieving properties of the zeolitic imidazolate framework 8 (ZIF-8) was achieved in gram quantities with the potential to be scaled up to commercial levels. A soluble crystal called metal-organic polyhedra 18 (MOP-18) was also synthesized in gram quantities under similar conditions as the MOFs and ZIF-8. The advantage introduced by this material is the improved dispersion of the unit cells in the polymer matrix that allows for fast and improved membrane preparation. Carbon nanotubes were also studied as additives for mixed-matrix membranes due to their uniform interior surface that facilitates the diffusion of molecules, especially hydrogen; to achieve this goal, the nanotubes were cut and functionalized with carboxylic acid. Although MOFs, ZIF-8, and MOP-18 introduce organic functionality to improve their dispersion, inorganic materials with different functionalities to improve polymer/additive interaction were also studied. In this regard, mesoporous ZSM-5, periodic mesoporous organosilicas, and carbon aerogel were synthesized to exploit the mesoporous cavities for polymer chain penetration to improve contact. In addition to the previous strategy, carbon aerogel and zeolite A and zeolite Y composites were prepared to introduce meso and microporosity simultaneously. A material with both characteristics could have better polymer wetting (mesopores) and size selective (micropores) properties.

The research efforts of our membrane group have focused on forming and evaluating novel membranes containing the microporous MOF nanocrystals previously mentioned (e.g. MOF-5, MOP-18, ZIF-8, Cu-MOF, and Cu-BPY-HFS), the nanoporous molecular sieving materials (e.g. carbon molecular sieves (CMS) and zeolites), and single-walled carbon nanotubes (SWNTs), dispersed in a Matrimid® polymer matrix. The preparation of membranes containing MOF, ZIF-8, and MOP-18 crystals was less laborious and faster than the preparation of the membranes containing inorganic additives; however, in both cases the particle/polymer interaction was strong due to the organic character of the MOF or the availability of mesoporous sites in the inorganic additives that allowed good contact. The MOF-containing mixed-matrix membranes were mechanically more robust and more processable allowing high loadings of the materials in the polymer matrix. Up to 80 wt% MOP-18/Matrimid® mixed-matrix membranes were prepared with improved additive dispersion that showed no signs of aggregation or large defects. Similarly, high Cu-MOF loadings were achieved (80% w/w) demonstrating that the incorporation of organic functionalities in frameworks improves dispersion in a polymer matrix. In the case of the inorganic materials (PMOs, zeolites, carbon aerogels, and carbon aerogel zeolite composites), the maximum additive loading achieved was 30% (w/w) before

embrittlement made difficult their manipulation and characterization. The mechanical resistance of these membranes was similar to those containing MOFs, ZIF-8, or MOP-18.

Permeation experiments of pure gases at 2 atm and 35 °C with MOF-5 and ZIF-8 MMMs showed that the effect of having these materials in the membrane is the increased separation performance for H_2/CO_2 by either increasing the flux of the gases and keeping the selectivity constant (Matrimid[®] $H_2/CO_2 = 2.7$, $H_2 = 24.4$ Barrers; 30% w/w MOF-5/Matrimid[®] $H_2/CO_2 = 2.6$, $H_2 = 53.8$ Barrers) or by increasing both the selectivity and the permeability (Matrimid[®] $H_2/CO_2 = 2.9$, $H_2 = 26.5$ Barrers; 60% w/w ZIF-8/Matrimid[®] $H_2/CO_2 = 4.4$, $H_2 = 35.8$ Barrers). In the case of MOF-5, the increased permeability comes from the porosity introduced by the MOF-5 crystals in the membrane, while in the case of ZIF-8 the sieving effect of the crystals (pore size 0.34 nm) rejected the transport of molecules larger than H_2. Separation of gas mixtures of H_2/CO_2 at different feed ratios showed that the membranes are selective for H_2. In the case of the 30% w/w MOF-5/Matrimid[®] membrane, the H_2/CO_2 separation ranged from 2.1 to 2.3 which was close to the selectivity of the pure polymer (2.3 to 2.5). For the 60% w/w ZIF-8/Matrimid[®] membrane, the separation of the H_2/CO_2 gas mixtures increased to 7.0, a 180% increase in selectivity over the pure polymer that brought the mixed-matrix membrane above the Robeson upper bound.

Cu-MOF/Matrimid[®] MMMs show results similar to MOF-5 MMMs. When the loading of Cu-MOF reached 30% (w/w), the selectivity of the H_2/CO_2 mixtures remained constant at 2.05 but the permeability of H_2 increased from 17.1 Barrers (Matrimid[®]) to 158 Barrers, a 9 fold increase in permeability that put the membrane above the Robeson upper bound. The remarkable improvement in the gas transport properties of the Cu-MOF MMMs relies on the good dispersion and wetting of the crystals by the polymer matrix that minimizes the formation of non-selective voids leaving the pores of the crystals accessible to gas molecules.

Materials with microporous and/or mesoporous cavities like carbon aerogel composites with zeolite A and zeolite Y, and membranes containing mesoporous ZSM-5 showed sieving effects for small molecules (e.g. H_2 and CO_2), however, the membranes were most selective for CO_2 due to the strong interaction of the zeolites with CO_2. For example, at 30 wt% ZSM-5 loading, the CO_2/CH_4 selectivity increased from 34.7 (Matrimid[®]) to 56.4. The large increase in selectivity was the result of the increase in CO_2 permeability from 7.3 (Matrimid[®]) to 14.6 Barrers. At 30 wt% ZSM-5 loading, the H_2/CH_4 separation was also improved from 83.3 (Matrimid[®]) to 136.7 with an increase in H_2 permeability from 17.5 (Matrimid[®]) to 35.3 Barrers. The 10% carbon aerogel-zeolite A and -zeolite Y composite/Matrimid[®] membranes exhibited an increase in the CO_2/CH_4 separation from 34.7 to 71.5 (zeolite A composite) and to 57.4 (zeolite Y composite); in addition, the membrane exhibited an increase in the CO_2/N_2 separation from 33.1 to 50 (zeolite A composite) and to 49.4 (zeolite Y composite), indicating that these type of materials have affinity for CO_2.

With the incorporation of the studied materials, the selectivity for other important mixtures was also studied. In some cases, the selectivity for a specific gas was increased, e.g. methane in the case of the Cu-MOFs and CO_2 in the case of the carbon aerogels. For instance, the gas mixture separation of 20% (w/w) Cu-BPY-HFS/Matrimid[®] showed that the CH_4/N_2 separation for the mixed gases increased to 1.7, while the ideal selectivity was 1.16. The selectivity of CO_2/CH_4 decreased from 34 to 20, much lower than the ideal selectivity of 27.6 for CO_2/CH_4. As for the separation of other gas mixtures, there was

not a large difference compared with pure Matrimid$^{®}$, which suggests the Cu-BPY-HFS has no affinity towards H_2 or CO_2 but an increased affinity for CH_4.

The dispersion of additives and the phase separation between the inorganic/organic components was addressed with the introduction of MOP-18, which is a metal-organic polyhedra functionalized with alkyl chains that is soluble in organic solvents. The solubilization of MOP-18 made it possible to overcome the dispersion of the aggregates and, at the same time, to improve the affinity between the additive and the polymer thus minimizing phase separation. This functionalization, and the inherent affinity of the MOP-18 for the polymer, made it possible to obtain membranes with MOP-18 loadings as high as 80% (w/w) with good mechanical strength. The superior dispersion of MOP-18 was taken to the limits preparing membranes with loadings up to 80 wt% without aggregation or formation of defects in the membrane. Another advantage introduced by the functionalized MOP-18 is the increased processability of the material; membranes can be easily made by eliminating tedious and long dispersion procedures. Although the MOP-18/Matrimid$^{®}$ MMMs are not selective for H_2, they exhibited an interesting improved selectivity for C_3H_6/N_2 (Matrimid$^{®}$ C_3H_6/N_2 = 1.6; 80% w/w MOP-18/Matrimid$^{®}$ C_3H_6/N_2 = 5.79) by increasing the permeability of C_3H_6 from 0.39 (Matrimid$^{®}$) to 3.40 (80% w/w MOP-18/ Matrimid$^{®}$).

The following manuscripts have been submitted to/accepted by journals during the period covered by this report:

Zhang, Y.; Musselman, I. H.; Ferraris, J. P.; Balkus Jr., K. J., "Mixed-matrix membranes composed of Matrimid$^{®}$ and mesoporous ZSM-5 nanoparticles", *J. Membr. Sci.* **2008**, 325, 28.

Zhang, Y.; Musselman, I. H.; Ferraris, J. P.; Balkus Jr., K. J., "Gas permeability properties of Matrimid$^{®}$ membranes containing the metal-organic framework Cu-BPY-HFS", *J. Membr. Sci.* **2008**, 313, 170.

Zhang, Y.; Musselman, I. H.; Ferraris, J. P.; Balkus Jr., K. J., "Gas permeability properties of mixed-matrix Matrimid$^{®}$ membranes containing a carbon aerogel: A material with both micropores and mesopores", *Ind. Eng. Chem. Res.* **2008**, 47, 2794.

Perez, E. V.; Balkus Jr., K. J.; Ferraris, J. P.; Musselman, I. H., "Mixed-matrix membranes containing MOF-5 for gas separations", *J. Membr. Sci.*, in press.

Zhang, Y.; Musselman, I. H.; Ferraris, J. P.; Balkus, Jr., K. J., "Gas permeability properties of Matrimid$^{®}$ membranes containing the periodic mesoporous organosilicas", *Separations Sci. Tech.*, submitted.

Zhang, Y.; Musselman, I. H.; Ferraris, J. P.; Balkus, Jr., K. J., "Mixed matrix membranes containing carbon aerogel-zeolite composites", *Ind. Eng. Chem.*, submitted.

Ordoñez, J.; Ferraris, J. P.; Balkus, Jr., K. J.; Musselman, I. H., "Gas permeability and selectivity properties of ZIF-8/Matrimid$^{®}$ mixed-matrix membranes", in preparation.

Perez, E. V.; Ferraris, J. P.; Balkus Jr., K. J.; Musselman, I. H., "Copper based metal-organic framework (Cu-MOF) mixed-matrix membranes for gas separation", in preparation.

Perez, E. V.; Ferraris, J. P.; Balkus Jr., K. J.; Musselman, I. H., "Metal-organic polyhedra (MOP-18) mixed-matrix membranes for gas separation", in preparation.

REPORT DETAILS

Experimental methods

Materials

Biphenyl-4,4'-dicarboxylic acid (BPDA, 97%), triethyldiamine (TED, 98%), triethylamine (TEA, 98%), diethylformamide (DEF, 98%), $Zn(NO_3)_2 \cdot 6H_2O$, $Zn(NO_3)_2 \cdot 4H_2O$, HNO_3, 4-methylacetophenone, 2-methylimidazole (H-MeIM), sodium bicarbonate (99.5%), potassium carbonate (98%), 1-iodododecane (98%), 5-hydroxyisophthalic acid (97%), tetraethylorthosilicate (TEOS), tetrapropylammonium hydroxide (TPAOH), sodium hydroxide, cetyltrimethylammonium bromide (CTABr), resorcinol (99.9%) formaldehyde (36-38% in water, methanol-stabilized), tetramethylammonium hydroxide, sodium carbonate (99%), single-walled carbon nanotube functionalized with carboxylic acid groups (SWNT: 80-90% purity, carboxylic acid content: 3-6 atom%, diameter×length=4-5 nm×500-1500 nm, total impurities 5-10% metals), nitric acid, Cu (II) tetrafluoroborate, ammonium hexafluorosilicate, 4,4'-bypyridine, octadecyltrimethylammonium chloride (ODTMA), polyoxyethylene(10) stearyl ether (Brij 76), bis(triethoxysilyl)ethylene(BTE), bis(triethoxysilyl)methylene (BTEM), bis(triethoxysilyl)ethenylene(BTEE), 1,4-bis(triethoxysilyl) benzene(BTEB), and copper acetate monohydrate ($Cu(OAc)_2 \cdot H_2O$, >99%) were obtained from Aldrich and used without further treatment. Benzene-1,4-dicarboxylic acid (BDA, >99%) and formic acid (98% formic acid, 2% H_2O) were received from Fluka and used as received. Concentrated sulfuric acid was obtained from Mallinckrodt. Ethyl acetate (99.8%), acetonitrile (99.8%), and potassium hydroxide (>85%) were purchased from EM Science. Ethyl ether (99.9%), hexanes (95% n-hexanes), and hydrochloric acid were obtained from J. T. Baker and used without further treatment. HPLC grade water was obtained from Fisher and used as received. Molecular sieves 4A 4-8 mesh (Sigma-Aldrich) were washed with HPLC grade water, activated at 400 °C for 1 d, cooled to room temperature in a vacuum oven at low pressure, and stored in capped bottles filled with nitrogen for later use. Methanol (99.9%, HPLC grade), 1-heptanol (97%), ethanol, chloroform (99.9%, H_2O <0.002%), acetone (99.7%, H_2O = 0.3%), and toluene (99.8%, H_2O = 0.010%) were purchased from Fisher; *N,N*-dimethylformamide (DMF, 99.8%, H_2O <0.15%) and ethanol were obtained from EMD. All organic solvents were dried over activated molecular sieves 4A for 1 d before use. Matrimid® 5218 was purchased from Ciba Polymers (Hawthorne, New York). It was dried at 240° C in a vacuum oven for 1 d and stored in nitrogen before use. Matrimid® 5218 is a commercially available polyimide, made from the monomers 3,3′,4,4′-benzophenone tetracarboxylic dianhydride and diaminophenylindane, and is currently used as a gas separation membrane material. For membrane casting, Mylar® A92 sheets were purchased from Active Industries. For the permeation experiments, nitrogen, oxygen, hydrogen, methane, carbon dioxide, and their certified mixtures H_2/CO_2 (75/25, 50/50, 25/75), CH_4/N_2 (94/6, 50/50, 25/75), CH_4/CO_2 (90/10, 50/50, 25/75) were obtained from Air Liquide. The purity of the gases was greater than 99.5% for CH_4 and O_2; the rest of the gases were greater than 99.99% pure. Propylene (99.9%) and propane (99.9%) were acquired from Applied Gas Inc.; the certified 50/50 propylene/propane mixture was acquired from Matheson Tri-Gas.

Synthesis of MOF-5

Metal-organic framework 5 (MOF-5) nanocrystals were synthesized in gram quantities by modifying published procedures [1-3] to control the water content in the reaction mixture. This procedure can be easily scaled up to larger quantities. In a typical synthesis, 4.00 g (13.50 mmol) of $Zn(NO_3)_2 \cdot 6H_2O$ was dissolved in 250 mL of DMF in a round bottom flask. To remove the excess water adsorbed by the zinc salt, 12.8 g of activated 4A molecular sieves 4-8 mesh were added to the DMF solution. After drying for 1 h, the molecular sieves were removed and then BDA (1.30 g, 7.80 mmol) was added to the DMF solution. The solution was heated to 70 °C and, under strong agitation, TEA (5.05 g, 50.50 mmol) was added drop wise over the course of 10 min to produce a white precipitate; the solution was then left to react for 10 min and cooled to room temperature while stirring continuously. As-synthesized MOF-5 nanocrystals were obtained by filtering the white solution and then washing the white powder with 3 x 30 mL of DMF. The white powder was dried for 1 d at 80 °C in a vacuum oven at low pressure. Activated MOF-5 nanocrystals were obtained by filtering and washing the powder with a continuous flow of 3 x 30 mL each of DMF, CHCl₃, and acetone in that order. The activated material was dried in a vacuum oven at 240 °C for 1 d at low pressure. MOF-5 was recovered (2.2 g, 80% yield based on Zn) and stored in a capped vial filled with nitrogen

Synthesis of Cu-MOF

Cu-MOF nanocrystals were synthesized in gram quantities by modifying published procedures [4, 5] to control the water content in the reaction mixture, to reduce the synthesis time, and to improve reproducibility. The new procedure can be easily scaled up to larger quantities. In a typical synthesis, a 100 mL ethanol solution containing 1.75 g (8.8 mmol) of copper acetate was stirred at room temperature until the copper acetate dissolved. Then, 30 g of activated 4A (4-8 mesh) molecular sieves were added to the solution. After drying for 1 h, the molecular sieves were removed and the solution was capped for further use. A second solution consisting of 1.05 g (9.20 mmol) of TED in 90 mL of toluene was dried with 10 g of activated 4A (4-8 mesh) molecular sieves. After drying for 1 h, the molecular sieves were removed. A third solution made of 2.00 g (8.60 mmol) of BPDA and 2.6 mL of formic acid in 200 mL of DMF was heated to 110 °C in a 500 mL round bottom flask until the BPDA was dissolved. The solution was then cooled to room temperature. To remove the excess of water introduced by the formic acid, 1.5 g of activated 4A (4-8 mesh) molecular sieves was added to the solution. After drying for 1 h, the molecular sieves were removed and the solution was refluxed at 110 °C with strong agitation until the BPDA dissolved. Once the DMF solution reached 110 °C, the ethanol solution was added all at once and immediately followed by the toluene solution. The final solution was heated to 110 °C with refluxing and stirring for 30 h with the condenser open to atmosphere. The resulting blue solution was then cooled to room temperature. As-synthesized Cu-MOF nanocrystals were obtained by filtering the blue solution and then washing the blue cake with 3 x 50 mL of DMF. The cake was dried for 1 d at 80 °C in a vacuum oven. Activated Cu-MOF nanocrystals were obtained by filtering and washing the cake with a continuous flow of 3 x 50 mL each of DMF, CHCl₃, acetone, and CHCl₃ in that order.

The activated material was dried in a vacuum oven at 90 °C for 1 d and then cooled to room temperature under a blanket of nitrogen before being removed from the vacuum oven. Activated

Cu-MOF (2.8 g) was recovered and stored in a capped vial filled with nitrogen.

In order to detect the presence of a possible 2D phase mixed with the 3D phase of the Cu-MOF, the same procedure was repeated but at a lower temperature (50 °C) and without the addition of the TED solution. A similar procedure was reported by Mori et al. in the synthesis of 2D copper terephthalate crystals [6].

Synthesis of MOP-18

MOP-18 nanocrystals were synthesized in gram quantities following the procedure described by Furukawa et al. [7]. In a typical synthesis, a 100 mL DMF solution containing 2.7 g (7.6 mmol) of 5-dodecoxyisophthalic acid was stirred at room temperature until the acid dissolved. A second solution consisting of 1.5 g (7.6 mmol) of copper acetate in 50 mL of DMF was stirred until the copper acetate dissolved completely. The solution containing the organic acid was added at once to the copper solution with stirring (1 min) until the final solution was mixed. A blue precipitate formed immediately, which was allowed to crystallize for 1 d at room temperature in a sealed container. The solvent was decanted and 50 mL of DMF was added and then decanted after 1 h; to finish washing the crystals, two 50 mL aliquots of methanol were added to the crystals and each was decanted after 1 h. The blue precipitate was filtered, washed with methanol, and then dried at 60° C in a vacuum oven for 1 d yielding 2.3 g of blue MOP-18 crystals.

Synthesis of ZIF-8

A solid mixture of $Zn(NO_3)_2 \cdot 4H_2O$ (3.1 g) and 2-methylimidazole (H-MeIM) (0.96 g) was dissolved in 60 mL of DMF in a round bottom flask. Once the solution was heated to 100 ^{o}C, triethylamine was added. The resulting solution was further heated and allowed to reflux at 140 ^{o}C for 6-8 h. The solution was filtered and washed with successive 50 mL portions of DMF, $CHCl_3$, and MeOH. The crystals were air dried for 20 min and put in the vacuum oven at 240 ^{o}C overnight.

Synthesis of mesoporous ZSM-5

The synthesis of mesoporous ZSM-5 followed a procedure similar to that previously reported [8]. A gel with the molar ratio of SiO_2:0.28 TPAOH:0.00625 Al_2O_3:36 H_2O was prepared and stirred for 2 h at room temperature. Then, the gel was transferred to a 23 ml Teflon liner (autoclave) and aged at 110 °C for 2 h to give a clear solution which was cooled to room temperature. Water, sodium hydroxide, and CTABr were added to yield a final synthesis gel having the molar ratio SiO_2:0.28 TPAOH:0.12 CTABr:0.5 NaOH:0.00625 Al_2O_3:118 H_2O. After stirring for 2 h at room temperature, the synthesis mixture was transferred to a Teflon lined autoclave and heated at 150 °C for 8 h. The resulting solid was collected by filtration, dried in air, and calcined at 550 °C for 6 h to remove the organic template. MCM-48 was prepared using a synthesis mixture having the molar ratio of SiO_2: 0.12 CTABr:0.5 NaOH:0.00625 Al_2O_3:118 H_2O [8]. The gel was stirred at room temperature for 2 h then transferred to an autoclave and heated at 150 °C for 8 h. After cooling to RT, the product was filtered and dried at 110 °C overnight, followed by calcination at 550 °C for 6 h to remove the organic template.

Synthesis of carbon aerogel

Carbon aerogels were synthesized through polycondensation of resorcinol with formaldehyde catalyzed by sodium carbonate [9]. In a typical synthesis, 6.0 g resorcinol, 16.52 g formaldehyde, and 0.031 g sodium carbonate were dissolved in 7.59 mL deionized water under stirring. After thermal curing (1 d at room temperature, 1 d at 50 °C, and 3 d at 90 °C), a red resorcinol-formaldehyde polymer gel was obtained. Then the wet gel was introduced into acetone for 3 d to exchange the water inside the pores, fresh acetone was changed each day. The gels were dried at room temperature under ambient pressure, and further pyrolyzed at 800 °C under an argon atmosphere, and thus transformed into carbon aerogels. The obtained carbon aerogels were in a monolithic form.

Synthesis of carbon aerogel, carbon aerogel-zeolite composites

Carbon aerogel-zeolite A composite: The reaction mixture with composition (molar basis) 3.165 $Na_2O : Al_2O_3 : 1.926 SiO_2 : 128 H_2O$ was made [10]. Pre-dried monolithic carbon aerogel was added into the precursor. The mixture was heated in an autoclave at 100°C for 12 h. After hydrothermal treatment, the carbon aerogel+zeolite A composite was washed and dried it in vacuum oven at 200°C for 48 h. The final product was a monolithic carbon aerogel-zeolite A composite.

Carbon aerogel-zeolite Y composite: The pre-dried monolithic carbon aerogel was added into the reaction mixture with composition (molar basis) $4.62 Na_2O : Al_2O_3 : 10 SiO_2 : 180 H_2O$ [10] and heated in an autoclave at 100°C for 24 h. Final product was washed with water and dried in a vacuum oven at 200°C for 48 h. The final product was the monolithic carbon aerogel-zeolite Y composite.

Functionalization and shortening of SWNTs (SWNT-short)

Purified single-wall carbon nanotubes were used as the starting material to make short SWNTs functionalized with carboxylic acid groups. The procedure to shorten the SWNT was modified from the methods in ref 40 and 41. First, 70 mg SWNT was added to a 200 mL acid mixture (75 % vol 99 wt% H_2SO_4 and 25%vol 70 wt% HNO_3) and sonicated in a water bath for 30 h at RT. After sonication, the 200 mL mixture was diluted to 800 mL. The solution was then centrifuged at 3000 rpm for 30 min to recover the SWNT. After decanting the supernatant, the SWNT-short was collected and washed with 1M NH_4HCO_3 solution to neutraling. To test the solubility of SWNT-short, 10 mg SWNT-short was dissolved in water and centrifuged at 15000 rpm for 2 h. No apparent separation was achieved.

Synthesis of Cu-BPY-HFS

In a typical synthesis, 0.30 g $Cu(BF_4)_2$ and 0.178 g $(NH_4)_2SiF_6$ were dissolved in 10.0 g water and 0.312 g 4,4'-bypyridine was dissolved in 10 g DMF. The DMF solution was added to the water solution with stirring at RT. Purple crystals precipitated immediately. After 30 min, the powder was centrifuged and washed with water, acetone, and chloroform sequentially. The final product was dried at 50 °C under vacuum.

Synthesis of PMOs

The synthesis of mesoporous benzene silica (MBS) followed a procedure similar to that previous reported [11]. In a typical synthesis, ODTMA (16.665 g, 47.88 mmol) was dissolved in a mixture of DI

water (500g) and 6M sodium hydroxide (NaOH) aqueous solution (40g, 200 mmol NaOH) at 50-60 °C. BTEB (20 g, 49.67 mmol) was added to the ODTMA solution with vigorous stirring at room temperature. The mixture was treated ultrasonically for 20 min to disperse the hydrophobic BTEB in the aqueous solution, and stirred for 20 h at room temperature. The solution was kept at 95 °C for 20 h under static conditions. The resulting white precipitate was recovered by filtration and drying to yield as-made mesoporous benzene−silica (8.22 g). The surfactant was removed by stirring 1.0 g of as-synthesized material in 250ml of ethanol with 9 g of 36% HCl aqueous solution at 70°C for 8h to yield mesoporous benzene−silica (0.69 g).

The synthesis of periodic mesoporous organosilicas (PMOs) followed a procedure similar to that previously reported [12]. In a typical synthesis, 0.40 g Brij 76 was added into the mixture of 1.31 ml concentrated HCl (12.2 M) and 18.69 ml deionized water. The mixtures were loaded into a polypropylene bottle and kept at 50 °C for 12 h. The organosilane precursor was then added to the resulting clear solution under stirring to make the reactant molar ratios as follows: 0.11 Brij 76: 222 H_2O: 3.20 HCl: 0.56 organosilane. The synthesis mixtures were covered and stirred at 50 °C for 12 h, followed by heating at 90 °C under static conditions for an additional 24 h. The white powders were recovered by suction filtration and air-dried. The as-synthesized product must be extracted with acidified ethanol to produce mesoporous organosilicas. Composites were placed in excess (350 ml/g) acidified ethanol (1 M HCl) and refluxed for 12 h. The products were recovered by filtration, washed with absolute ethanol, and dried under vacuum at 60 °C for 10 h. The extraction procedure was repeated twice to remove organic template.

Instrumentation

SEM images were acquired using a FEG LEO-1530 scanning electron microscope. Samples for SEM analysis were coated with Au-Pd using a Denton Vacuum Desk II sputter coater. XRD patterns were obtained with a Rigaku Ultima III X-ray diffractometer using $Cu_{K\alpha}$ X-ray radiation. IR spectra were collected using a Nicolet Avatar 360 FTIR E.S.P. spectrophotometer equipped with a single-bounce attenuated total reflectance (ATR) accessory. Thermal analyses were performed on a Perkin-Elmer Pyris 1. Differential scanning calorimetry (DSC) was carried out at a heating rate of 10 °C/min under nitrogen protection. Mechanical properties were determined at room temperature on a Perkin-Elmer DMA 7e. Tensile testing was performed on a Favimat Textechno instrument to obtain the Young's modulus and tensile strength of the membranes.

Membrane Fabrication
MOF-5/Matrimid® mixed-matrix membranes

Flat 0, 10, 20, and 30% (w/w) activated MOF-5/Matrimid® mixed-matrix membranes were fabricated. Two solutions were prepared by dissolving 0.50 g of Matrimid® in 4.50 g of $CHCl_3$ and by dispersing 0.05 g (10%), 0.10 g (20%), or 0.15 g (30%) of activated MOF-5 in 4.5 g of $CHCl_3$. The two solutions were bath sonicated for 4 h and stirred for 1 d and then were mixed by pouring the polymer solution into the MOF-5 solution. The combined solution was stirred and bath sonicated for 1 more hour and then

concentrated by purging the excess solvent with a stream of nitrogen until the polymer/CHCl$_3$ concentration reached 10% w/w.   In a laminar flow hood, an AccuLab Jr.™ Drawdown casting table with rod 2.5 was used to cast the membranes onto Mylar$^®$ A92 films.   The freshly cast membranes were immediately covered with a watch glass to slow solvent evaporation.   After 30 min, the watch glass was removed to allow the solvent to evaporate completely.   When dried, the membranes were removed from Mylar$^®$ and then annealed in a vacuum oven at 240 °C and low pressure for 1 d.   After annealing, the membranes were stored in a desiccator filled with nitrogen.   The average membrane thickness was 35 μm.

Cu-MOF/Matrimid$^®$ mixed-matrix membranes

Flat 0, 10, 20, 30, 40, 50, and 80% (w/w) activated Cu-MOF/Matrimid$^®$ mixed-matrix membranes were fabricated.   Two solutions were prepared by dissolving 0.40 g of Matrimid$^®$ in 4.50 g of CHCl$_3$ and by dispersing 0.04 g (10%), 0.08 g (20%), 0.12 g (30%), 0.16 g (40%), 0.20 g (50%), or 0.32 g (80%) of activated Cu-MOF in 2.5 g, 5.5 g, 8.5 g, 10.5 g, 12.5 g, or 20.0 g of CHCl$_3$, respectively.   The two solutions were stirred for 2 h, bath sonicated for 2 h, and then mixed by pouring the Cu-MOF solution into the polymer solution.   The combined solution was stirred for 1 more hour and then concentrated by purging the excess solvent with a stream of nitrogen until the polymer/CHCl$_3$ concentration reached 10%.   In a laminar flow hood, an AccuLab Jr.™ Drawdown casting table with rod 2.5 was used to cast the membranes onto Mylar$^®$ A92 films.   The freshly cast membranes were immediately covered with a watch glass to slow solvent evaporation.   After 3 h, the membranes were removed from Mylar$^®$ and then annealed in a vacuum oven at 100 °C and low pressure for 1 d.   After annealing, the membranes were cooled to room temperature at low pressure in the lapse of 5 h.   The membranes were stored in a desiccator filled with nitrogen. The average membrane thickness was 60 μm.

MOP-18/Matrimid$^®$ mixed-matrix membranes

Flat 0%, 30%, 50%, 80% (w/w) and 80 wt% MOP-18/Matrimid$^®$ mixed-matrix membranes were fabricated.   Two solutions were prepared by dissolving 0.22 g of Matrimid$^®$ in 3.00 g of CHCl$_3$ and by dissolving 0.06 g (30%), 0.11 g (50%), or 0.16 g (80%) of MOP-18 in 1.6 g, 1.9 g,   or 2.5 g of CHCl$_3$, respectively.   For the 80 wt% loading the two solutions consisted of 0.05 g of Matrimid$^®$ and 0.21 g of MOP-18 both dissolved in 1.00 g and 3.10 g of CHCl$_3$, respectively.   The two solutions were independently stirred for 1 h and then the MOP-18 solution was added to the polymer solution.   The combined solution was stirred for 0.5 hour and then concentrated by purging the excess solvent with a stream of nitrogen until the polymer/CHCl$_3$ concentration reached 10%.   In a laminar flow hood, an AccuLab Jr.™ Drawdown casting table with a doctor blade was used to cast the membranes onto Mylar$^®$ A92 films.   The freshly cast membranes were immediately covered with a watch glass to slow solvent evaporation.   After 0.5 h, the membranes were removed from Mylar$^®$ and then annealed in a vacuum oven at 100 °C for 1 d.   After annealing, the membranes were cooled to room temperature at low pressure over the course of 5 h. The membranes were stored in a desiccator filled with nitrogen.   The average membrane thickness of the 23 and 33 wt% MOP-18 loading was 22 μm and for the 45 and 80 wt% was 74 μm.

ZIF-8/Matrimid® mixed-matrix membranes

ZIF-8/Matrimid® mixed-matrix membranes [0%, 20%, 30%, 40%, 50% and 60% (w/w)] were fabricated by solution blending.   Two solutions, Matrimid® (0.50 g) and ZIF-8 [0.10 g (20%), 0.15 g (30%), 0.20 g (40%), 0.25 g (50%), 0.30 g (60%)] in chloroform (5 mL), were prepared separately. These solutions were stirred and bath sonicated alternately for 24 h to obtain a homogenous suspension. The ZIF-8 crystals were first "primed" or coated by adding a small amount, approximately 20%, of the Matrimid® solution to the ZIF-8 solution, after which it was further stirred and bath sonicated for another 24 h.   After thorough mixing, the remaining bulk polymer solution was added.   The chloroform solvent was evaporated to obtain the desired solution viscosity (approximately 10% w/w) for membrane casting.   Membranes were cast in a Pure Aire© laminar flow hood onto a Mylar® (Mylar® A92 film) covered glass substrate using an AccuLab Jr.™ Drawdown casting table with a 2.5 μm wire wound rod.   The resulting membrane was immediately covered with a watch glass, and was allowed to dry slowly in ambient air overnight.   The membrane was then peeled off the Mylar® and annealed in a vacuum oven at 240 °C for overnight.

ZSM-5/Matrimid® mixed-matrix membranes

Calcined mesoporous ZSM-5 was ground in a mortar and vacuum-dried at 120 °C for 1 d. The mesoporous ZSM-5 powder was slurried into 1,1,2,2-tetrachloroethane (TCE) and sonicated for 4 h before the addition of Matrimid® powder to form a 10% (w/w) solution. Mixed-matrix membranes were then formed using 10, 20, and 30% (w/w) suspensions of mesoporous ZSM-5 in the Matrimid® solution. To adequately disperse the mesoporous ZSM-5 particles within the Matrimid® matrix, the suspensions were stirred and sonicated for several 30-min periods until a homogeneous suspension was observed. For a 10% (w/w) mesoporous ZSM-5/Matrimid® composite, a typical preparation consisted of adding 0.015 g of Matrimid® in 1.35 g of TCE, with stirring and sonicating for 4 hours at room temperature. The 0.020 g of Matrimid® was then added with stirring and sonicating for 4 h at room temperature. The suspension was stirred for 30 min and then bath sonicated for 30 min. After seven additional periods of stirring and sonicating, 0.115 g of Matrimid® (total: 0.135g) were added to the suspension and stirred overnight at RT. A final 30-min sonication period was completed before casting to remove any trapped air bubbles. Membranes were cast in a laminar flow hood (PureAire) onto a glass substrate using an AccuLab Jr. Drawdown casting table with a wire wound rod (AccuLab Jr. #80). Membrane thicknesses were determined using SEM. Cross sections were prepared by freeze-fracturing the membranes after several minutes of immersion in liquid N_2. SEM images were acquired from the surfaces and cross-sections of the membranes.

Carbon aerogel/Matrimid® mixed-matrix membranes

The carbon aerogel was ground using a wig-l-bug ball mill and vacuum-dried at 120 °C for 1 day. The carbon aerogel powder was then placed into 1,1,2,2-tetrachloroethane (TCE) and sonicated for 1 h to disperse the fine powder. Then, Matrimid® polymer was added to form a 10% (w/w) solution. Mixed-matrix composite membranes were formed using 10, 20, and 30% (w/w) suspensions of the carbon aerogel in the Matrimid® solution. To adequately disperse the carbon aerogel particles within the Matrimid® matrix, the suspensions used for the preparation were stirred and sonicated for several 10-min

periods until a homogeneous suspension was observed. For a 10% (w/w) carbon aerogel/ Matrimid®
composite, a typical preparation consisted of adding 0.015 g of carbon aerogel in 1.35 g of TCE with
stirring and sonicating for 1 h at room temperature. Next, 0.135 g of Matrimid® polymer was stirred into
the solution. The suspension was stirred for 10 min and then bath sonicated for 10 min. After five
additional iterations of stirring and sonicating, the mixture was stirred at RT overnight. A final 30-min
sonication was completed before casting to remove any trapped air bubbles. Membranes were cast in a
laminar flow hood (PureAire) onto a glass substrate using an AccuLab Jr. Drawdown casting table with
a wire wound rod (AccuLab Jr. #80). The membrane thickness was determined using optical microscopy.
Cross-sections were prepared by freeze-fracturing the membranes after several minutes of immersion in
liquid N_2.

Carbon aerogel-zeolite/Matrimid® mixed-matrix membranes

Calcined carbon aerogel was ground using a mechanic ball mill, then vacuum-dried at 120 °C for 1
day. The carbon aerogel powder was put into 1,1,2,2-tetrachloroethane (TCE) and sonicated for 1 hour
to disperse the fine powder. Then Matrimid® polymer was added to form a 10% (w/w) solution.
Mixed-matrix composite membranes were then formed using 10, 20, and 30% (w/w) suspensions of
carbon aerogel in the Matrimid® solution. To adequately disperse the carbon aerogel particles within the
Matrimid® matrix, the suspensions used for the preparation were stirred and sonicated for several 10-min
periods until a homogeneous suspension was observed. For a 10% (w/w) carbon aerogel/Matrimid®
composite, a typical preparation consisted of adding 0.015 g of carbon aerogel in 1.35 g of TCE, stirring
and sonicating for 1 h at room temperature. Next, 0.135 g of Matrimid® polymer was stirred into the
solution. The suspension was stirred for 10 min and then bath sonicated for 10 min. After five additional
iterations of stirring and sonication, the mixture was stirred overnight. A final 30-min sonication period
was completed before casting to remove any trapped air bubbles, which could cause the formation of
nonselective pores.

Membranes were cast in a laminar flow hood (PureAire) onto a glass substrate using an AccuLab Jr.
Drawdown casting table with a wire wound rod (AccuLab Jr. #80). Membrane thickness for calculation
of gas permeability was determined using optical microscopy. Cross sections were prepared by
freeze-fracturing the membranes after several minutes of immersion in liquid N_2.   SEM images were
acquired from the surfaces and cross sections of the membranes.

Functionalized SWNT/Matrimid® mixed-matrix membranes

Both SWNT-COOH and SWNT-short were more soluble in NMP than in other solvents. To
adequately disperse the SWNTs within the Matrimid® matrix, the SWNT-NMP solution was sonicated
for more than 4 h to de-bundle the SWNTs. For a 3.6% (w/w) SWNT-Matrimid® composite, a typical
preparation consisted of dissolving 0.005 g of SWNT in 1.5 g of NMP, then stirring and sonicating for 4
h at room temperature. Next, 0.135 g of dried Matrimid® was stirred into the NMP solution. The solution
was stirred for 30 min to dissolve the polymer then stirred and sonicated for 2 h. Then, a final 30-min
sonication was completed to remove any trapped air bubbles, which could cause the formation of
nonselective pores.

Membranes were cast in a laminar flow hood (PureAire) onto a glass substrate using an AccuLab Jr.

Drawdown casting table with a wire wound rod (AccuLab Jr. #80). After casting, the wet membrane was transferred to a pre-heated 70°C vacuum oven to dry. After 1 h, the dry membrane was removed from the glass and transferred to a pre-heated 200 °C oven for 2d to remove the organic solvent and also to anneal the polymer. Membrane thickness for the calculation of gas permeability was determined using optical microscopy. Cross-sections were prepared by freeze-fracturing the membranes after several minutes of immersion in liquid N_2. SEM images were acquired from the surfaces and cross-sections of the membranes.

Cu-BPY-HFS/Matrimid® mixed-matrix membranes

The Cu-BPY-HFS powder was slurried into chloroform and sonicated for 1 h to disperse the fine powder. Then, Matrimid® polymer was added to form a 10% (w/w) solution. Mixed-matrix membranes were formed using 10, 20, and 30% (w/w) suspensions of Cu-BPY-HFS in the Matrimid® solution. To adequately disperse the Cu-BPY-HFS particles within the Matrimid® matrix, the suspensions used for the preparation were stirred and sonicated for several 10-min periods until a homogeneous suspension was observed. For a 10% (w/w) Cu-BPY-HFS/Matrimid® composite, a typical preparation consisted of adding 0.015 g of Cu-BPY-HFS in 1.35 g of chloroform, stirring, and sonicating for 1 h at room temperature. Next, 0.135 g of Matrimid® polymer was stirred into the solution. The suspension was stirred for 10 min and then bath sonicated for 10 min. After five additional iterations of stirring and sonication, the mixture was stirred for overnight. Then, a final 30-min sonication period was completed before casting to remove any trapped air bubbles, which could cause the formation of nonselective pores.

Membranes were cast in a laminar flow hood (PureAire) onto a glass substrate using an AccuLab Jr. Drawdown casting table with a wire wound rod (AccuLab Jr. #80). After casting, the membranes were dried in vacuum oven at 50 °C for at least 3 d to remove the solvent. The membrane thickness was determined using optical microscopy. Cross-sections were prepared by freeze-fracturing the membranes after several minutes of immersion in liquid N_2. SEM images were acquired from the surfaces and cross sections of the membranes.

PMOs/Matrimid® mixed-matrix membranes

The periodic mesoporous organosilca powder was ground in a mortar and vacuum-dried at 120 °C for 1 day. The PMO powder was stirred into 1,1,2,2-tetrachloroethane (TCE) and sonicated for 4 hours before the addition of Matrimid® powder to form a 10% (w/w) solution. Mixed-matrix membranes were then formed using 10, 20, and 30% (w/w) suspensions of PMO in the Matrimid® solution. To adequately disperse the PMO particles within the Matrimid® matrix, the suspensions were stirred and sonicated for several 30-min periods until a homogeneous suspension was observed. For a 10% (w/w) PMO/Matrimid® composite, a typical preparation consisted of adding 0.015 g of PMO in 1.35 g of TCE, with stirring and sonicating for 4 hours at room temperature. The 0.020 g of Matrimid® was then added with stirring and sonicating for 4 hours at room temperature. The suspension was stirred for 30 min and then bath sonicated for 30 min. After seven additional periods of stirring and sonicating, 0.115 g of Matrimid® (total: 0.135g) were added to the suspension and stirred overnight at RT. A final 30-min sonication period was completed before casting to remove any trapped air bubbles. Membranes were

cast in a laminar flow hood (PureAire) onto a glass substrate using an AccuLab Jr. Drawdown casting table with a wire wound rod (AccuLab Jr. #80). Membrane thicknesses were determined using SEM. Cross sections were prepared by freeze-fracturing the membranes after several minutes of immersion in liquid N_2. SEM images were acquired from the surfaces and cross sections of the membranes.

Permeability Studies

Separations of gas blends (50%/50% H_2/CO_2, 90%/10% CH_4/CO_2, and 94%/6% CH_4/N_2) and single-gas permeabilities for H_2, O_2, N_2, CO_2, and CH_4 were evaluated using a custom-built gas permeameter [13, 14]. The permeameter consists of a stainless steel permeation cell which separates upstream and downstream pressure transducers (MKS Instruments). This cell exposes a membrane area of 0.97 – 2.0 cm^2 to the gas. All valve actuation and pressure monitoring were conducted using LabView 7.1 software (National Instruments). After evacuating both sides of the membrane for several hours, the upstream side of the membrane was pressurized to approximately 2000 Torr with a single gas. The upstream and downstream pressures were recorded every second for 2 h. The steady-state slope of downstream pressure versus time was determined from the raw data. The time lag (θ, -intercept/slope) and diffusivity (D, $L^2/6\theta$) were calculated from the steady-state slope. The permeability was evaluated from 3θ to 7θ, and the solubility was calculated using the equation $S = P/D$. The percent relative error between successive runs for each gas was between 0.2 and 5.6%. For the determination of the composition of the mixed gas permeates, an on-line residual gas analyzer (MKS PPT-200) was used. The RGA unit is controlled by a computer and consists of a quadrupole mass spectrometer (1 to 200 amu) with a Faraday cup. The working pressure range of the RGA is $1x10^{-10}$ to $1x10^{-4}$ Torr. The RGA was evacuated to $8x10^{-9}$ Torr before the analysis of the permeate.

RESULTS AND DISCUSSION

MOF-5/Matrimid® mixed-matrix membranes

To maximize the interaction between the gas molecules and the MOF sorption sites, only batches of activated MOF-5 nanocrystals that showed high surface area (2500 – 3000 m^2/g) were used for the fabrication of mixed-matrix membranes with 10, 20, and 30% (w/w) loading. X-ray diffraction patterns of activated MOF-5/Matrimid® mixed-matrix membranes were acquired before and after permeability experiments. In all cases, the diffraction patterns revealed the presence of only one phase corresponding to MOF-5 (see, for example, Figure 1d). It should also be noted that the relative intensities of the reflections of the MOF-5 in the polymer remained the same ($I_{9.6°}$ = 20% $I_{6.7°}$) as those measured for the pure activated MOF-5 material.

Thermogravimetric analyses of activated MOF-5/Matrimid® membranes (see, for example, Figure 2c) indicated that there was no loss of weight up to 350 °C (temperature of crystal decomposition) indicating that casting solvent was not trapped in the pores of the MOF-5 nanocrystals. The polymer decomposed above this temperature.

Figure 3 shows an optical image of a Matrimid® membrane cast from CHCl$_3$ and Figure 4 shows an SEM image of its cross-section. Figure 5 shows the surface and cross-sections of 10, 20, and 30% (w/w) MOF-5/Matrimid® mixed-matrix membranes. SEM images of the membrane surfaces (Figures 5a, d, g) and cross-sections (Figures 5b, e, h) indicate that there are no gross defects; however, agglomerates of MOF-5 are evident in the polymer. The membrane cross-section morphology reveals the formation of circular cavities and polymer veins (elongated matrix segments) with increased plastic deformation of the polymer (Figures 5c, f, i). This morphology is an indication of a strong contact/interaction between the polymer and the walls of the MOF-5 nanocrystals, although it is not strong enough to break the agglomerates and keep them dispersed at the primary nanoparticle level. Debonding of the agglomerates from the matrix may be occurring during freeze fracture resulting in the formation of cavities [15, 16]. Rigidification of the polymer-additive interface is also expected as a result of the strong interaction of the additive and the matrix, limiting the mobility of the polymer chains [15-17].

Single gas permeation experiments showed that the permeability of all gases increased with MOF-5 loading. For example, at 30% loading the permeability of the resulting membrane increased 120% with respect to the pure polymer cast from the same solvent and tested under the same conditions (our experimental Matrimid® permeability values listed in Table 1 agree well with published values [18]). In the case of H$_2$, an increase in permeability from 24.4 Barrers (Matrimid®) to 53.8 Barrers (30% (w/w) MOF-5/Matrimid®) was achieved suggesting that the MOF-5 crystals were facilitating gas transport (Table 1). Since the permeabilities of all the gases increased proportionally, the ideal selectivities remained unchanged (Table 2). For example, the H$_2$/CO$_2$ separation of pure Matrimid® cast from

CHCl$_3$ was 2.70 (P_{H_2} = 24.4 Barrers, P_{CO_2} = 9.0 Barrers) and, at 30% (w/w) MOF-5 loading, the

H$_2$/CO$_2$ separation was 2.66 (P_{H_2} = 53.8 Barrers, P_{CO_2} = 20.2 Barrers). A plot of the facilitation

ratios versus the kinetic diameters of the gases (Figure 6) showed that the ratios increased only with an

increase in the MOF-5 loading.   To test its resistance to higher pressures, a 20% MOF-5/ Matrimid[®] membrane was run at 3 atm and 35 °C. The permeabilities of the gases tested were identical to the permeabilities of the membrane run at 2 atm and 35 °C ($P_{H_2}^{2\ atm}$ = 33.3 Barrers, $P_{H_2}^{3\ atm}$ = 33.1 Barrers,

$P_{CO_2}^{2\ atm}$ = 12.6 Barrers, $P_{CO_2}^{3\ atm}$ = 11.9 Barrers, $P_{O_2}^{2\ atm}$ = 2.6 Barrers, $P_{O_2}^{3\ atm}$ = 2.6 Barrers, $P_{N_2}^{2\ atm}$ = 0.4

Barrers, $P_{N_2}^{3\ atm}$ = 0.4 Barrers, $P_{CH_4}^{2\ atm}$ = 0.32 Barrers, $P_{CH_4}^{3\ atm}$ = 0.32 Barrers).   The results also suggest that the membrane is free of non selective voids.

Gas diffusivities (average of 2 membranes) of CO_2, O_2, N_2, and CH_4 (Figure 7) increased with MOF-5 loading; up to 100% increase in diffusivity was observed at 30% MOF-5 loading (D_{CO_2} from

0.44 ± 0.04 to 1.02 ± 0.07 x 10^{-8} cm^2 s^{-1}, D_{O_2} from 0.94 ± 0.30 to 1.60 ± 0.07 x 10^{-8} cm^2 s^{-1}, D_{N_2}

from 0.19 ± 0.01 to 0.33 ± 0.03 x 10^{-8} cm^2 s^{-1}, and D_{CH_4} from 0.06 ± 0.01 to 0.12 ± 0.01 x 10^{-8} cm^2 s^{-1}).

The increase in diffusivity can be explained by the porosity introduced by the MOF-5 and by its pore window (0.8 nm), which is larger than the kinetic diameters of the gases tested.   In addition to the MOF porosity, the availability of a more uniform surface (crystal wall or linker) for surface diffusion could help to increase the diffusivity of the gases in the membrane.

Compared to pure Matrimid[®], MOF-5/Matrimid[®] mixed-matrix membranes showed no significant change in solubility with increased MOF-5 loading (Figure 8).   In the case of CO_2, O_2, N_2, and CH_4, the solubility remained essentially unchanged regardless of the MOF-5 loading (S_{CO_2} from 20.70 ± 1.90 to

19.90 ± 0.05 x 10^{-2} cm^3_{stp} cm^{-3} cmHg, S_{O_2} from 2.20 ± 0.90 to 2.50 ± 0.12 x 10^{-2} cm^3_{stp} cm^{-3} cmHg,

S_{N_2} from 1.30 ± 0.26 to 1.60 ± 0.02 x 10^{-2} cm^3_{stp} cm^{-3} cmHg, and S_{CH_4} from 3.80 ± 1.30 to 3.70 ±

0.23 x 10^{-2} cm^3_{stp} cm^{-3} cmHg).   These results indicate that the MOF-5 nanocrystals have no significant affinity for CO_2, O_2, N_2, and CH_4 at the temperature and feed pressure used in this study (35° C and 2 atm).   These results agree with Sholl's simulated adsorption isotherms of CO_2, CH_4, and N_2 in MOF-5 which show no significant increase in gas adsorption up to 3-4 atm. [19]; only CO_2 adsorption increases at pressures above 3 atm. Therefore, the experimental solubility trends obtained by the time lag method can be considered valid for the gases tested, excluding H_2.   It can be concluded, therefore, that the permeability of the gases is enhanced by their increase in diffusivity in the membrane owing to the porosity of the MOF-5. Another example of a non selective material is MCM-41, which increases the diffusivities but not the solubilities of the gases [13].

Although MOF-5 was reported to be a good material for the storage of H_2 [20], selective sorption of gas mixtures in MOFs was not measured until this work for MOF-5 in MMMs.   Permeation experiments with blends of gases showed that the separation of H_2/CO_2 in a 30% MOF-5/Matrimid[®] mixed-matrix membrane did not increase at any feed ratio compared to the separation of the mixtures

performed with the pure polymer (Matrimid® H_2/CO_2 = 2.4, 30% MOF-5/Matrimid® H_2/CO_2 = 2.2). However, the CH_4/N_2 and the CO_2/CH_4 separations showed a selectivity improvement for CH_4 of 15% and 20%, respectively, at a 50/50 feed composition (Table 3). The increased selectivity for methane can be explained in terms of the extended dual mode transport model for gas mixtures that assumes that the primary effect of the presence of more than one gas in the membrane results in the competition between these gases for the fixed unrelaxed free volume in the polymer [21]. Also, the Henry's sorption coefficient of a gas is assumed to be independent of the presence of other components. From this model, it can be concluded that, due to the large solubility of CO_2 in the membrane (S_{CO_2} = 20.00,

S_{CH_4} = 1.20 x10^{-2} cm$^3_{stp}$ cm^{-3} cmHg), the solubility of CH_4 is greatly reduced, rendering CH_4 transport

dependent mostly on diffusivity, which is enhanced by the porosity and the uniform surface introduced by the MOF-5 nanocrystals. In addition, the incorporation of MOF-5 reduced the sorption sites in the polymer for CO_2 which contributed to the reduction of CO_2 transport. Pure glassy polyimide, however, showed a different result with increased CO_2 selectivity over CH_4 at different CO_2/CH_4 feed ratios [22]. The increased CO_2 selectivity resulted from an increased CO_2 solubility and a longer residence time of the gas in the polymer leading to a reduced diffusivity of CH_4. Overall, CO_2 dominated the competition for sorption sites in the polymer matrix.

Cu-MOF/Matrimid® mixed-matrix membranes

The simulated X-ray diffraction pattern of Cu-MOF presented by Seki [4, 5] was used as a reference to verify the nature of the synthesized crystals (Figure 9a). X-ray diffraction of as-synthesized, semi-activated, and activated Cu-MOF nanocrystals (Figure 9b,c,d respectively) confirmed that both materials were Cu-MOF crystals and that the presumed 2D phase (Figure 9f,g), that results from the exposure to moisture or from an incomplete reaction, was not present. Similarly to MOF-5, [23-25] X-ray diffraction of Cu-MOF shows differences in the intensities of the first five main reflections between the as-synthesized, semi-activated, and activated crystals. For the as-synthesized Cu-MOF nanocrystals, the main reflections at 2θ = 5.70°, 10.70°, and 11.60° are more intense than the rest of the reflections and have similar intensities; additionally the reflection at 2θ = 9.05° is not present. When the crystal is fully activated, the reflection at 2θ = 5.70° is still the most intense of all the reflections and the rest of the reflections have intensities less than 20% of the intensity of the main reflection [intensity at 2θ = 8.20° ($I_{8.20°}$ = 6.5% $I_{5.70°}$), 9.05° ($I_{9.05°}$ = 14.0% $I_{5.70°}$), 10.80° ($I_{10.80°}$ = 7.7% $I_{5.70°}$), and 11.60° ($I_{11.60°}$ = 18.3% $I_{5.70°}$)]; additionally the positions of the reflections at 2θ = 8.20° and 9.05° are slightly shifted. It is believed that guest molecules occupy the pores of the as-synthesized crystals, like in the case of MOF-5, [3, 24] causing a destructive interference in the XRD pattern and that, through activation, these molecules are removed causing a reverse in the peak intensities. These observations of peak intensity shifts have been correlated to measured surface areas and thermogravimetric analysis results.

Nitrogen sorption isotherms obtained with as-synthesized (Figure 10a), semi-activated (Figure 10b), and activated Cu-MOF crystals (Figure 10c) were used to calculate BET surface areas and HK pore sizes. The surface area of the crystals ranges from 400 m²/g to 2200 m²/g for the as-synthesized and

semi-activated crystals to 3000 m^2/g for the fully activated crystals.

Thermogravimetric analysis of the possible 2D phase shows no weight loss up to 300 °C (Figure 11a). The as-synthesized Cu-MOF nanocrystals showed that up to 20% of material is lost at 200 °C, which is attributed to trapped solvent in the pores and to coordination solvent. The maximum temperature the crystals support before decomposition is 300 °C; above this temperature the crystals collapse and decompose (Figure 11b). Activated Cu-MOF nanocrystals followed a similar trend except that weight loss begins at 300 °C owing to crystal decomposition (Figure 11c). The TGA of the 3% Cu-MOF/Matrimid® membrane shows that, up to 340 °C, the membrane does not lose weight suggesting that casting solvent was not present in the pores of the crystals (Figure 11d). Figure 11e shows the TGA of pure Matrimid® as a reference; the polymer is stable up to 450 °C.

Single gas permeation experiments show that the permeability of the gases increased rapidly as the content of the Cu-MOF increased (Table 4). Even at low Cu-MOF loadings of 9 and 17 wt%, the permeabilities of all the gases increased by more than 100% and 400%, respectively, (Table 5), retaining the selectivity of the membrane for some gas pairs and at the expense of a reduction in selectivity for gas pairs involving CH$_4$ or N$_2$ (Table 6). This reduction in selectivity can be readily explained by the affinity of the Cu-MOF for CH$_4$ and by the quadrupole interaction of N$_2$ with the SBU of the MOF crystal that increases the transport of these less permeable gases in the membrane. The rapid increase in the permeabilities of the gases at these low loadings can be explained by the uniform porosity introduced by the Cu-MOF nanocrystals that increased the available volume through which molecules could diffuse; in addition, the more uniform path for molecular diffusion provided by the crystal walls diminished the tortuosity the gas molecules encountered when diffusing through polymer chains. Armatas [26] concluded that gas transport in porous materials is strongly influenced by the size of the pore, the connectivity of the pores, the variability of the pore size, and the tortuosity the molecules experience in the pores. The combination of these factors, when applied to microporous materials, helps to explain why the permeabilities of the gases in Cu-MOF/Matrimid® MMMs increase sharply. The model [26] indicates that the diffusion of gases in microporous materials is independent of the connectivity of the pores, but highly affected by the inhomogeneity of the pore size, which introduces a high level of tortuosity. In the case of the 45 wt% Cu-MOF loading, the high permeabilities experienced by the gases suggest that the Cu-MOF crystals have a narrow pore size distribution and that the pores of the MOF are uniform, minimizing the tortuosity experienced by the gas molecules.

Although the previous model explains well the permeability of the Cu-MOF/Matrimid® MMMs, it remains possible that defects formed at the MOF/polymer interface that contributed to the large gas permeabilities. To determine whether this defective structure was present, two experiments were conducted. The first experiment consisted of filtering a solution of fluorescein (~1 nm) in acetone through the 45 wt% Cu-MOF/Matrimid® membrane for 2 h. In this experiment, the face of the membrane exposed to fluorescein was at atmospheric pressure and the other side at reduced pressure. If the membrane had defects, then the solution should have flowed through the membrane. However, this did not happen suggesting that defects, if present, were no larger than 1 nm, the size of fluorescein. To further investigate fluorescein diffusion into the membrane, a laser scanning confocal microscope was used to image both surfaces of the membrane. No fluorescence was observed which indicated that the probe did not diffuse into the membrane. Details of this technique applied to membrane

characterization are described by Tsapatsis et al. [27, 28].   Another piece of membrane was immersed in a fluorescein/acetone solution for 1 week.   Still, no fluorescence was detected at the surfaces that could indicate diffusion of the probe into the membrane.

Ideal selectivities of the gases showed a monotonic decrease with increasing Cu-MOF loading above 17 wt%.   Below this loading, the selectivity of the membranes remained unchanged suggesting that the polymer was still dominating the separation.   At Cu-MOF loadings above 17 wt%, the selectivities started to decrease except for CH_4/N_2, C_3H_6/N_2, and C_3H_8/N_2 which exhibited a gradual increase.   The increase in the selectivity for some of these gas pairs is an indication that the interaction of the gas with the crystal walls/SBU is greater than with the polymer.   This interpretation lead us to conclude that surface diffusion of the organic vapors is taking place on the walls of the crystal which is supported by the increase in the solubility of the gases.   This assumption is reasonable since, at high MOF loadings, most of the potential interaction sites of the polymer chains are already in contact with the MOF crystals and are not available to interact with the penetrants, thereby reducing the presence of the penetrants in the polymer matrix.

Gas mixture separation of binary components (Table 7) supports our premise that the membranes with high Cu-MOF loading (45 wt%) are free of defects.   Defects in the membrane would result in a loss of selectivity with results close to 1.   In Table 7, the selectivities of the membranes for gas mixtures of H_2/CO_2 show values similar to the pure polymer, but for the CH_4/N_2 separation the selectivity increases from 1 to 2 (Knudsen = 1.3) at 45 wt% Cu-MOF loading with a CH_4/N_2 feed of 50/50 indicating that the membrane is interacting with the gas molecules.

MOP-18/Matrimid® mixed-matrix membranes

The 30, 50, and 80% (w/w) MOP-18/Matrimid® membranes retained much of their flexibility and mechanical resistance as can be seen from the optical image in Figure 12.   This remarkable strength of the membrane indicates a strong interaction between the MOP-18 and the polymer suggesting the formation of successful mixed-matrix membranes.   The high flexibility of the 80% MOP-18/Matrimid® membrane suggests that as the loading of the MOP-18 increases the role of the polymer matrix changes from a support material for the crystals to a binding entity that "glues" the crystals together.   In the case of the 80 wt% MOP-18/Matrimid® membrane, embrittlement made it difficult to test the material but it was still possible to remove the membrane from the casting substrate and manipulate it.   SEM images of the surfaces and cross-sections of a Matrimid® membrane and 30, 50, 80% (w/w), and 80 wt% MOP-18/Matrimid® mixed-matrix membranes are shown in Figures 13 and 14, respectively.   The surfaces of the MMMs showed no aggregation of the crystals as the loading of MOP-18 increased, as is commonly seen with zeolites and to a less extent with some MOFs in MMMs.   The surfaces of the membranes, even at very high loadings, remained smooth and free from gross defects, an indication of good dispersion and wetting of the crystals in the polymer matrix.   The low magnification SEM images of the membrane cross-sections (Figure 13) show no macroscopic morphology or aggregation of the MOP-18 crystals, even at the highest loading of 80 wt%, which is remarkable considering the large area of the sample visualized in Figure 13 (approximately 140 µm x 85 µm).   High magnification SEM images of the cross-sections revealed that as the loading of MOP-18 increases, the polymer/crystal

phases are indistinguishable suggesting an even distribution of the crystals in the matrix; however, small, uniform, and evenly distributed granules (< 100 nm) can be seen and no morphology associated with the polymer phase can be detected. Instead, the granules seem to represent a new phase composed of both MOP-18 crystals and polymer. The 80 wt% MOP-18/Matrimid® membrane cross-section shows a more continuous phase with the presence of evenly distributed granules (<100 nm) that could be made by polymer coating of the MOP-18 crystals. The more continuous phase could be the morphology of the MOP-18 phase since it became the more abundant face in the membrane.

X-ray diffraction patterns of the MOP-18/Matrimid® membranes (Figure 15) were acquired for the 50, 80% (w/w), and 80 wt% MOP-18 loadings to examine the possibility of recrystallization of the MOP-18 unit cells into nanocrystals. In all cases, no diffraction pattern was detected which supports the assumption that the MOP-18 unit cells were well dispersed in the matrix.

Thermogravimetric analyses of the MOP-18/Matrimid® membranes (see, for example, Figure 16) indicate that there is no loss of weight up to 300 °C confirming that casting solvent was completely removed from the membrane and that it was not trapped in the pores of the MOP-18 unit cells. TGA also indicates that the polymer chains may have stabilized the unit cells to a higher temperature (50 °C above the temperature of unit cell decomposition). Above 300 °C, the unit cells decomposed completely and the membrane followed the polymer decomposition path.

Single gas permeation experiments showed that the permeability of the gases increased proportionally as the content of MOP-18 increased (Table 8). However, from the calculation of the facilitation ratios (Table 9), the permeabilities of the more condensable gases, like methane and propylene, were enhanced more than the rest of the gases tested. The relatively small increase of hydrogen permeability could be an indication of the reduction of polymer free volume due to the interaction of the MOP-18 unit cells with the polymer. Additionally, the increased tortuosity introduced by the alkyl chains of MOP-18 could have restricted the diffusion of hydrogen in the membrane, limiting its mobility. An interesting scenario is observed when the loading of MOP-18 reaches 80% (w/w). At this loading, the increase in the permeability of H_2, CO_2, O_2, and N_2 is almost negligible (with respect to the 50% MOP-18 loading) and the only gases that experience an increase in permeability are CH_4, C_3H_6, and C_3H_8, probably owing to their organic character which facilitates their interaction with the walls of the unit cells (on the surface of the unit cells). The 10 fold increase in the permeability of C_3H_6 versus the 5 fold increase of the permeability of C_3H_8 could be explained by the presence of non filled coordination sites in the MOP-18 SBU (the copper paddle wheel cluster that has one vacant coordination site on each copper atom) that could interact more strongly with the propylene double bond enhancing the solubility of this gas in the membrane.

Table 10 shows that the ideal selectivities of CH_4/N_2 (1.62) and C_3H_6/N_2 (5.79) increase considerably when compared to the pure polymer (CH_4/N_2 = 0.92, C_3H_6/N_2 = 1.61), and are far from the Knudsen values (CH_4/N_2 = 1.32, C_3H_6/N_2 = 0.81), indicating the gas transport follows the solubility/diffusivity model. Again, for these two gases, the increased selectivity can be explained by their increased organic character and, in the case of C_3H_6, by the interaction of the double bond with uncoordinated sites in the MOP-18 SBU. The H_2/CH_4 separation shows an accelerated decrease in selectivity due to two combined effects, the increased tortuosity that reduces the permability of H_2 and the increased permeability of CH_4 in the membrane.

When the diffusivity and solubility of the gases was analyzed, it was seen that the diffusivity of the gases increases as the loading of MOP-18 increases.   In the case of CH_4, the diffusivity increases 4 fold but its solubility remains constant for all MOP-18 loadings.   However, the diffusivity of C_3H_6 remains unchanged with the MOP-18 loadings, but its solubility increases 8 fold.   Indeed, it can be said that this is the only gas that experiences an increase in solubility with the increase of MOP-18 loading.   The fact the diffusivity of C_3H_6 does not increase even at 80% (w/w) MOP-18 suggests that the membrane is free of defects or voids larger than the kinetic diameter of C_3H_6 (0.45 nm); it can be concluded, therefore, that any potential voids or defects in the membrane are smaller than 0.45 nm, otherwise the diffusivity of C_3H_6 would have increased significantly.

Gas mixture separation of binary components shows that the membrane is more selective for CH_4 in the CO_2/CH_4 and CH_4/N_2 separations (Table 11).   For the CH_4/N_2 separation, the competition for the sorption sites in the membrane could be dominated by CH_4 leading to an increased flux of this gas and simultaneously a reduction in N_2 solubility.   In the case of CO_2/CH_4, the separation is still dominated by CO_2, but a large decrease in selectivity for CO_2 is observed (50% less), which supports the idea that CH_4 is effectively competing for the sorption sites in the membrane.

ZIF-8/Matrimid® mixed-matrix membranes

The ZIF-8 material (Figure 17) was synthesized using a hydrothermal method producing nanometer-sized crystals ranging in diameter from 70 to 200 nm.   Nanometer-sized crystal synthesis of ZIF-8 material was achieved by adding a base, triethylamine (TEA), in the synthesis procedure (Figure 18).   The XRD patterns of the as-synthesized ZIF-8 with and without the addition of TEA, both match the theoretical pattern calculated for ZIF-8.   The addition of TEA did not change the crystallinity of the ZIF-8 as evidenced by the XRD plots of ZIF-8 synthesized with and without TEA.   Immediate washing of as-synthesized ZIF-8 with DMF, $CHCl_3$, and MeOH was carried out to activate the material by displacing guest molecules from the pores so that they would be available to absorb gas molecules or penetrants.   After the solvent exchange, the ZIF-8 nanocrystals were dried under vacuum at 240 °C for overnight.   TGA analysis of as-synthesized ZIF-8 nanocrystals, revealed a ~10% weight loss starting at 150 °C and plateauing at 300 °C, that was attributed to the presence of residual solvent or guest molecules in ZIF-8.   Between 400 °C and 500 °C, the decomposition of the ZIF-8 material occurs. The activated and annealed ZIF-8 material showed no immediate weight% loss until 400 °C, indicating that it was free from guest molecules.   The TGA plot also showed that the activated ZIF-8 material was thermally stable up to 400 °C, and that framework decomposition occurs in the range of 400-500 °C, which was similar to literature observations [29].   The pore size and surface area of the nanocrystals were determined by N_2 adsorption at 77 K on ZIF-8 that was washed with DMF, $CHCl_3$, and MeOH. Multipoint BET (1300 m^2/g) and Langmuir (1500 m^2/g) surface areas were obtained.   An Argon (Ar) adsorption analysis was also performed and obtained a BET surface area of 1200 m^2/g and a Langmuir surface area of 1500 m^2/g.   Infrared spectroscopy of ZIF-8 show peaks at 3135, 2928, 1580, 1459, 1422, 1383, 1308, 1176, 1145, 994, 952, 759, 693, 421 cm^{-1}.   The absorption band at 3135 cm^{-1} is for the C=C stretch, 2928 cm^{-1} is for the C-H aliphatic stretch of the imidazole, and 1580 cm^{-1} is for the C=N stretch.   The C-N adsorption bands are found on the 1100-1400 cm^{-1} region.   The absorption band at

421 cm^{-1} is associated with the stretching of the Zn-N.   The obtained spectrum correlates well with the literature data [29].

Using CHCl$_3$ as the solvent, the ZIF-8 nanocrystalline material was cast into mixed-matrix membranes (0%, 20%, 30%, 40%, 50% and 60% w/w loadings) with Matrimid® as the polymer matrix. XRD plots (Figure 19) acquired from the mixed-matrix membranes showed that the crystallinity of the ZIF-8 material was still intact after membrane fabrication and annealing.   SEM images (Figure 20) were acquired from the surfaces and cross-sections of the membranes with different ZIF-8 loadings. The surface images showed the incorporation of the ZIF-8 particles into the polymer matrix, wherein there was increased particle content with increased loading.   However, the ZIF-8 nanocrystals tended to aggregate into sub-micrometer particles that were evenly dispersed in the polymer.   The SEM images of the membrane cross-sections also showed uniform dispersion of the ZIF-8 material in the polymer matrix.   SEM was also used to measure the thickness of the fabricated membranes, which averaged 40-50 μm.   Data obtained from tensile testing showed an increase in Young's modulus (Table 12) at 20% w/w loading of ZIF-8, and then starts to decrease from 30 to 60% w/w loading.   This indicated that there was good interfacial contact between the ZIF-8 nanoparticles and Matrimid® at low loadings specifically at 20% resulting to an increase in elasticity.   However, at higher loadings the MMMs become brittle resulting to a decrease in Young's modulus.   The tensile strength of the MMMs showed similar trends.   ATR-FTIR spectra obtained of the MMMs showed both the adsorption bands of the Matrimid® and the ZIF-8 material.   The peaks for the ZIF-8 material, 1580 cm^{-1} (C=N stretch), and 1145, 990 cm^{-1} (C-N stretch) grow in intensity as the ZIF-8 loading increases.   The peak at 1580 is not well pronounced for the ZIF-8/Matrimid® MMMs because it is being masked by the presence of the C=O and C=C bands of Matrimid® [30].   No shift in the wavenumbers was observed for the adsorption bands of the MMMs, indicating that the surface interaction present for the ZIF-8 and Matrimid® would only be van der Waals forces.   The TGA plot (Figure 21) of annealed ZIF-8/Matrimid® showed that there was no weight loss up to 400 °C, indicating that guest molecules were not present in the pores of the ZIF-8 material, and that the casting solvent was completely evacuated after annealing.

Pure gas permeation (Figures 22 and 23) was tested for N$_2$, O$_2$, CH$_4$, C$_3$H$_8$, CO$_2$ and H$_2$ at 35 °C for ZIF-8 loadings up to 60% (w/w) above which the membranes became brittle.   The permeability increased for all gases as the loading of ZIF-8 increases from 0 to 40% (w/w).   At very low loadings of 20% (w/w), the effect of the ZIF-8 additive is not apparent because there is no significant change in permeability.   At 40% (w/w), the permeability increased in proportion to the amount of ZIF-8 present in the membrane, and in the order of C$_3$H$_8$ < H$_2$ < CO$_2$ < O$_2$ < N$_2$ < CH$_4$.   The results suggest that the permeability is highly governed by the transport properties of the polymer.   It is suggested that the ZIF-8 nanocrystal additive helps to create more free volume in the polymer leading to an increase in permeabilities [31]. However, the permeabilities of all gases decreased for the 50% (w/w) ZIF-8 loading. The decrease in permeability could be attributed to the increased ZIF-8 loading, wherein a change in matrix occurs [32]. Specifically, at 50% (w/w) ZIF-8 loading, the membrane matrix may become somewhat rigidified, causing the permeability properties to be more influenced by the presence of the ZIF-8 nanocrystals.   This leads to mixed-matrix membranes with gas permeability properties that are highly affected by the increased amount of ZIF-8 material.   The small pore windows of the ZIF-8 nanocrystals selectively transport small gas molecules resulting to their relatively high permeability

values at this loading.   Also, loadings of 50% (w/w) could create more tortuous diffusion path and smaller cross-sectional area available for transport leading to reduced permeability.   However, there is an apparent increase in permeability for all gases at the 60% (w/w) ZIF-8 loading.   This increase could be due to the formation of nonselective voids around the nanocrystals as the ZIF-8 particle loading increases, combining to give a channel network, thus increasing the permeation rate of the gases.   In summary, the increase in permeability at low ZIF-8 concentration could be due to an increase in polymer free volume, while at higher concentration clustering of ZIF-8 nanocrytals may lead to phase separation and a decrease in permeability [33].

There is no significant change in the ideal selectivities (Figure 24 and 25) of the gas pairs up to 40% (w/w) ZIF-8 loading.   The ZIF-8 nanocrystal could alter the polymer chain packing, in turn, resulting to separation properties not having high selectivity-destroying defects [34] at loadings up to 40% (w/w).   At 50% (w/w) ZIF-8 loading, an increase in selectivity is observed specifically for gas pairs containing small gas molecules, such as H_2/O_2, H_2/CO_2, and H_2/C_3H_8.   For these gas pairs, the increase in selectivity could be attributed to the sieving effect of the small pore aperture/window of ZIF-8 nanocrystals for smaller gas molecules.   For the 50% (w/w) ZIF-8/Matrimid® membrane, there is a transition from polymer to ZIF-8 driven permselectivity.

Gas mixtures of H_2/CO_2 (50:50 mol%) and CO_2/CH_4 (10:90 mol%) were used to test 50% and 60% (w/w) ZIF-8/Matrimid® MMMs.   The selectivities obtained for both loadings with the 50% H_2/50% CO_2 gas mixture were very close to the ideal selectivity, indicating that there is no competitive adsorption for this gas blend, which is consistent with the fact that both small gas molecules readily diffuse through the pore aperture of ZIF-8.   In contrast, for the 10% CO_2/90% CH_4 gas mixture, both loadings demonstrated a decrease in selectivity, suggesting that the higher composition of the bigger gas molecule, CH_4 could be blocking the diffusion or transport of the smaller CO_2 gas molecule through the ZIF-8 pore.   The effect of CO_2 plastization could also contribute to decrease in the gas mixture selectivity.

ZSM-5/Matrimid® mixed-matrix membranes

Cross-sections of the resulting membranes were prepared by freeze-fracturing the membranes after several minutes of immersion in liquid N_2. Figure 26 shows the SEM images of a pure Matrimid® membrane. The top view SEM images in Figure 26a and Figure 26b both show a smooth surface even at the 200 nm scale. The cross-section SEM images in Figure 26c and Figure 26d also show a clean surface at this magnification, which is characteristic of the pure polymer membrane. Figure 27 shows SEM iamges of Matrimid® membrane cross-sections containing different loadings of the mesoporous ZSM-5. In the cross-sections, many sub-micron particles can be observed. At low magnification (Figure 27a, b, and c), all cross-sections show a similar crater-like pattern, with mesoporous ZSM-5 particles located inside the crater. At higher loading, the size of the craters tend to be smaller. At the interface between the ZSM-5 particles and polymer, there are no micron size voids in Figure 27b, d, and f which suggests the contact between the polymer and the ZSM-5 particles is good at these magnifications. From the SEM image in Figure 27d, many tiny stress cracks attributed to the freeze-fracturing process as well as raised area of polymer can be seen. At the interface between the polymer and ZSM-5 particles, there are no

apparent voids or defects present. In contrast, microporous zeolites often show non-selective voids between the polymer and zeolite crystals [35]. The cross-section morphology obtained here is very similar to Friedrich's polypropylene membrane containing grafted SiO_2 particles. The fracture surface is characterized by the formation of elongated matrix segments and extensive cavitation sites, as indicated by a number of matrix-fibrillated circles around the particles, which is evidence of plastic deformation. The appearance of the matrix circles is probably the result of successive debonding of the mesoporous ZSM-5 crystals from the polymer matrix due to interfacial stress concentrations [36]. The mesoporous ZSM-5 particles are only 200 nm in diameter, which may help with polymer wetting and the mesopores are large enough for polymer chains to penetrate. The ZSM-5 has mesopores ~2.7 nm, while the polymer chains are ~ 0.7 nm in diameter, which may penetrate into the mesopores and lead to good contact. A Matrimid® membrane containing 10% uncalcined mesoporous ZSM-5 was also made and its cross-section checked with SEM. The presence of micron size voids is a indicator of poor interfacial contact, which was observed in mixed matrix membranes containing zeolites [37], carbon molecular sieve [18]. Since the mesopores of the uncalcined mesoporous ZSM-5 are still occupied by the template, the polymer chains cannot penetrate into the mesoporous ZSM-5 particles which should lead to bad interfacial contact. From SEM images in Figure 27g and h, cracks as big as 100 nm can be found easily which confirmed that the presence of mesopores is the key to good interfacial contact.

Table 13 lists the pure gas permeability results for the mixed-matrix membranes, while Figure 28 graphically illustrates the permeability results. The permeabilities of H_2, CO_2, and O_2 increased as the loading of mesoporous ZSM-5 increased, while CH_4 and N_2 decreased at 10% and 20% then increased again. The decreased permeabilities of slow gases, such as N_2 and CH_4, can be attributed to chain rigidification, which results in permeability reduction and higher selectivity. In addition, the diffusion of large gases, like CH_4 and N_2, in zeolite channels is slower than the diffusion in the polymer, which leads to lower permeability and higher selectivity. The penetration of polymer chains into the mesopores of ZSM-5 also narrows the pore size of the mesopores, which makes the diffusion in the mesopores much slower. The smaller gases, like H_2, CO_2, and O_2, are less affected, which results in higher permeability as the ZSM-5 loading increases. All these factors lead to a permeability reduction and higher selectivity. Additionally, CO_2 molecules have the ability to interact with the polar surface of zeolite during permeation and, hence, CO_2 permeability and permselectivity increase considerably with increasing zeolite loadings in the mixed-matrix membranes [38].

The ideal selectivities for five gas pairs are shown graphically in Figure 29. For H_2/N_2, there is an increase from 79.6 for pure Matrimid® to 142 at 10% loading. The ideal selectivity for O_2/N_2 increased from 6.6 for pure Matrimid® to 10.4 at 20% loading, while the H_2/CH_4 selectivity increased from 83.3 to 170 at 20% loading. The ideal selectivity for H_2/CO_2 and CO_2/CH_4 also increased compared with the pure Matrimid® membrane. The higher selectivity for these gas pairs must come from the molecular sieving effect. This result also suggests that the mixed-matrix membranes at this loading are defect free and the contact between the ZSM-5 particles and polymer is good. Since gas diffusion in mesopores is usually the result of Knudsen flow [39], the improved selectivity toward O_2/N_2 and H_2/N_2 can be attributed to the micropores of the mesoporous ZSM-5, which can provide size and shape selectivity. At 30% loading, the ideal selectivities of H_2/N_2, H_2/CH_4, O_2/N_2, and CO_2/CH_4 decreased, which suggests the presence of defects, compared with the 10% and 20% loadings. However, from the SEM images of

the mixed-matrix membrane cross-sections (Figure 27), the interfacial contact for the 30% membrane looks good and similar to that of the 10% and 20% membranes. However, the resolution of SEM used in this project can only reach 20 nm at most, and defects in the range of 5 to 20 nm, which cannot be seen at this resolution, can affect the gas permeation substantially. A ZSM-5 membrane supported on an α-Al$_2$O$_3$ tube via a template-free synthesis exhibits ideal selectives for O$_2$/N$_2$, CO$_2$/CH$_4$ and H$_2$/N$_2$ of 10, 770, and 480, respectively at 25°C [40]. These ideal selectivities of mesoporous ZSM-5/Matrimid$^®$ membranes lie between the pure Matrimid$^®$ membranes and the pure ZSM-5 membranes.

To test whether the gas molecules enter the zeolite crystal pores, pure gas permeation was run at a higher pressure. The permeability and ideal selectivity data are listed in Table 13. The pure gas permeation experiments were carried out at 1100 torr and 1900 torr, respectively. The permeability and ideal selectivity are within a narrow error range. This result suggests that the gas molecules primarily diffuse through the zeolite's pore system, instead of through defects in the membranes [13].

Matrimid$^®$ membranes containing 10% uncalcined mesoporous ZSM-5 and ZSM-5 crystals were also tested in control experiments. The uncalcined mesoporous ZSM-5 crystals have no accessible mesopores and micropores, since the pores are filled with organic template. A Matrimid$^®$ membrane containing 10% uncalcined mesoporous ZSM-5 resulted in an increase in permeability for all gases of at least 200% with lower selectivities, which suggests the presence of non-selective voids. The Matrimid$^®$ membrane containing ZSM-5 crystals also showed an increase in permeability and a decrease in selectivity, which suggests poor contact between the zeolite crystals and polymer. Calcined MCM-48 was also added into Matrimid$^®$ and the resulting membrane showed higher permeability and unchanged ideal selectivity compared with the pure Matrimid$^®$ membrane. These control experiments suggest that the mesopores are important in forming defect-free membranes, while the micropores can provide size and shape selectivity.

The diffusivities and solubilities of gases in pure Matrimid$^®$ and the mixed-matrix membranes are shown in Figures 30 and 31. The diffusivities of H$_2$ and O$_2$ increase as the loading increases, while N$_2$, CH$_4$, and CO$_2$ decrease first and then increase when the loading is 30%. The solubilities of all gases remain constant except for CO$_2$, which increases nearly 100%. This result can be attributed to the affinity between the CO$_2$ and the zeolite structure [41, 42]. The increase in H$_2$, O$_2$ and CO$_2$ diffusivity suggests that the gas diffusion of these small molecules is not affected in the zeolite channels, while the diffusion of bigger gases, like N$_2$ and CH$_4$, is slower due to the molecular sieving effect. When the zeolite loading is higher (>20%), there might be more defects, which leads to higher permeability for all gases. This result is consistent with the decreased selectivity at higher loading. The diffusivity selectivity and solubility selectivity data are shown in Figures 32 and 33. The diffusivity selectivities of H$_2$/N$_2$, CO$_2$/CH$_4$ and O$_2$/N$_2$ reach a maximum at 10% loading, but data at 20% and 30% loading are still better than pure Matrimid$^®$. When the loading is too high, there may be aggregates of molecular sieve particles, which can lead to lower selectivities and higher permeabilities. The solubility selectivity of CO$_2$/CH$_4$ increases as the loading increases, which can be attributed to the affinity between the mesoporous ZSM-5 and CO$_2$. The solubility selectivity of H$_2$/N$_2$ decreased while O$_2$/N$_2$ remained constant, which suggests the mesoporous ZSM-5 has no solubility selectivity toward H$_2$, N$_2$, and O$_2$. The data suggest the selectivity increase toward CO$_2$/CH$_4$ can be attributed to both solubility selectivity and diffusivity. CO$_2$ has a strong affinity toward zeolites, which can increase the solubility of CO$_2$, and CO$_2$ is much

smaller than CH_4, so that the diffusion of CO_2 in the zeolite channels is less affected than CH_4. The ideal selectivity increases for the H_2/N_2 and O_2/N_2 gas pairs are mainly from diffusivity selectivity. The diffusion of small molecules (H_2, O_2, and CO_2) in the zeolite channels is less affected with N_2 and CH_4.

Carbon aerogel/Matrimid® mixed-matrix membranes

The as-synthesized carbon aerogel is in a monolithic form and was ground into a fine powder with particle less than 1 micrometer in diameter by a mechanical ball mill. Matrimid® membranes containing carbon aerogels with different loadings were then prepared. The SEM images of the carbon aerogel-Matrimid® membrane cross-section in Figure 34 suggest good contact between the carbon aerogel particles and polymer. There are no obvious micrometer size voids between carbon aerogel particles and the polymer phase. The cross-section images reveal crater-like patterns surrounding the carbon aerogel particles. This morphology is a result of the freeze fracture process and demonstrates the strong affinity between the particles and polymer chains [17, 43, 44]. From the magnified micrograph (Figure 34 insets), the appearance of the fibrillated matrix circles is probably a result of successive debonding of the carbon aerogel particles from the polymer matrix due to the interfacial stress concentration. The presence of this morphology suggests strong interaction between the polymer and carbon aerogel particles [17, 43, 44].

Pure gas permeation of N_2, O_2, CH_4, CO_2, and H_2 were tested at 35 °C. When considering the kinetic diameter, the molecular dimensions increase in the order $H_2 < CO_2 < O_2 < N_2 < CH_4$ [18, 41]. This is also the order of decreasing permeability in Matrimid®. The condensability increases in the order $H_2 < N_2 < O_2 < CH_4 < CO_2$. The permeability values listed in Table 14 for pure Matrimid® are comparable to those previously reported [18, 35]. Table 14 also lists all the permeability and ideal selectivity values for the carbon aerogel mixed-matrix membranes at different loadings. The trend of permeability and ideal selectivity is shown graphically in Figures 35 and 36. The permeabilities of H_2, CO_2, and O_2 increased as the carbon aerogel loading increased, while the CH_4 and N_2 permeabilities decreased first at 10% and 20% loading, and then permeability increased at 30% loading. The decrease in the permeabilities of slow gases, such as N_2 and CH_4, can be attributed to the penetration of polymer chains into the mesopores of the carbon aerogel and the interaction between the carbon aerogel particles and polymer. This leads to chain rigidification, which results in permeability reduction and higher selectivity. In addition, the gas diffusion in the micropores of the carbon aerogel is slower than in the polymer, which leads to lower permeability and high selectivity. The penetration of polymer chains into the mesopores of the carbon aerogel also narrows the pore size of the mesopores, which makes the diffusion in the mesopores slower. All these factors can lead to the permeability reduction for larger gas molecules, like CH_4 and N_2, and higher selectivity towards smaller gases, like CO_2, H_2, and O_2. The permeability of the fast gases, such as CO_2 and H_2, increases as the carbon aerogel content increases. This can be attributed to the large permeabilities of CO_2 and H_2 and their small molecular size.

Pure gas permeation showed that the ideal selectivities for O_2/N_2, H_2/N_2, and CO_2/CH_4 increased from 6.63, 79.55, and 34.71 for pure Matrimid® to 9.41, 115.75, and 47.80 at 10% loading. These results can be compared with CMS-Matrimid® membranes, where the highest O_2/N_2 selectivity was 7.9 at 36% loading while the CO_2/CH_4 selectivity was 51.7 at 36% loading [18]. In the present case, the ideal O_2/N_2

selectivity was higher when the loading was between 10%-20%. At 30%, the O_2/N_2 ideal selectivity dropped to 8.36. This result may reflect some aggregation of the carbon aerogel in the membrane at high loading. The improved selectivity toward O_2/N_2 and H_2/N_2 can be attributed to the micropores of the carbon aerogel.

The diffusivities and solubilities of gases in pure Matrimid[®] and mixed-matrix membranes are shown in Figures 37 and 38. The diffusivities of H_2, CO_2, and O_2 increase as the loading increases, while for N_2 and CH_4, diffusivity first decreases at 10% and then increases when the loading is 30%. The solubilities of all gases remain constant except for CO_2, which increases nearly 30%. The diffusivity selectivity and solubility selectivity data are shown in Figures 39 and 40. The diffusivity selectivities of H_2/N_2, CO_2/CH_4, and O_2/N_2 reach a maximum at 10% loading, but data at 20% and 30% loading are still better than pure Matrimid[®], except for CO_2/CH_4. The solubility selectivity of CO_2/CH_4 increases as the loading increases, while the solubility selectivity of H_2/N_2 decreased and O_2/N_2 remained constant. The data suggest that the selectivity increment toward CO_2/CH_4 and H_2/N_2 can be attributed to both solubility selectivity and diffusivity. The selectivity increase toward O_2/N_2 is mainly from diffusivity selectivity. The diffusion of small molecules (H_2, O_2, and CO_2) in the micropores of carbon aerogel is less affected compared with big molecules, such as N_2 and CH_4.

To test whether the gas molecules enter the carbon aerogel pores, pure gas permeation was run at higher pressure. The permeability and ideal selectivity data are listed in Table 14. The pure gas permeation experiments were carried out at 1300 and 2000 torr. The permeability and ideal selectivity are within a narrow range of error. This result suggests that the gas molecules did enter the micropores and the contribution from non-selective voids is minimal [18, 45-47].

Gas mixtures of CO_2/H_2 (50:50 mol% and 75:25 mol%), CO_2/CH_4 (10:90 mol% and 50:50 mol%) and CH_4/N_2 (50:50 mol% and 94:6 mol%) were used to test the mixed matrix membrane. The separation of the gas mixtures was conducted with a 10% carbon aerogel/Matrimid[®] membrane at 35 °C. Table 15 lists the selectivity data. The selectivities of gas mixtures are very close to the ideal selectivity for N_2/CH_4, CO_2/CH_4, and CO_2/H_2 separation, which suggests there is no competitive adsorption of the gases in the carbon aerogel at this temperature and pressure. The separation is mainly determined by the molecular sieving effect. This result is reported for Matrimid[®] membranes containing carbon molecular sieves. The O_2/N_2 selectivity was 7.9 (36% loading) and they observed a higher selectivity toward CO_2/CH_4, 51.7 (36% loading), compared with 35.3 of pure Matrimid[®] membrane [18].

Carbon aerogel-zeolite composites/Matrimid[®] mixed-matrix membranes

The gas mixture separation was conducted with 10% (w/w) carbon aerogel-zeolite A and zeolite Y-Matrimid[®] membranes at 35 °C. Table 16 lists the selectivity data. The selectivities of gas mixtures are very close to the ideal selectivity for N_2/CH_4, CO_2/CH_4 and CO_2/H_2 separation, which suggests that there is no apparent competitive adsorption of the gases in the carbon aerogel-zeolite composites. The mixed-matrix membranes are selective towards smaller gas molecules, such as CO_2, H_2, and N_2, which is the result of the molecular sieving effect. Pure Matrimid[®] exhibits no selectivity for N_2/CH_4 separation, due to the similar size of these two molecules. However, carbon aerogel-zeolite A/Matrimid[®] membranes show improved N_2/CH_4 selectivity, which can be attributed to the small pore

diameter of zeolite A.   For carbon aerogel and carbon aerogel-zeolite Y/Matrimid[®] membranes, no selectivity gain was observed, because of the larger pore size of carbon aerogel and zeolite Y.   For CO_2/CH_4 separation, higher selectivity was obtained for carbon aerogel-zeolite/Matrimid[®] membranes, which comes from the affinity between the zeolite crystals and the CO_2 molecule.   The presence of zeolite A also helps to increase the CO_2/CH_4 selectivity via molecular sieving.   As for H_2/CO_2 separation, no big change was observed since the permeability of CO_2 and H_2 are too high.

Functionalized SWNT/Matrimid[®] mixed-matrix membranes

Figures 41 and 42 show the SEM cross-section view of Matrimid[®] membranes containing different loadings of SWNT-COOH and SWNT-short. From the cross-section images, no aggregates can be found at this magnification, which suggests good dispersion of SWNT-COOH and SWNT-short. The surface morphology (not shown) of the mixed-matrix membranes look like the pure Matrimid[®] membrane, especially at low loading. The result indicates good dispersion and compatibility between the SWNT and Matrimid[®]. When the loading of SWNT increases to 10%, the cross-section becomes rough and some fiber like features can be found, which might be the SWNT bundles. Kim et al. incorporated SWNTs into PDMS [48] and polysulfone [49] to make mixed-matrix membranes. SEM images of these membrane cross-sections show a fiber-like morphology which suggests the presence of SWNT bundles. In SWNT-polysulfone membranes, phase separation was observed at high loading, like 5%, which suggests the dispersion of SWNT was not homogeneous [49].

Pure gas permeation of N_2, O_2, CH_4, CO_2, and H_2 were tested at 35°C. When considering the kinetic diameter, the molecular dimensions increase in the order $H_2 < CO_2 < O_2 < N_2 < CH_4$. This is also the order of decreasing permeability in Matrimid[®] [18, 50]. The values listed in Table 17 are comparable to those previously reported for pure Matrimid[®] [18, 51, 52]. Table 17 also lists all the permeability and ideal selectivity values for the SWNT mixed-matrix membranes at different loadings. The permeabilities of all five gases increased as the SWNT loading increased, for both SWNT-COOH and SWNT-short-Matrimid[®] membranes. However, there is no apparent increase in ideal selectivity for H_2/N_2, O_2/N_2, CO_2/CH_4 and H_2/CO_2 separation. Although SWNTs were used as a H_2 storage material, the mixed-matrix membrane didn't show selectivity towards H_2, which suggests that SWNT has no affinity for H_2. Since SWNTs used in this project have micropores, higher selectivity towards O_2/N_2, H_2/N_2 and CO_2/CH_4 was expected because of molecular sieving effect. But ideal selectivities remained unchanged. There are several reasons that might contribute to this result. First, the content of SWNT loading is low compared with other mixed matrix membranes. For mixed-matrix membranes containing zeolites and carbon molecular sieves, the best results were usually obtained at 30 wt% loading [18, 35, 41, 45-47, 53]. In the present case, the maximum SWNT loading was only 5 to 10 wt%, which might not be enough to make a difference. At high loadings, the presence of defects may lower the selectivity. Second, the SWNTs were functionalized with carboxylic acid groups, which might block the pore entrance [54-57], such that the SWNTs might behave like an inert filler. Also, the gas diffusion in the SWNTs might not be selective [31, 58-63], since there are SWNTs with larger pore sizes (1 nm).

The diffusivities and solubilities of gases in pure Matrimid[®] and the mixed matrix membranes are shown in Table 18. The solubilities of all gases remain constant regardless of the SWNT loading, which

suggests that the higher permeability must come from diffusivity. Since the SWNTs were functionalized with polar groups, and the surface area is low, the affinity for gases such as H_2 and CH_4 is not surprise. The diffusivity increases as the loading increases, which might be attributed to the fast diffusion in the SWNT. Although the SWNT loading is low (<5%) and the SWNTs are not continuous in the mixed-matrix membranes, substantial increase was still observed, which suggest the fast diffusion in the SWNT.   Kim et al, incorporated raw SWNTs into PDMS and SWNT functionalized with long chain alkyl amines into polysulfone respectively [48, 49]. Both permeabilities and diffusivities of the mixed-matrix membranes increased as the SWNT loading were increased. For the PDMS-SWNT membranes, no selectivity change was observed. However, lower H_2/CH_4 selectivity was obtained and explained as the result of affinity between the CH_4 and SWNT [48, 49]. In this project, CO_2/CH_4 and H_2/CH_4 selectivities didn't decrease as the SWNT loading was increased, which is not consistent with Kim's result, which was also predicted by Sholl's simulation [61, 62]. Since the O_2/N_2 selectivity remained unchanged, this result suggests there might be no affinity between the SWNT and CH_4 molecules or the presence of carboxylic group may block the pore entrance, which leads to no selectivity change.

Gas mixtures of CO_2/H_2 (50:50 mol% and 75:25 mol%), CO_2/CH_4 (10:90 mol% and 50:50 mol%) and CH_4/N_2 (50:50 mol% and 94:6 mol%) were used to test the mixed matrix membrane. The gas mixture separations were conducted with 4 wt% SWNT-COOH and SWNT-short-Matrimid® membranes at 35 °C, as shown in Table 19. The selectivities of gas mixtures are very close to the ideal selectivity, which suggests there is no competitive adsorption of the gases in the carboxylic decorated SWNT.

Cu-BPY-HFS/Matrimid® mixed-matrix membranes

Permeation for the pure gases N_2, O_2, CH_4, CO_2, and H_2 were tested at 35 °C. The molecular dimensions of these five gases are listed in Table 24 [45, 64]. When considering the kinetic diameter, the molecular dimensions increase in the order $H_2 < < CO_2 < O_2 < N_2$ and CH_4. This is also the order of decreasing permeability in Matrimid®.   The permeabilities of pure Matrimid®, listed in Table 25 are comparable to those previously reported [47, 64].   Table 25 also lists all of the permeability and ideal selectivity values for the Cu-BPY-HFS/Matrimid® mixed-matrix membranes at different loadings. Figures 43 and 44 show the permeability and ideal selectivity data graphically. For all gases tested, the pure gas permeability increases as the loading increases. At 40%, a substantial increase in the permeability of all five gases was observed.   This increase usually suggests the presence of defects which increase gas permeability but with a loss in the selectivity. SEM images of membrane cross-sections in Figure 45 confirm the presence of aggregates and defects at the 40% loading. However, the ideal selectivities of O_2/N_2, H_2/CO_2, and CH_4/N_2 didn't significantly change compared with the 30% and 20% loadings. At the 40% loading, the ideal selectivities of CO_2/CH_4 and H_2/CH_4 decreased from 35 and 83 to 25 and 45, respectively. Lower selectivity usually suggests poor contact between the MOF particles and the polymer. However, the ideal selectivity of CH_4/N_2 actually increased from 0.95 to 1.21, instead of decreasing, which contradicts the idea of poor contact, since higher selectivity indicates good interfacial contact. The ideal selectivity of O_2/N_2 remained unchanged which provides another indication that the mixed matrix membranes are defect-free. These results are consistent with an increased

solubility of CH_4 in the membranes, which leads to higher selectivity towards CH_4, and explains the higher CH_4/N_2 ideal selectivity and the lower CO_2/CH_4 and H_2/CH_4 ideal selectivities. This result confirms the Cu-BPY-HFS has strong affinity towards CH_4 and favors the permeation of CH_4. Interestingly, the H_2/N_2 ideal selectivity also decreased from 80 to 54, just like the H_2/CH_4 ideal selectivity. This result can be attributed to the similar size of CH_4 and N_2, and that the Cu-BPY-HFS has a weak affinity towards N_2, compared with CH_4. The ideal selectivity of H_2/CO_2 decreased from 2.4 to 2.0, which suggests that the Cu-BPY-HFS interacts more strongly with CO_2 than H_2.

Figures 46, 47, 48, and 49 show the solubility and diffusivity data calculated from the raw data using the solution-diffusion model. From Figure 46, it can be seen that the diffusivity of CH_4 remained almost unchanged while the other four gases showed an apparent increase as the MOF loading increased. This result can be attributed to the large 0.8 nm pore size of Cu-BPY-HFS, which cannot limit the diffusion of small gas molecules. As shown in Figure 47, the solubility of CH_4 almost tripled, while the other four gases showed only a modest increase. This result can only be explained by a strong affinity between the Cu-BPY-HFS and CH_4. Figures 48 and 49 show the diffusivity, selectivity, and solubility selectivity data of CH_4/N_2, CO_2/CH_4, and O_2/N_2, respectively. It is apparent that the increased solubility of CH_4 dominates the CO_2/CH_4 and CH_4/N_2 separation. The Cu-BPY-HFS's affinity for CH_4 leads to higher solubility in the mixed-matrix membrane and higher selectivity towards CH_4.

To test whether the gas molecules enter the Cu-BPY-HFS pores or diffuse through polymer-particle interfacial voids, pure gas permeation studies were run at a higher pressure. The permeability and ideal selectivity data are listed in Table 25. The pure gas permeation experiments were carried out at 2000 and 3000 torr, respectively. The permeability and ideal selectivity values at these two pressures are within the 4 % error range, which suggests that the gas permeability is dominated by interaction with the metal organic framework pores verse defects in the membranes [65].

Several mixtures were tested as shown in Table 26. Generally, the selectivity for gas mixtures is not as good as the ideal selectivity predicted by pure gases. For pure Matrimid® membranes, the selectivities of CH_4/N_2 are almost the same as the ideal selectivity, which suggests that there is no competitive adsorption between CH_4 and N_2. In contrast, for the MOF mixed-matrix membrane at 20% loading of Cu-BPY-HFS, the $\alpha_{CH4/N2}$ for the mixed gases increased to 1.7, while the ideal selectivity is 1.16. The selectivity of CO_2/CH_4 decreased from 34 to 20, much lower than the ideal selectivity of 27.6 for CO_2/CH_4. As for the separation of the CO_2/H_2 mixture, there was not a large difference compared with pure Matrimid®, which suggests the Cu-BPY-HFS has no affinity towards H_2 or CO_2. This result suggests that the Cu-BPY-HFS has strong affinity for CH_4 and the competitive adsorption of CH_4 over N_2 increases the solubility of CH_4 in the membrane selectively in the mixture. The diffusivities of CH_4 and N_2 are not affected in the same way, since the pore size of the MOF is 0.8 nm and no size or shape selectivity is expected.

PMOs/Matrimid® mixed-matrix membranes

Figure 50 shows the SEM images of MBS-Matrimid® membrane cross-sections. Micron size MBS particles are dispersed homogeneously in the membrane and the fiber-like structure of MBS particle is obvious at high magnification. There are no apparent voids at the interface of the polymer and MBS

material, which indicates good interfacial contact. The maximum loading we can obtain without generating many visible defects is 30 wt%. Figure 51 shows the cross section SEM images of Matrimid® membranes containing 10 wt% PMOs made from Brij 76. Sub-micron size PMO particles are visible at the cross section and no presence of defects and non-selective voids at the interface. Since the MBS and other PMOs have largely organic frameworks, the hydrophobic organic pores may be more compatible with polymers than hydrophilic zeolites. The presence of mesopores ~ 3 nm may also allow the polymer chains to penetrate, which also results in better interfacial contact.

Table 27 lists the pure gas permeabilities and ideal selectivities of Matrimid® membranes containing MBS with loading form 10 wt% to 30 wt%. The permeability of all five gases increase as the loading increases, which is reasonable, since the gas diffusion in the mesopores is fast with no molecular sieving effect. The ideal selectivity for H_2/N_2, shows little change, while the selectivities for O_2/N_2 and CO_2/CH_4 separation exhibit moderate increase from 6.64 and 34.7 to 7.97 and 57.6, respectively. This result suggests there might be molecular sieving effect; however, the gas diffusion in mesopores follows Knudson diffusion, which is non-selective. The enhanced selectivity might come from the hydrophobicity of the MBS framework. The hydrophobic framework of MBS may be more compatible with polymer which leads to fewer defects. The polymer chains may penetrate into the mesopores and result in chain rigidification. The polymer rigidification leads to denser polymer packing, which contributes to enhanced selectivity towards small gas molecules. When the MBS loading increases, the ideal selectivities start to decrease which might suggest the presence of defects at higher loading. However, the ideal selectivity of CO_2/CH_4 is still higher than pure Matrimid® but lower than 10wt % loading.

The solubilities and diffusivities of O_2, N_2, CO_2 and CH_4 are shown in Table 28. From the solubility data, there is no apparent change for H_2, O_2, N_2, and CH_4, which suggests that MBS does not selectively adsorb these gases effectively at room temperature. However, the solubility of CO_2 exhibits an increase, which is consistent with CO_2's high critical temperature and easy condensability. The diffusivities of these gases exhibit substantial increase as the loading increases, which can be attributed to the Knudson diffusion in the mesopores. For diffusivity selectivity, there is no clear trend, however, no big change either. As for solubility selectivity, H_2/N_2 decreases as loading increases, which might be caused by the higher solubility of N_2 in the PMO. The solubility selectivity of CO_2/CH_4 increases apparently as loading increases, which should be the result of the easy condensability of CO_2. However, there is not a big change when loading is above 10%. The solubility selectivity for O_2/N_2 also shows slight decrease, although the difference of critical temperature between these two gases is very small.

The data for gas mixture separation are shown in Table 29. The selectivity of H_2/CO_2 separation is only slightly lower than ideal selectivity. As for CO_2/CH_4 separation, selectivities are around 47, lower than ideal selectivity but higher than pure Matrimid® membrane. The selectivity for N_2/CH_4 is slightly lower than ideal selectivity. Generally speaking, there is no big difference with the ideal selectivity. The result suggests that the MBS and other PMOs have no affinity towards these five gases. The hydrophobic framework of the PMOs may help to provide better interfacial contact, but cannot affect gas separation.

CONCLUSIONS

Microporous organic-inorganic hybrid nanocrystals like MOF-5, Cu-MOF, ZIF-8, and MOP-18 are good additives for the preparation of polymer based mixed-matrix membranes.   Compared to inorganic additives, the inclusion of these materials reduced the time and steps required for membrane preparation due to the organic character of the crystals that facilitated their dispersion and improved the interfacial contact with the polymer matrix.   In addition to these benefits, the MOF materials induced better gas transport properties (increased selectivity and permeability) for important separations like H_2/CO_2, CH_4/N_2, and C_3H_6/N_2 thus demonstrating their potential applications in gas separation.   Of particular importance is ZIF-8 which improved the selectivity of H_2/CO_2 from 2.9 to 4.4 and the permeability of H_2 from 26.5 to 35.8 Barrers.   The molecular sieving effect coming from the small pore window (0.34 nm) of ZIF-8 reduced the transport of molecules larger than H_2 and CO_2.   The molecular sieving effect of ZIF-8 was manifested at loadings above 40% (w/w), which indicates that a high additive loading may be required to overcome the transport properties of the polymer.   Owing to the hybrid nature of ZIF-8, MOP-18, and other MOFs, high additive loadings are possible, yielding materials that are mechanically strong enough to allow their manipulation and testing.

The inherent organic functionalization of MOP-18 is promising in that it facilitates the fabrication of homogeneous mixed-matrix membranes with extremely high loadings.   The 80 wt% MOP-18/Matrimid® membrane showed neither signs of additive aggregation nor the formation of large defects.   The preparation of this membrane encourages the engineering and development of similar materials for specific gas separations.

Not all the MOFs tested improved the H_2/CO_2 separation.   Rather, some Cu-MOFs improved the separation of important gas mixtures like CH_4/N_2.   For example, the 20% (w/w) Cu-BPY-HFS/Matrimid® membrane gave a CH_4/N_2 selectivity of 1.6 and a CO_2/CH_4 selectivity of 24.1 from their respective gas mixtures, which agree with pure gas permeation data.   The obtained results suggest that the Cu-BPY-HFS has affinity for CH_4 and, therefore, has the potential to be used for CH_4/N_2 separation.

Materials with both micropores and mesopores, such as carbon aerogel and carbon aerogel-zeolite composites, incorporated into Matrimid® to form mixed-matrix membranes showed a substantially higher selectivity towards the separation of mixtures of CO_2/CH_4.   The higher selectivity can be attributed to size and shape selectivity from the micropores.   The mesopores can solve the contact problem of mixed-matrix membranes, while the micropores can provide size and shape selectivity.   The low cost of the carbon aerogel makes it promising for industrial applications.
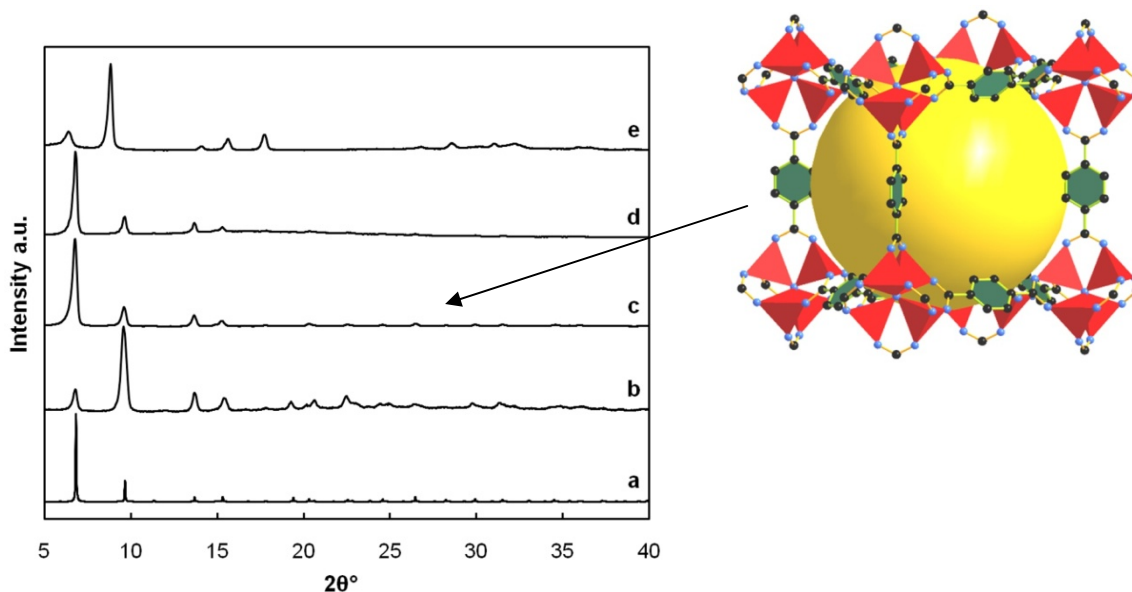
Figure 1. MOF-5 X-ray diffraction patterns: a) simulated from single crystal X-ray data [21], b) as-synthesized, c) activated, d) 30% activated MOF-5/Matrimid® mixed-matrix membrane, and e) activated MOF-5 exposed to moisture.
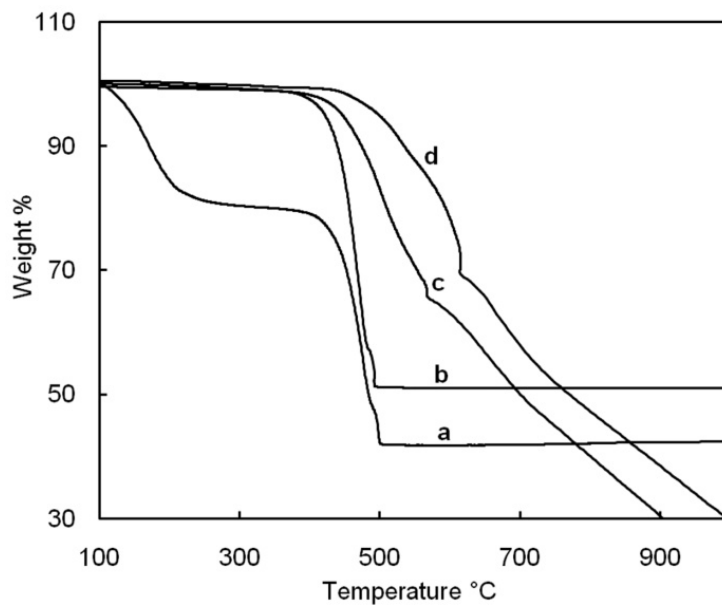
Figure 2. TGA of a) as-synthesized MOF-5, b) activated MOF-5, c) 20% activated MOF-5/Matrimid® mixed-matrix membrane, and d) Matrimid® powder.
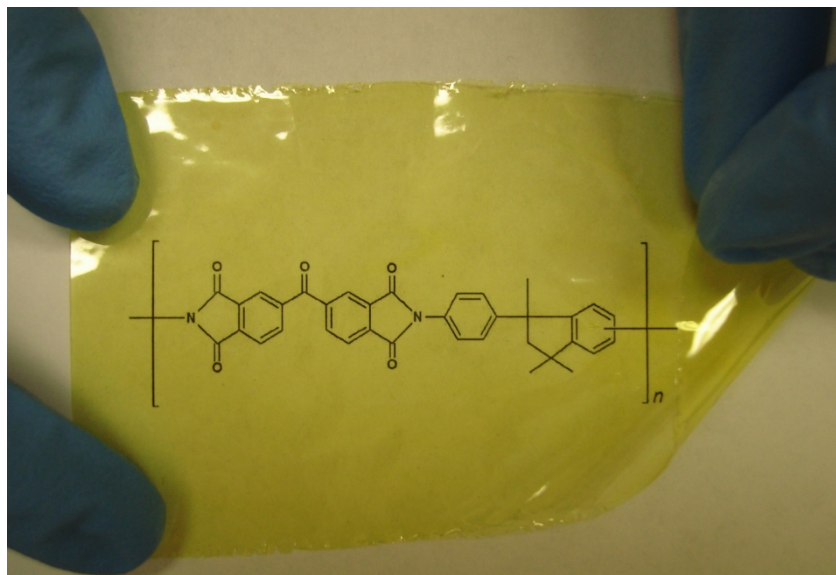
Figure 3. Flat Matrimid® membrane cast from chloroform.
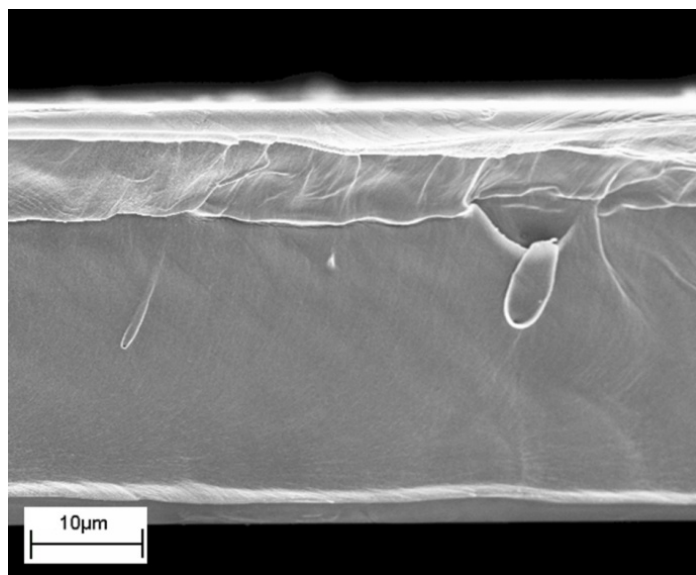
Figure 4. SEM image of the cross-section of a pure Matrimid® membrane.
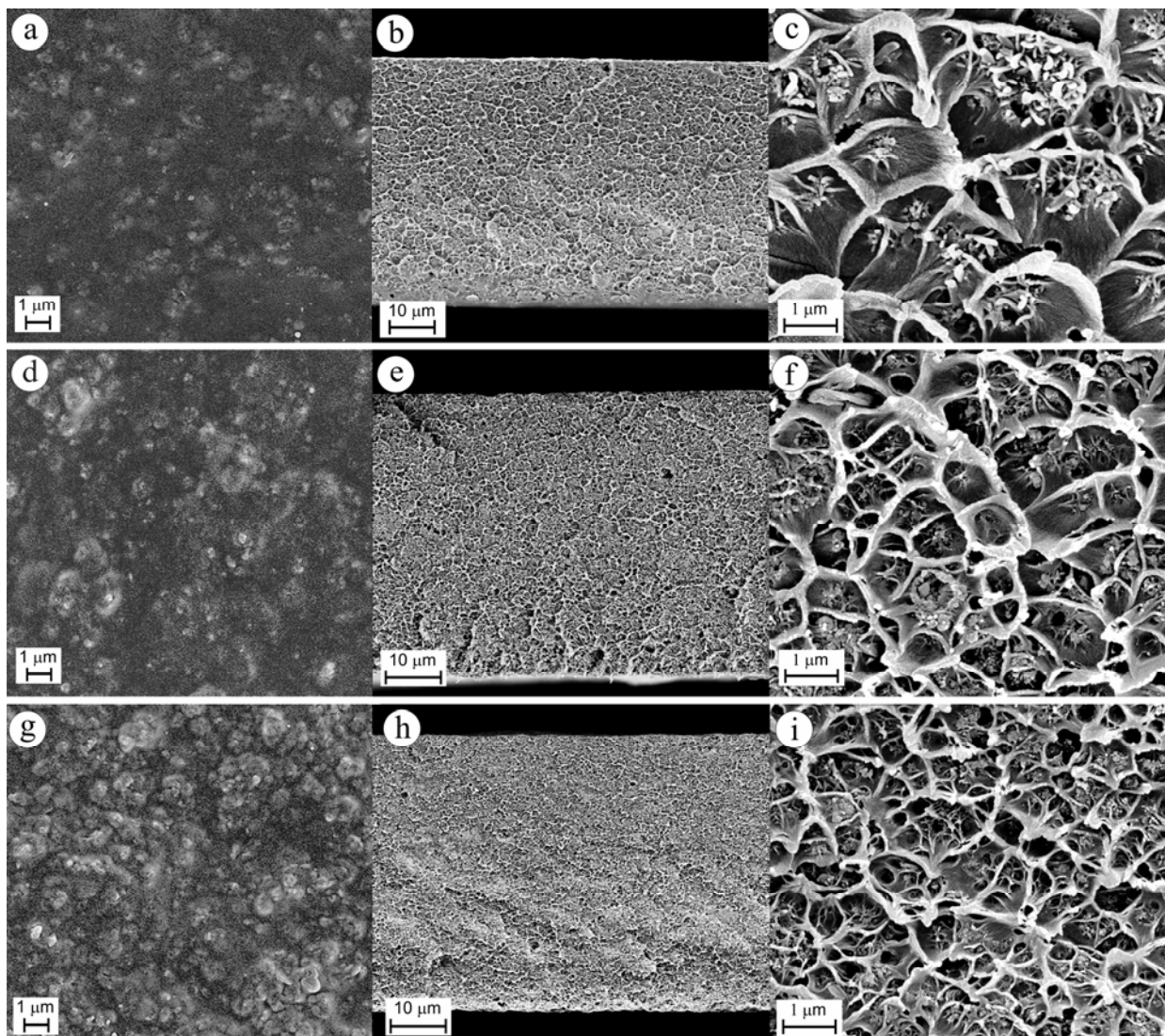
Figure 5. SEM images of the surface (a, d, and g), cross-section at low magnification (b, e, and h), and cross-section at high magnification (c, f, and i) of 10, 20, and 30% (w/w) MOF-5/Matrimid® mixed-matrix membranes, respectively. The cross-sections show plastic deformation of the polymer matrix due to the presence of the MOF-5 nanoparticles.
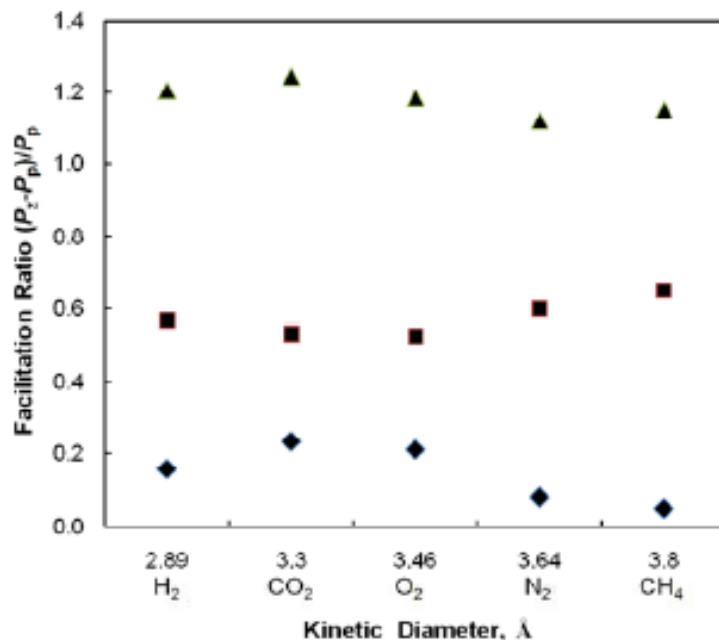
Figure 6. Facilitation plot of measured gases for MOF-5/Matrimid® mixed-matrix membranes: (♦) 10% MOF-5; (■) 20% MOF-5; (▲) 30% MOF-5.
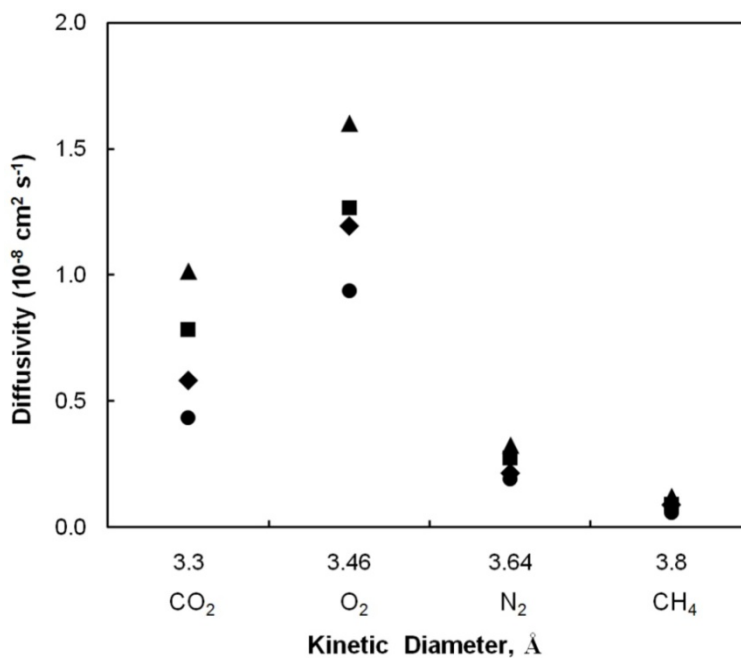
Figure 7. Diffusivities of tested gases for MOF-5/Matrimid® mixed-matrix membranes: (●) Matrimid®; (♦) 10% MOF-5; (■) 20% MOF-5; (▲) 30% MOF-5.
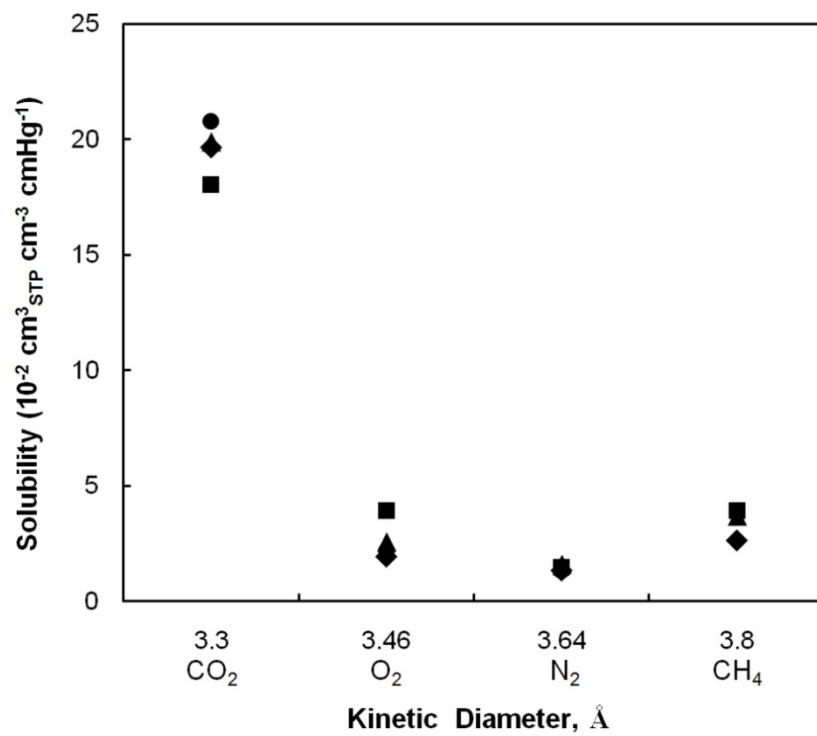
Figure 8. Solubilities of tested gases for MOF-5/Matrimid® mixed-matrix membranes: (●) Matrimid®; (♦) 10% MOF-5; (■) 20% MOF-5; (▲) 30% MOF-5.
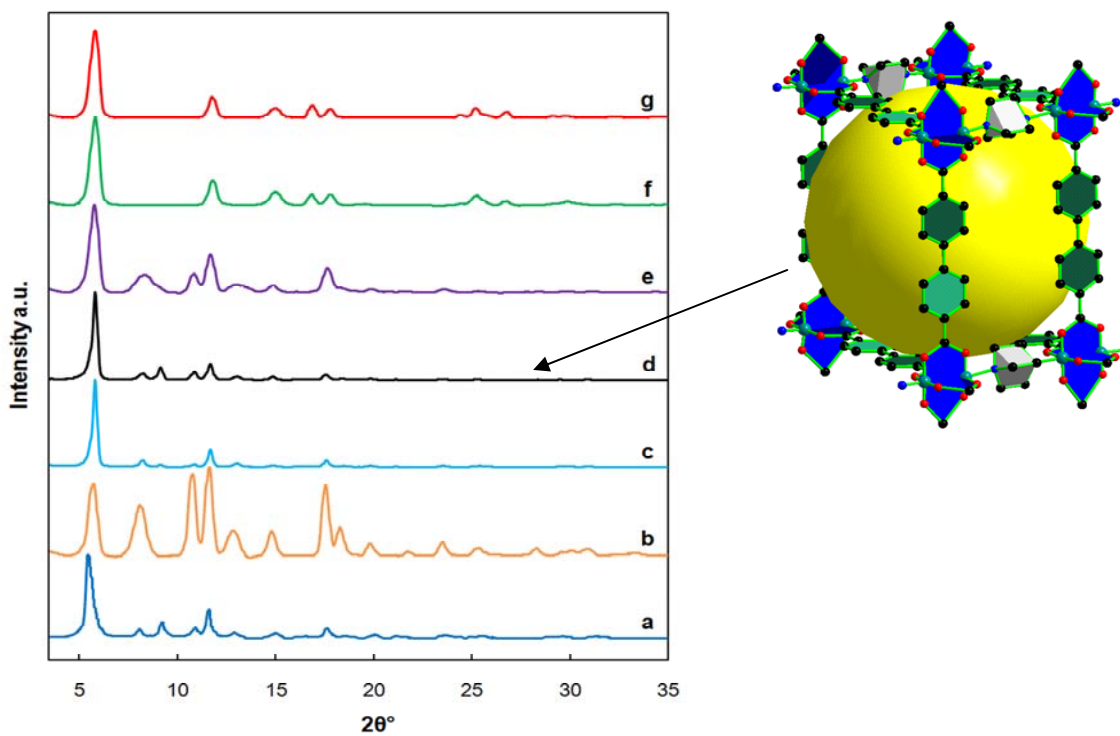
Figure 9. Cu-MOF X-Ray diffraction patterns: a) simulated [4], b) as-synthesized, c) semi activated, d) activated, e) 20% activated Cu-MOF/Matrimid® mixed-matrix membrane, f) activated Cu-MOF exposed to moisture, and g) plausible 2D phase.
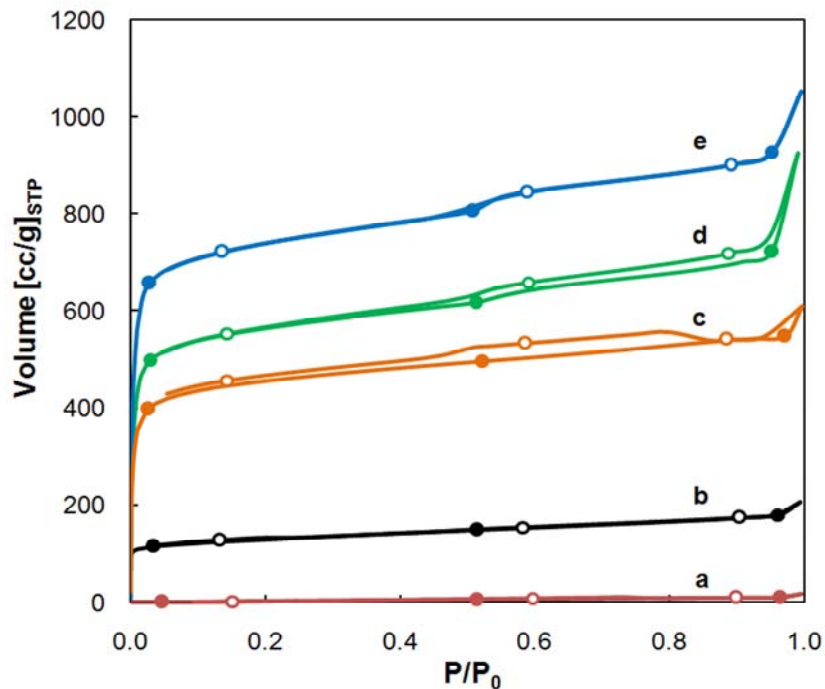
Figure 10. Nitrogen sorption (filled markers) and desorption (empty markers) isotherms at 77 K of a) Matrimid® membrane, b) as-synthesized Cu-MOF (BET SA = 400 m2/g), c) an 45 wt% Cu-MOF/Matrimid® MMM (BET SA = 1700 m2/g), d) semi activated Cu-MOF (BET SA = 2200 m2/g), and e) fully activated Cu-MOF (BET SA = 3000 m2/g).
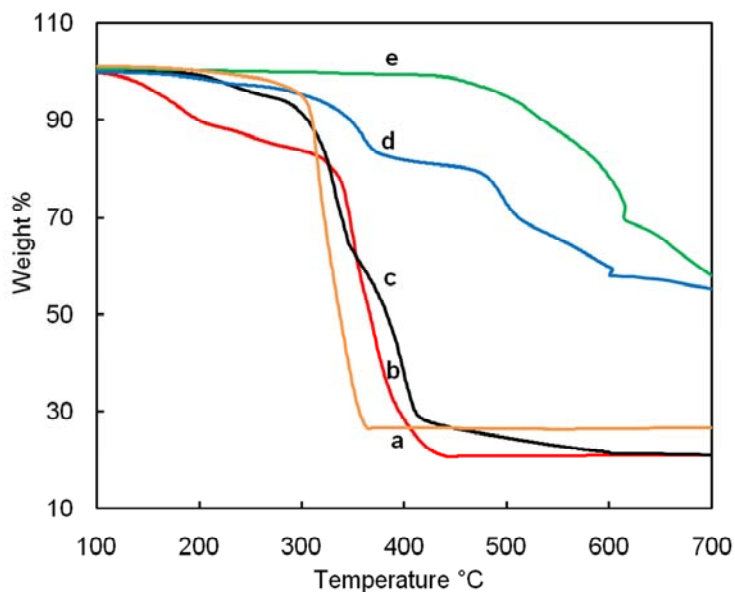
Figure 11. TGA of a) possible 2D phase of Cu-MOF, b) as-synthesized Cu-MOF, c) activated Cu-MOF, d) 30% activated Cu-MOF/Matrimid® mixed-matrix membrane, and e) Matrimid® powder.
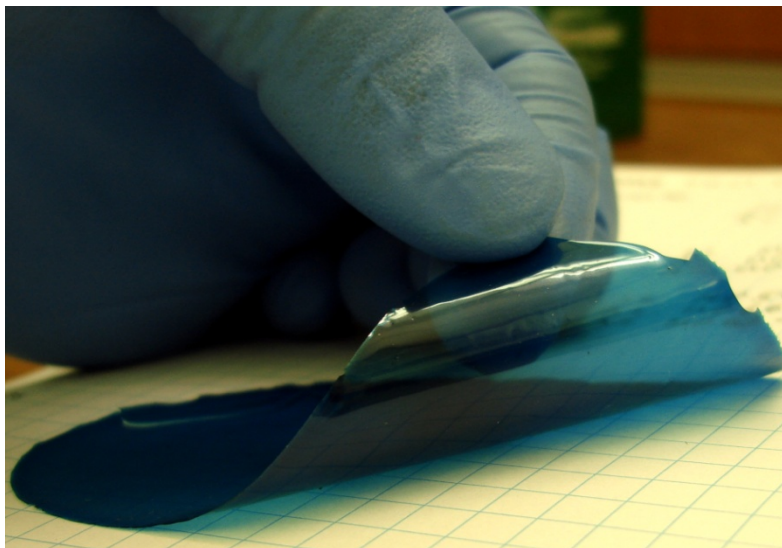
Figure 12. A 80% (w/w) MOP-18/Matrimid$^{®}$ membrane
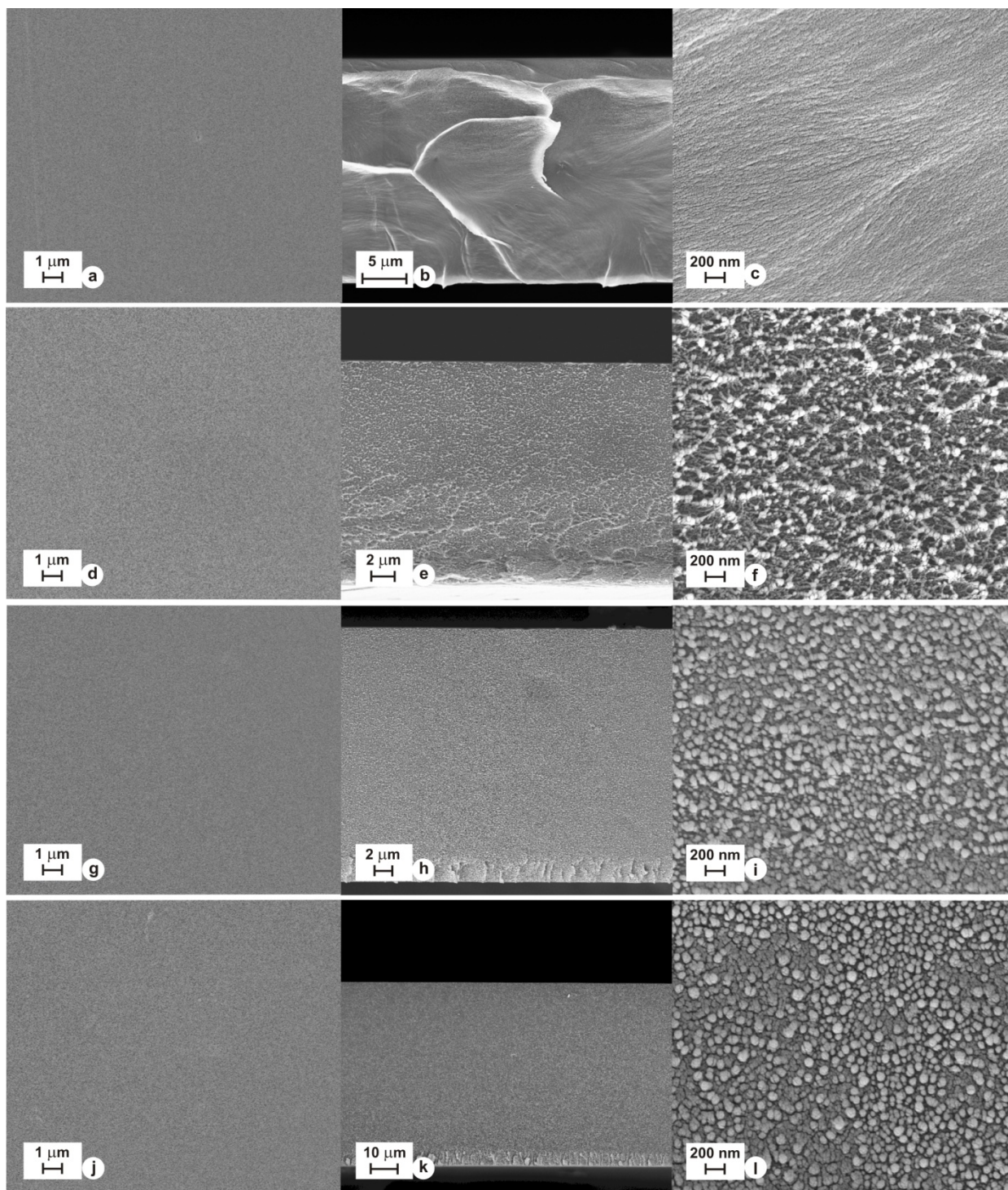
Figure 13. SEM images of the surface (a, d, g, and j), cross-section at low magnification (b, e, h, and k), and cross-section at high magnification (c, f, i, and l) of 0, 23, 33, and 45 wt% MOP-18/Matrimid® mixed-matrix membranes, respectively.   The cross-sections show no aggregation of the MOP-18 crystals.
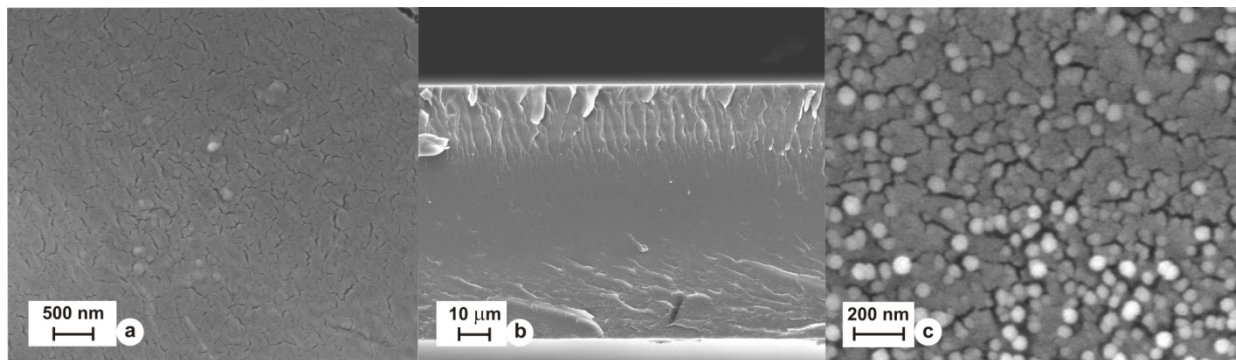
Figure 14.   SEM image of a 80 wt% MOP-18/Matrimid[®], a) surface, b) cross-section low magnification, and c) cross- section high magnification.
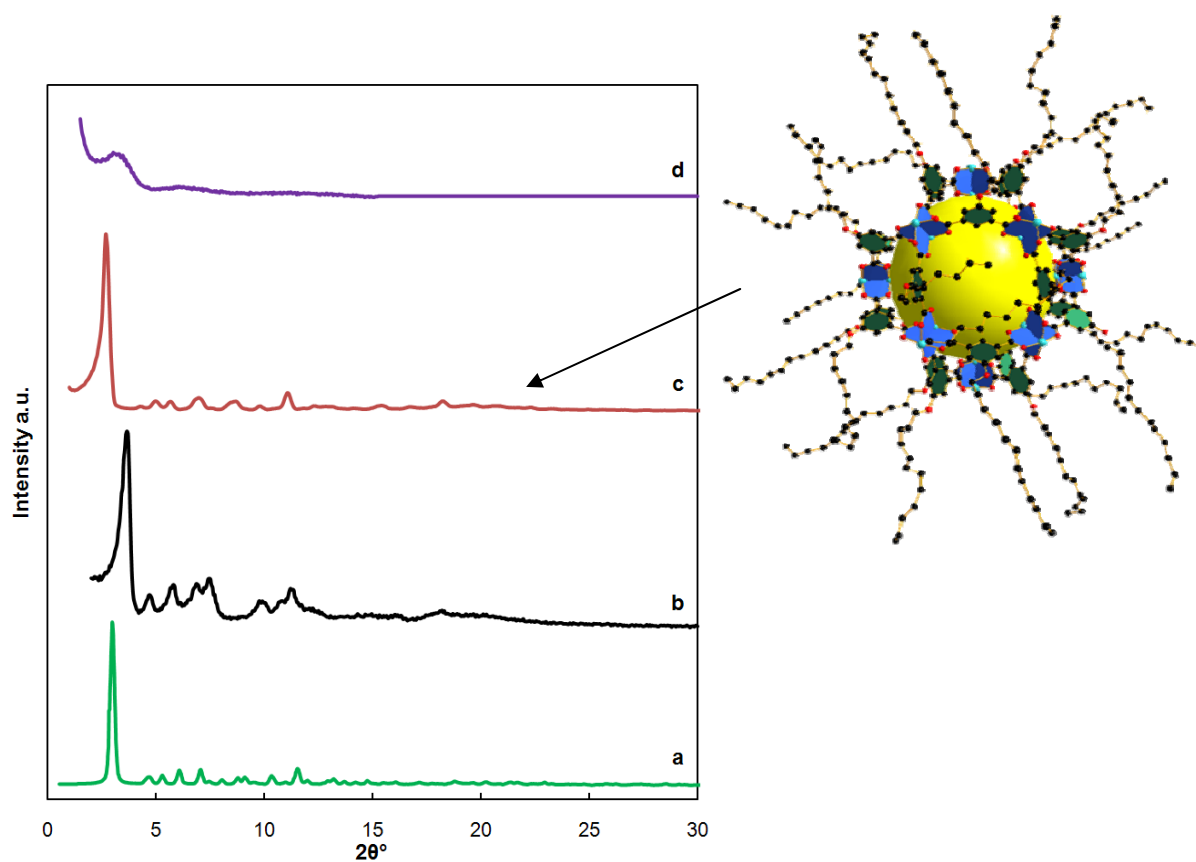
Figure 15. X-ray diffraction of a) theoretical MOP-18 X-ray diffraction, b) experimental, c)experimental recrystallized from hexanes/heptanol, and d) a 80% (w/w) MOP-18/Matrimid[®] membrane.
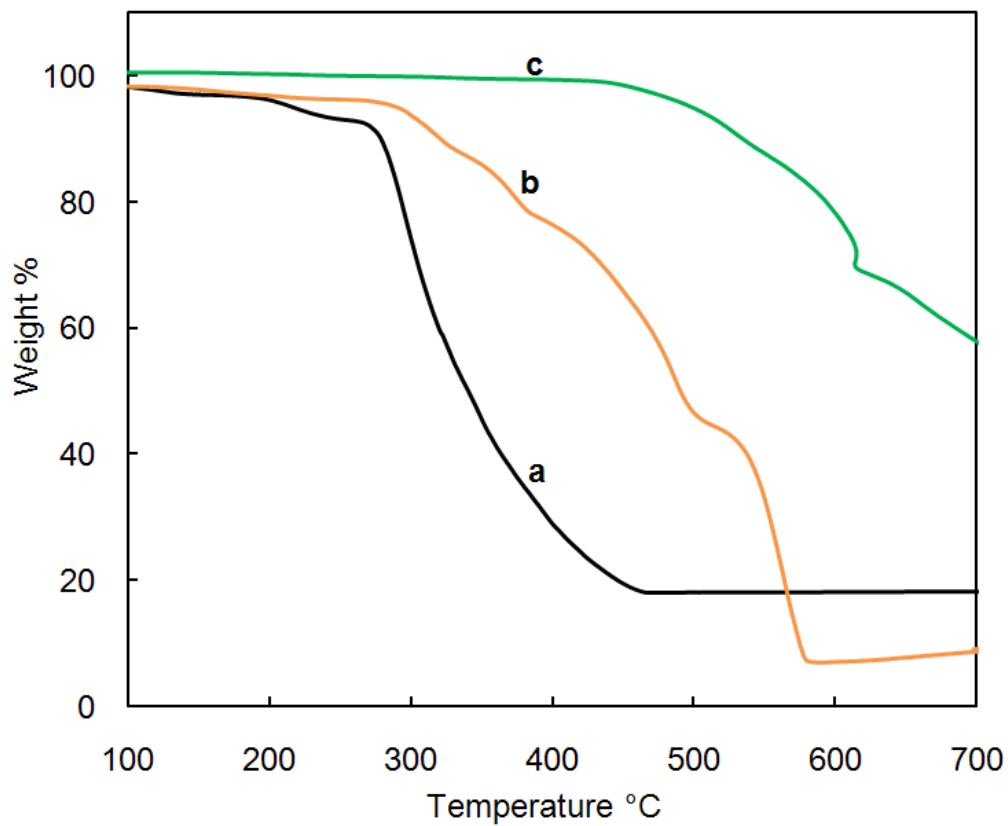
Figure 16. TGA of a) MOP-18 crystals, b) a 80% (w/w) MOP-18/Matrimid$^®$ membrane, and c) Matrimid$^®$ powder.
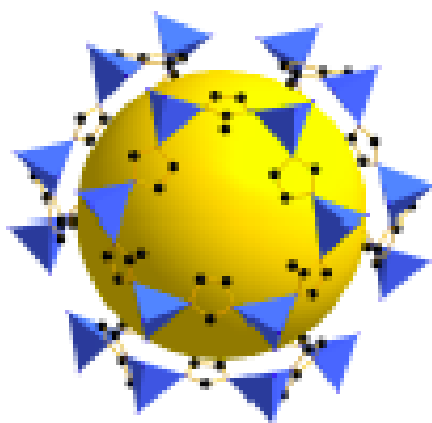
Figure 17. Structure of ZIF-8.
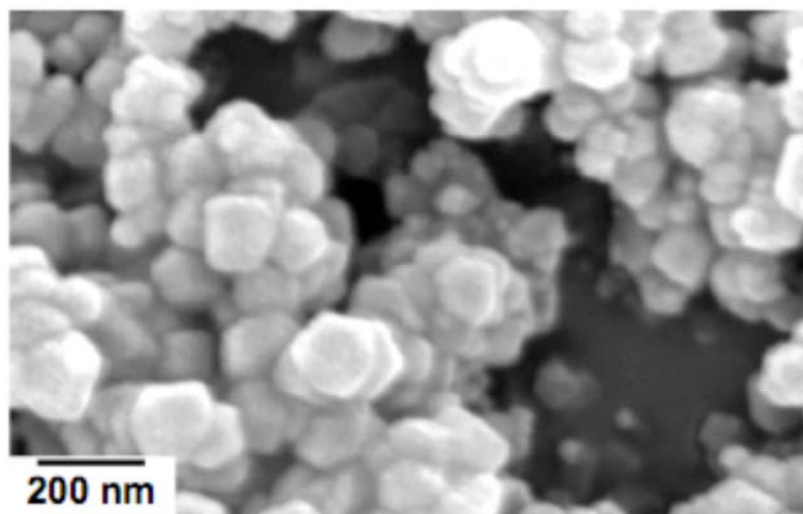
Figure 18.   SEM image of ZIF-8 nanocrystals.
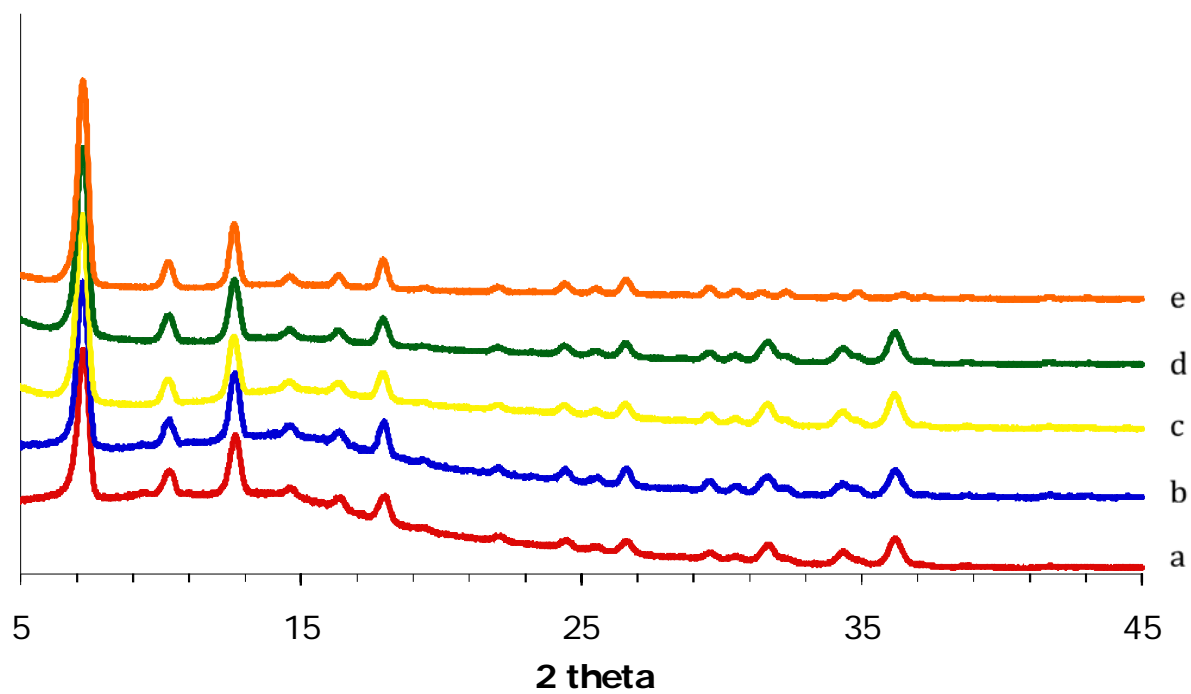
Figure 19.   Normalized XRD plots of ZIF-8/Matrimid® MMMs: a) 20% w/w ZIF-8, b) 30% w/w ZIF-8, c) 40% w/w ZIF-8, d) 50% w/w ZIF-8, and e) 60% w/w ZIF-8.
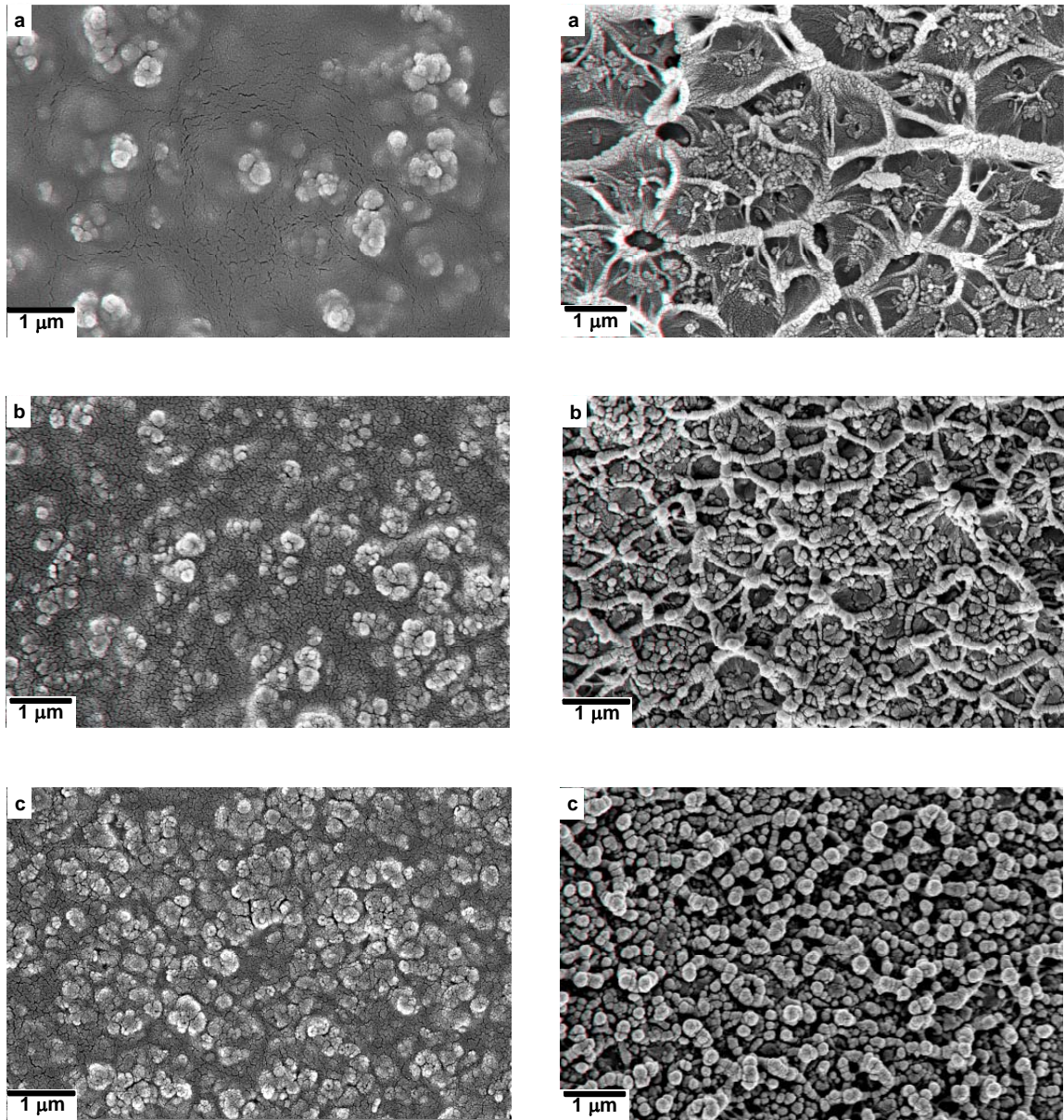
Figure 20.   SEM images of surface (left) and cross-section (right) ZIF-8/Matrimid® mixed matrix membranes: a) 20% w/w ZIF-8 b) 40% w/w ZIF-8 c) 60% w/w ZIF-8.
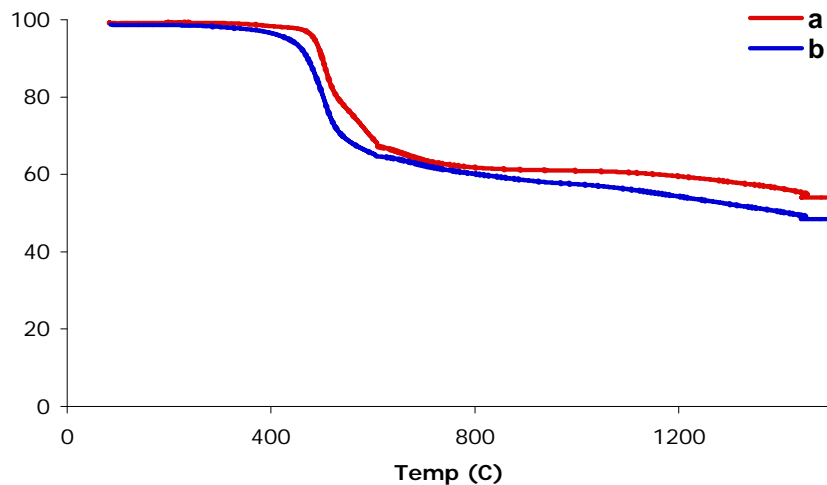
Figure 21.   TGA plot of ZIF-8/Matrimid® membranes: a) Matrimid® b) ZIF-8/Matrimid®
mixed-matrix membranes.
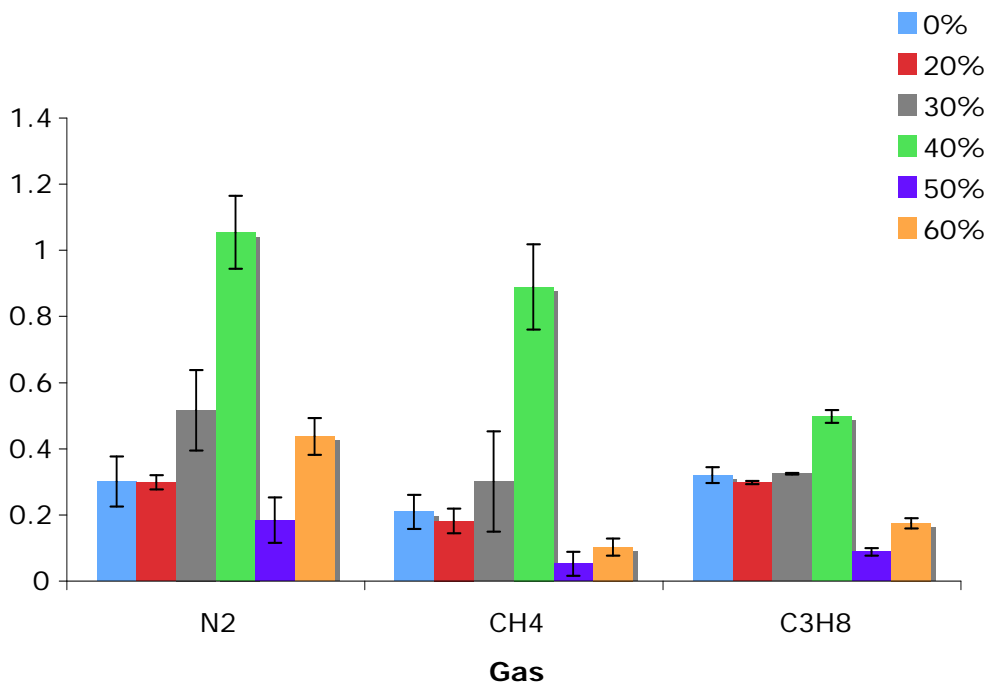
Figure 22.   Permeability plots of ZIF-8/Matrimid® MMMs for N_2, CH_4 and C_3H_8 at 0%, 20%, 30%, 40%, 50% and 60% (w/w) ZIF-8 loadings.
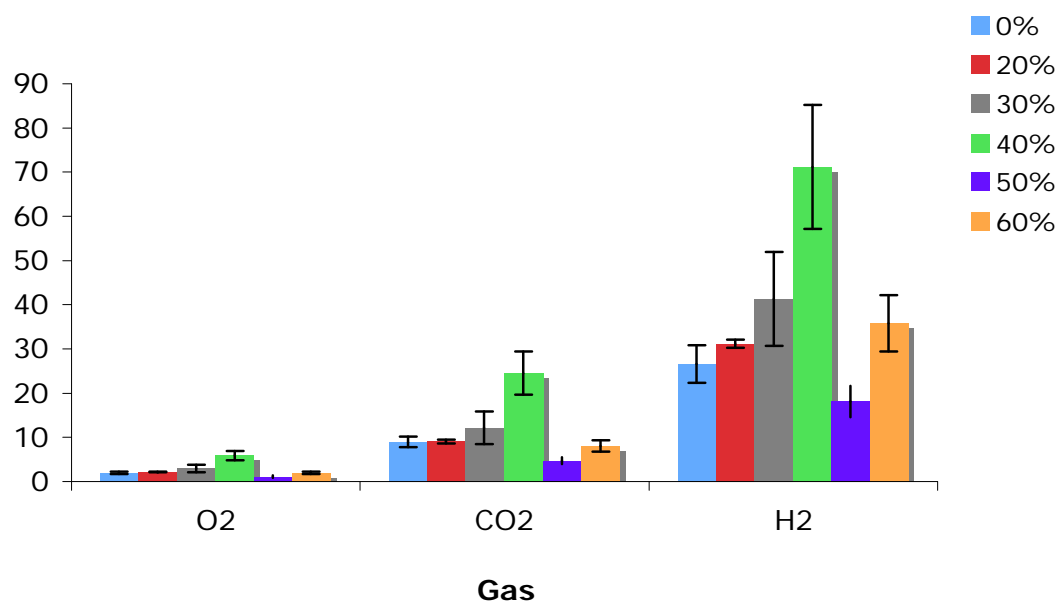
Figure 23. Permeability plots of ZIF-8/Matrimid® MMMs for O_2, CO_2 and H_2 at 0%, 20%, 30%, 40%, 50% and 60% (w/w) ZIF-8 loadings.
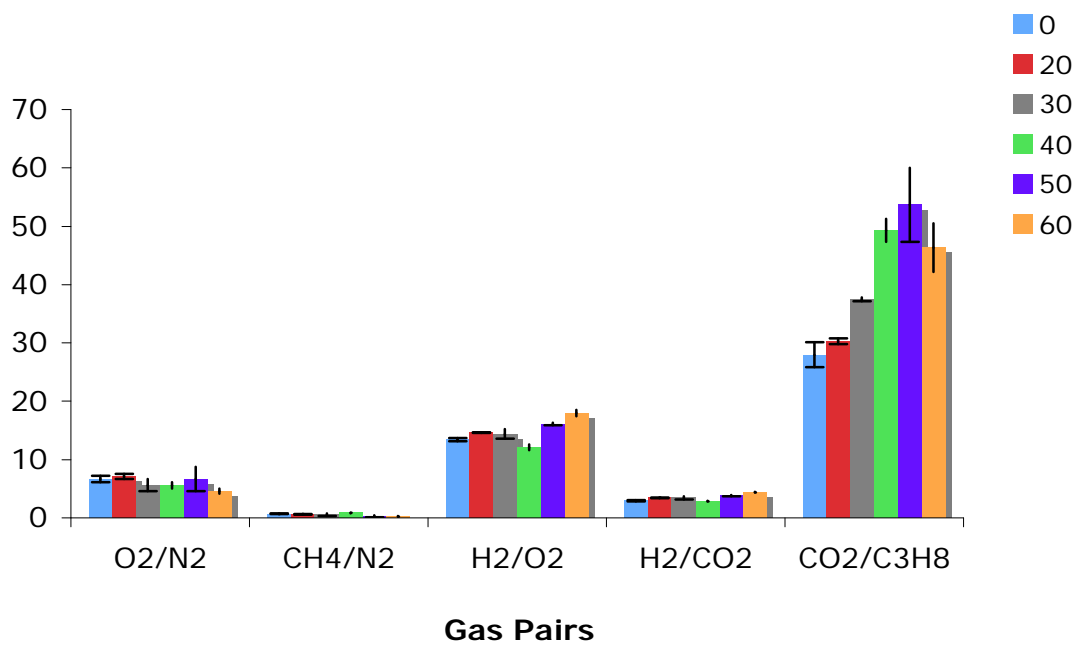
Figure 24. Ideal selectivity plots of ZIF-8/Matrimid® MMMs for O_2/N_2, CH_4/N_2, H_2/O_2, H_2/CO_2, H_2/C_3H_8 at 0%, 20%, 30%, 40%, 50% and 60% (w/w) ZIF-8 loadings.

46
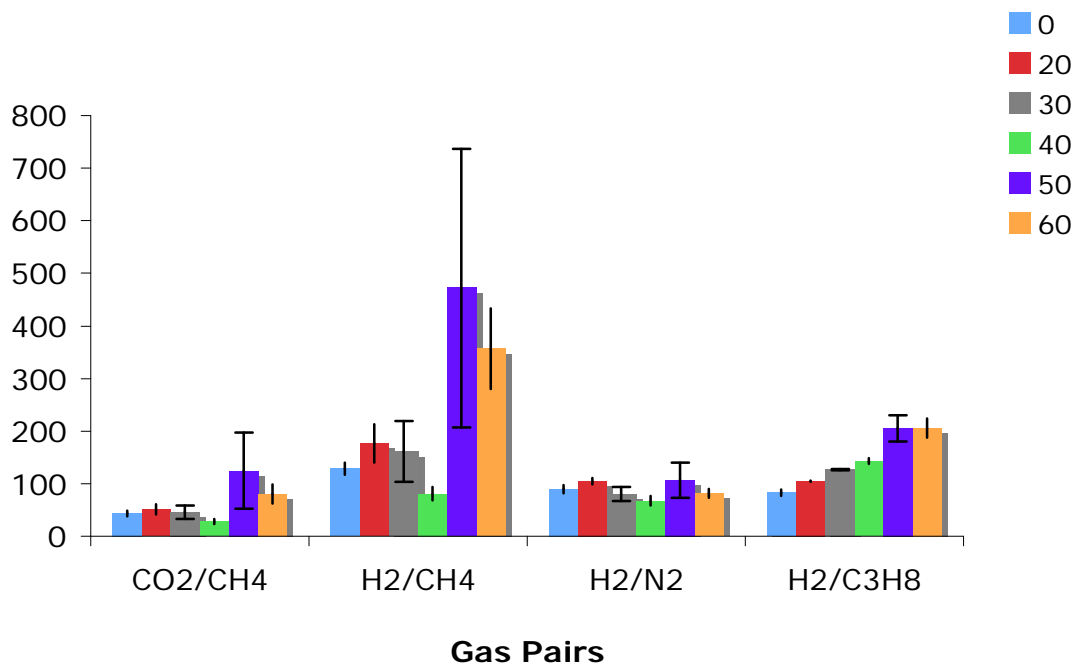
Figure 25.   Ideal selectivity plots of ZIF-8/Matrimid® MMMs for CO_2/CH_4, H_2/CH_4, H_2/N_2 and H_2/C_3H_8. at 0%, 20%, 30%, 40%, 50% and 60% (w/w) ZIF-8 loadings.
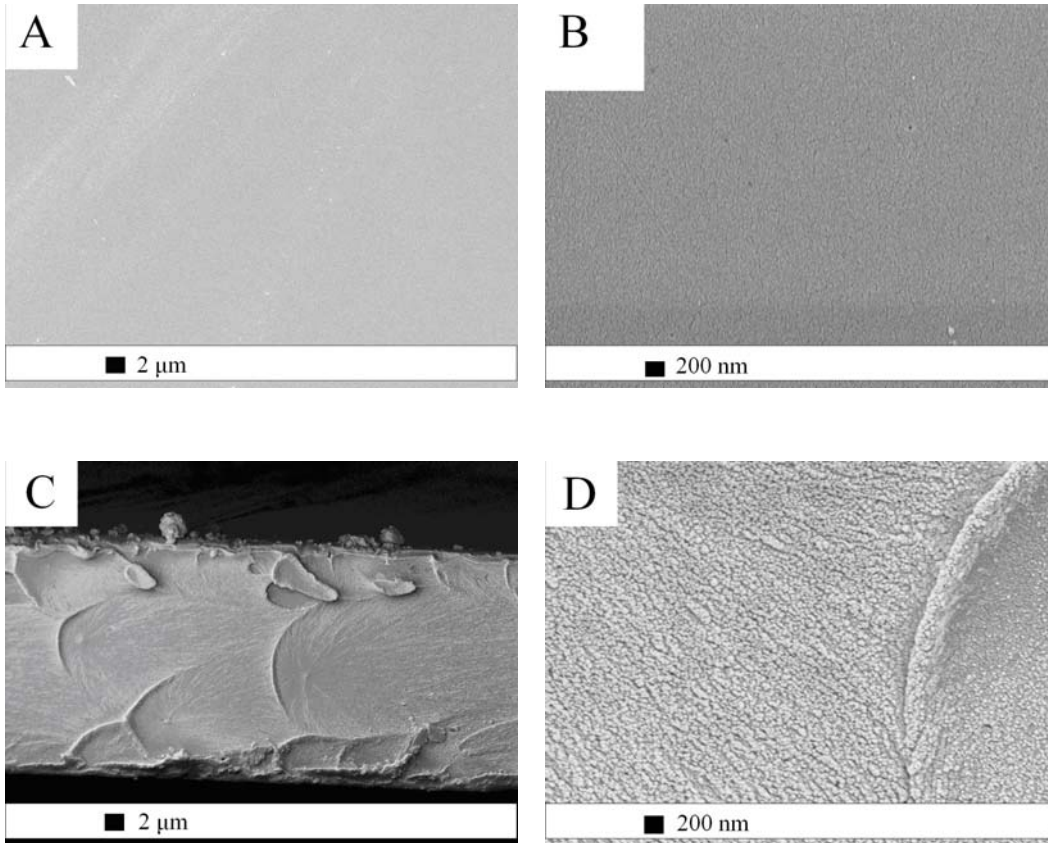
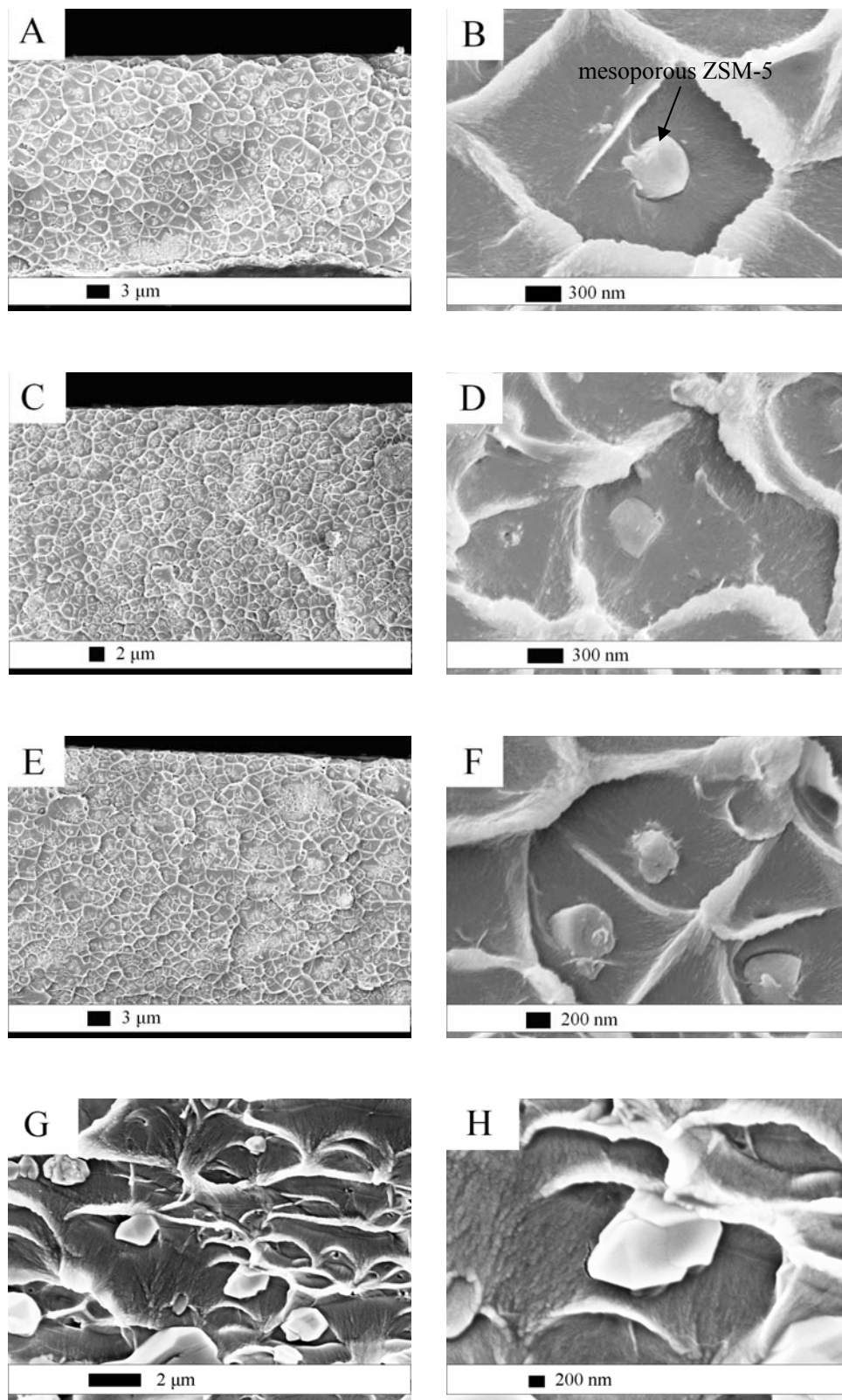Figure 26. SEM images of pure Matrimid®, (a,b) top view, (c,d) cross-section.

Figure 27. SEM images of cross-sections of Matrimid® membranes containing mesoporous ZSM-5, (A) (B) 10 wt%, (C) (D) 20 wt% and (E) (F) 30 wt% and (G)(H) 10 wt% uncalcined mesoporous ZSM-5.
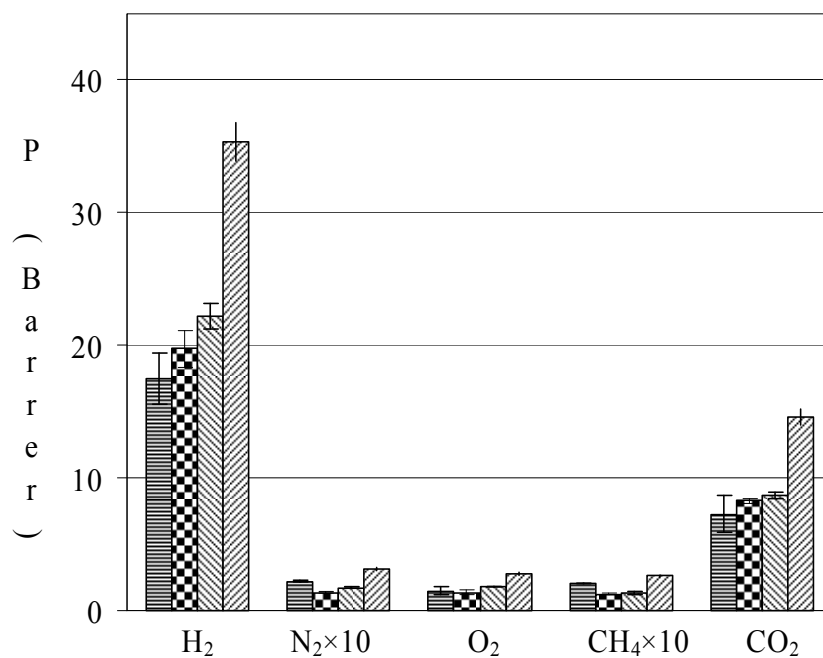
Figure 28. Pure gas permeability of mesoporous ZSM-5/Matrimid[®] membranes at different loadings, ▤ Pure Matrimid[®], ▨ 10 wt %, ▨ 20 wt % and ▨ 30 wt %.
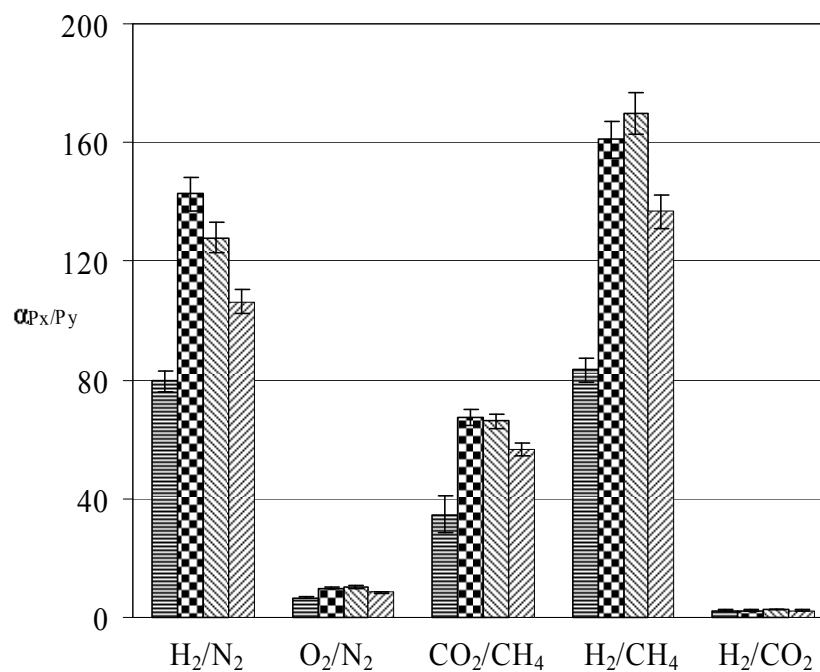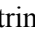

Figure 29. Ideal selectivity of mesoporous ZSM-5/Matrimid[®] membranes at different loadings, ▤ Pure Matrimid[®], ▨ 10 wt %, ▨ 20 wt % and ▨ 30 wt %.
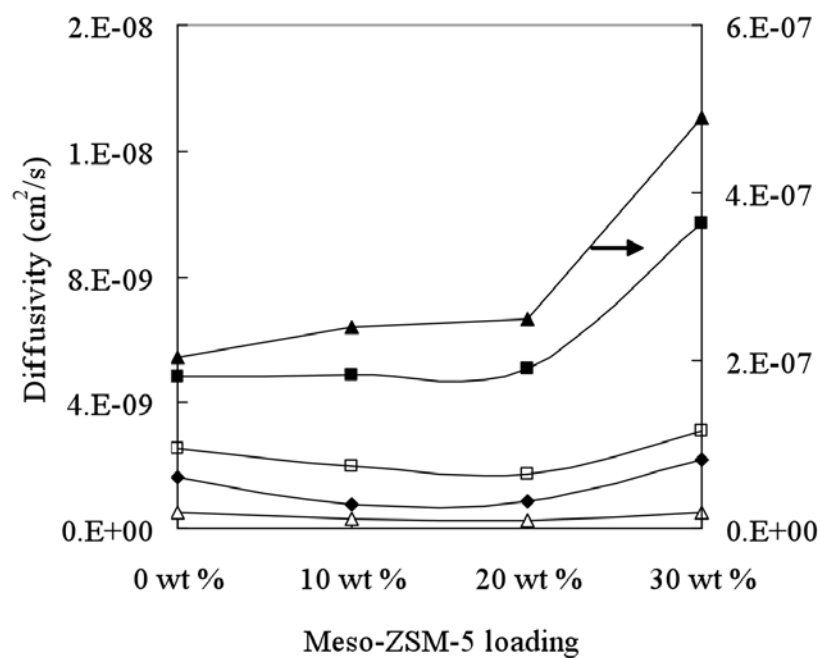
Figure 30. Diffusivity of gases in mesoporous ZSM-5/Matrimid® membranes at different loadings, ■ O_2, □ CO_2, ▲ H_2, ♦ N_2 and Δ CH_4.
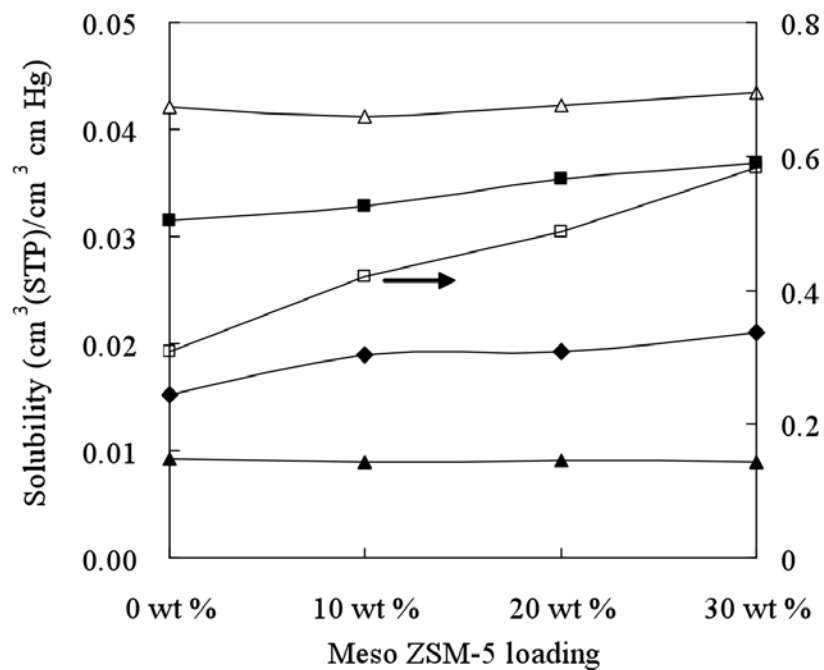
Figure 31. Solubility of gases in mesoporous ZSM-5/Matrimid® membranes at different loadings, ■ O_2, □ CO_2, ▲ H_2, ♦ N_2 and Δ CH_4.
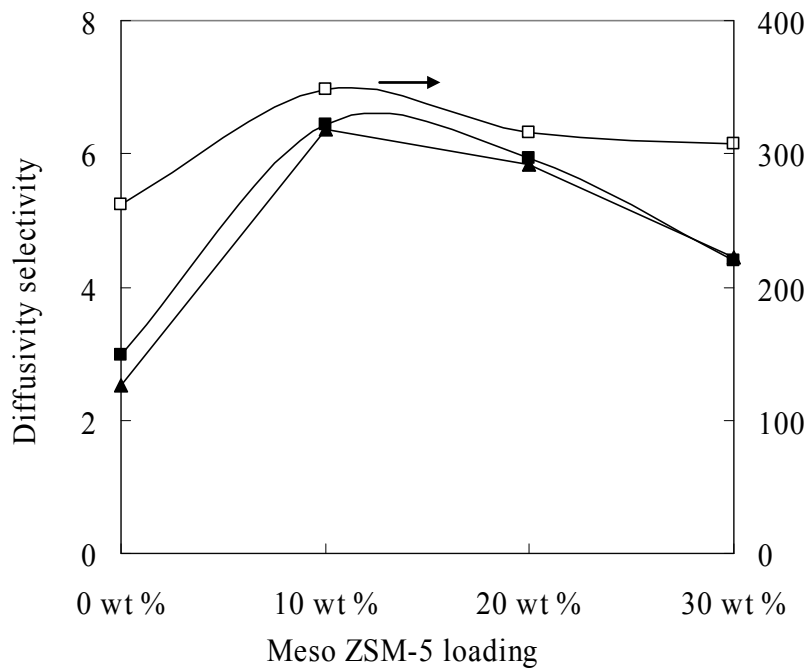
Figure 32. Diffusivity selectivity of mesoporous ZSM-5/Matrimid[®] membranes at different loadings, ■ O_2/N_2, □ CO_2/CH_4 and ▲ H_2/N_2.
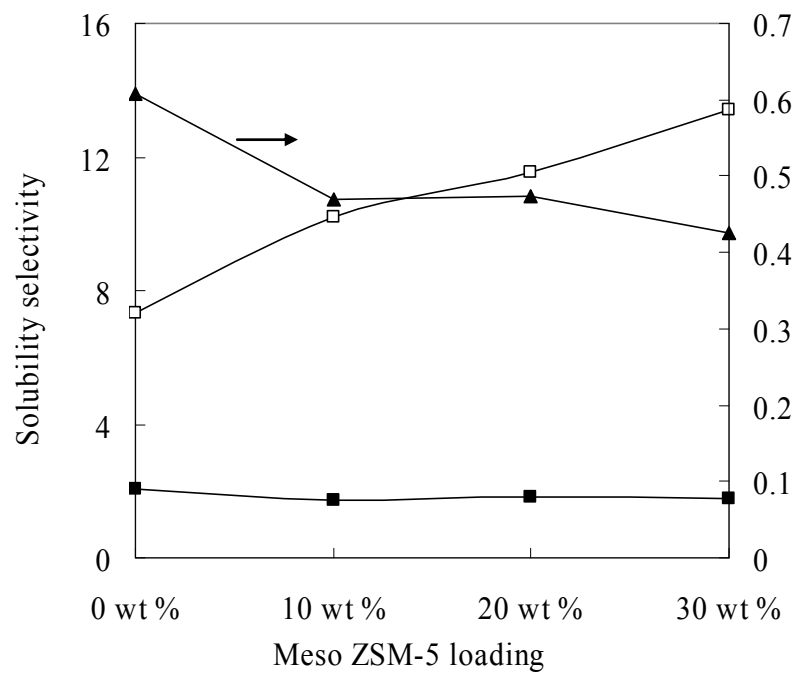
Figure 33. Solubility selectivity of mesoporous ZSM-5/Matrimid[®] membranes at different loadings, ■ O_2/N_2, □ CO_2/CH_4 and ▲ H_2/N_2.
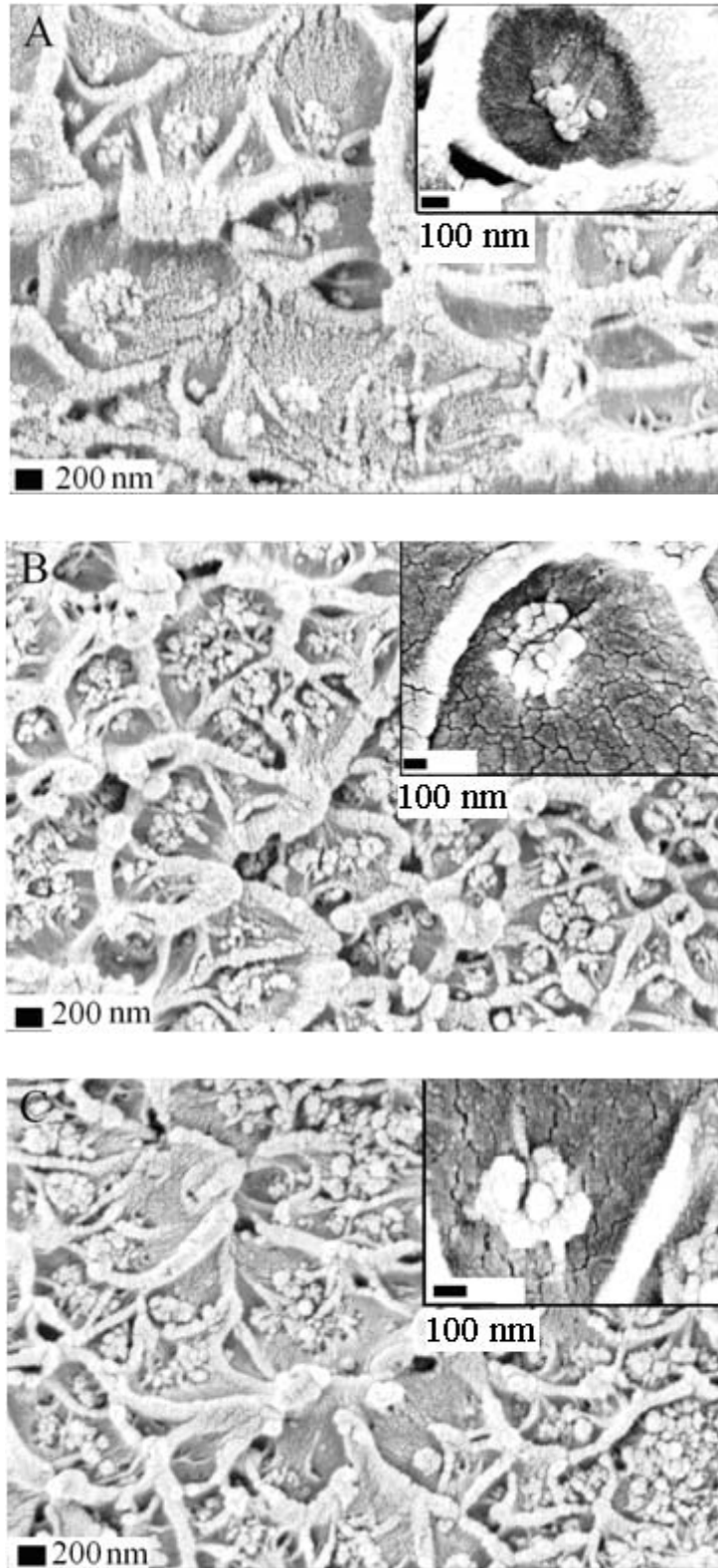
Figure 34. SEM images of carbon aerogel/Matrimid® membrane cross-sections, A) 10%, B) 20%, and C) 30% loading.
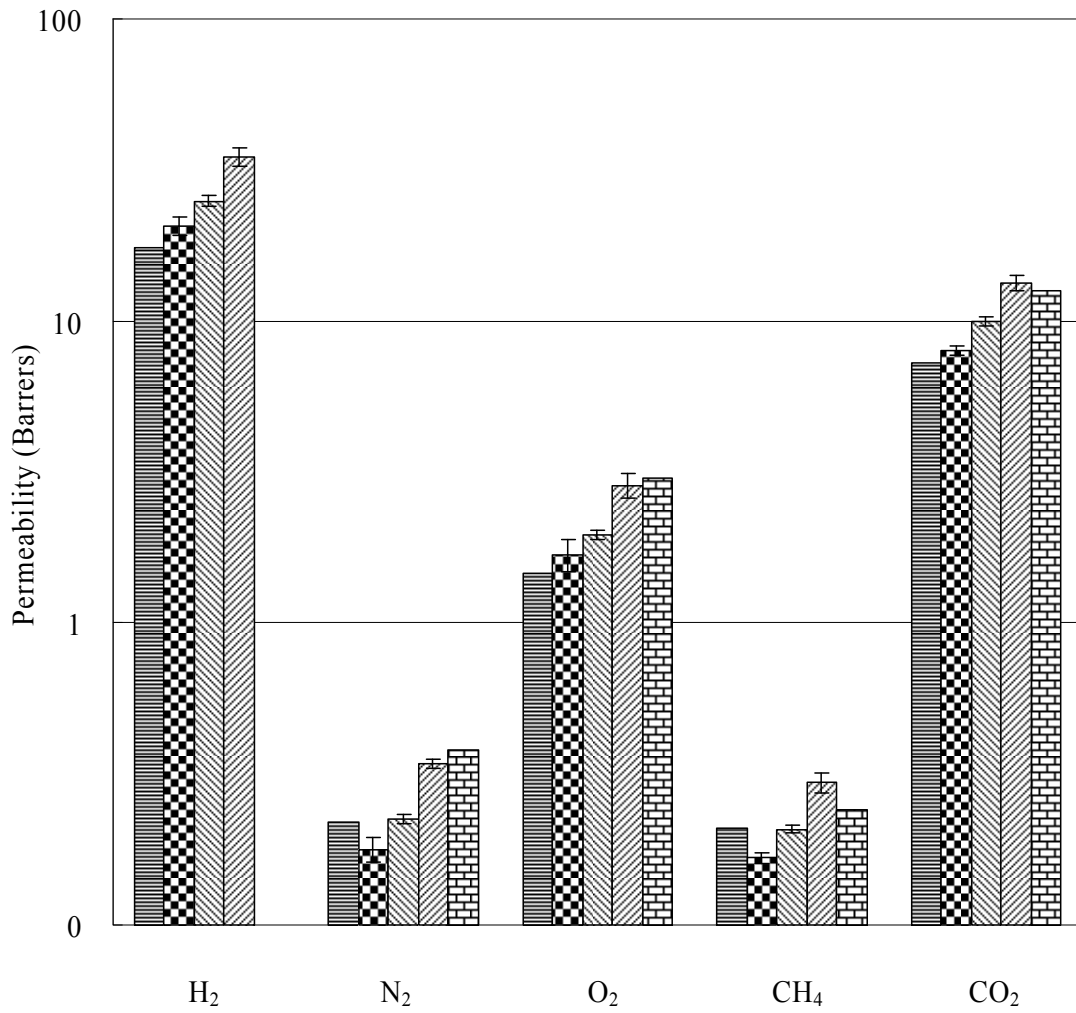
Figure 35. Pure gas permeability of carbon aerogel/Matrimid® membranes at different loadings.
▤ Pure Matrimid®, ▨10 wt %, ▨ 20 wt %, ▨ 30 wt % and ⊞ 40 wt %
CMS/Matrimid®membrane.
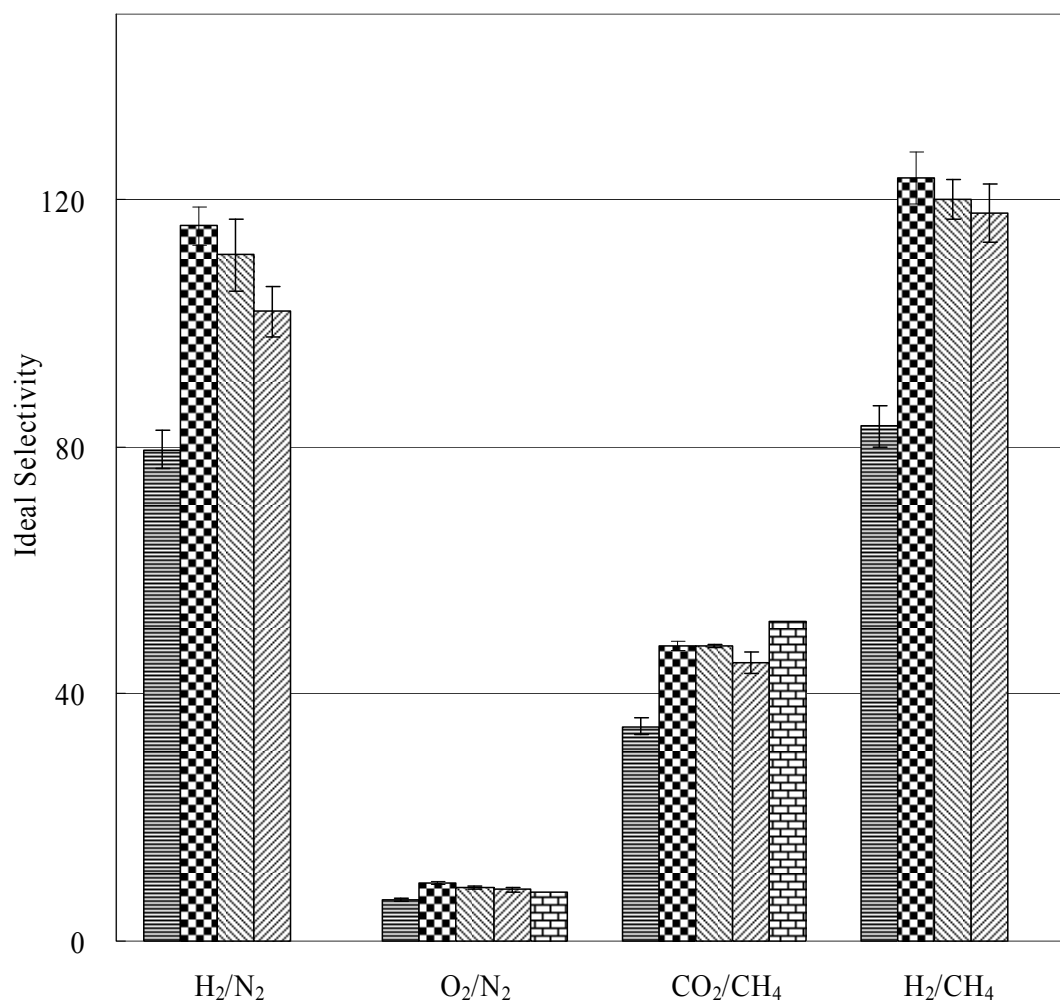
Figure 36. Ideal selectivity of carbon aerogel/Matrimid® membranes at different loadings.
■ Pure Matrimid®, ▨10 wt %, ▨ 20 wt %, ▨ 30 wt % and ⊞ 40 wt % CMS/Matrimid® membrane.
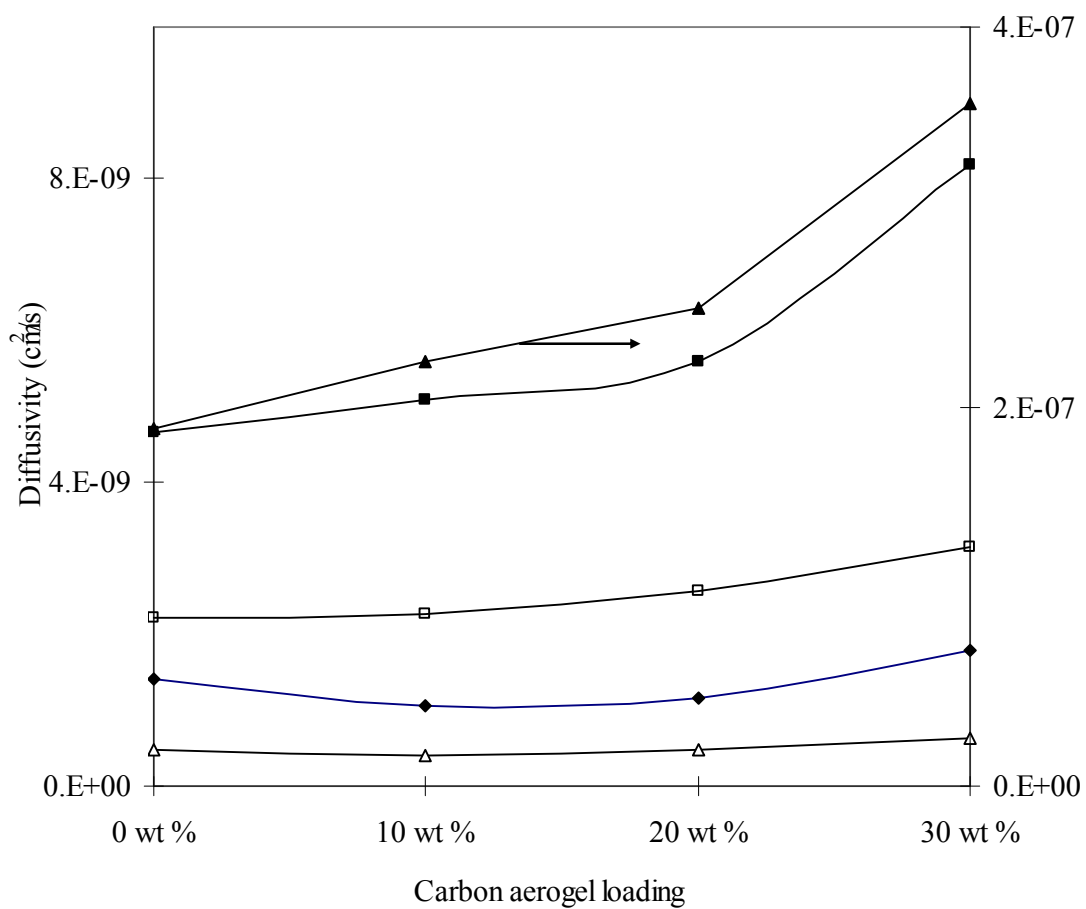
Figure 37. Diffusivity of gases in carbon aerogel/Matrimid® membranes at different loadings.
■ O_2 , □ CO_2 , ▲ H_2 , ♦ N_2 , and Δ CH_4
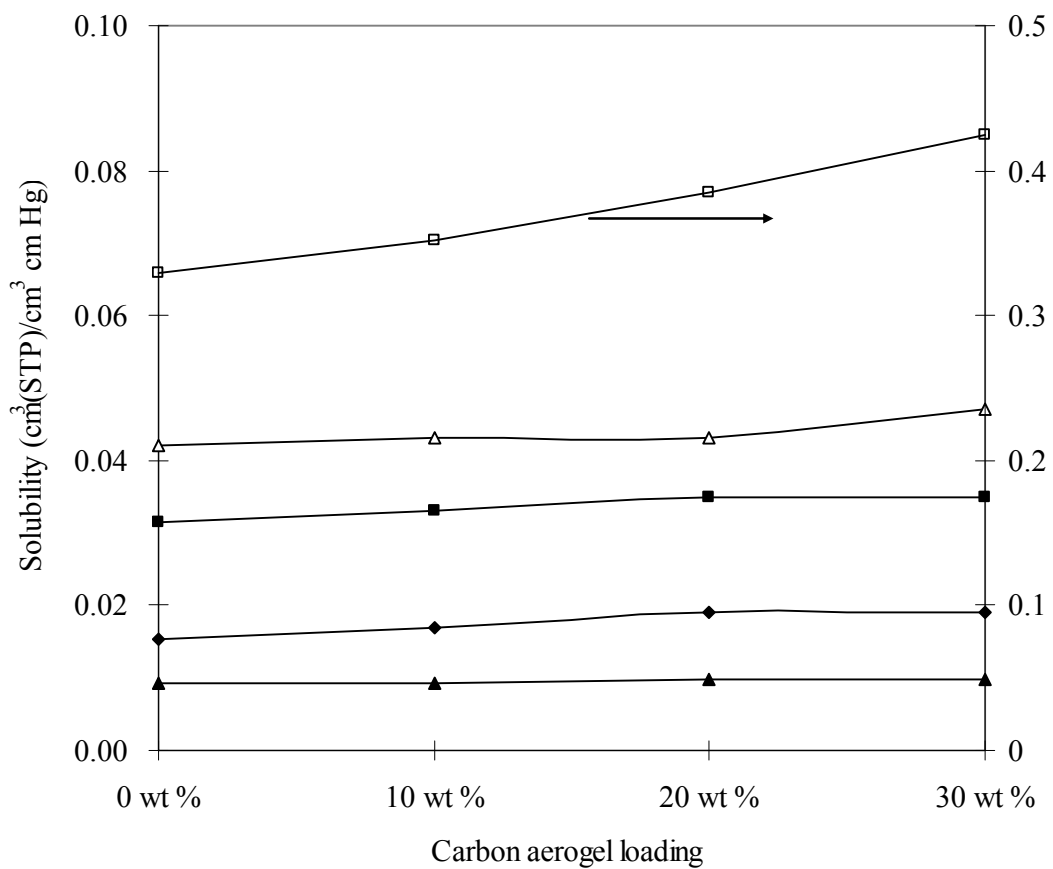
Figure 38. Solubility of gases in carbon aerogel/Matrimid® membranes at different loadings.
■ O_2 , □ CO_2 , ▲ H_2 , ♦ N_2 , and Δ CH_4.
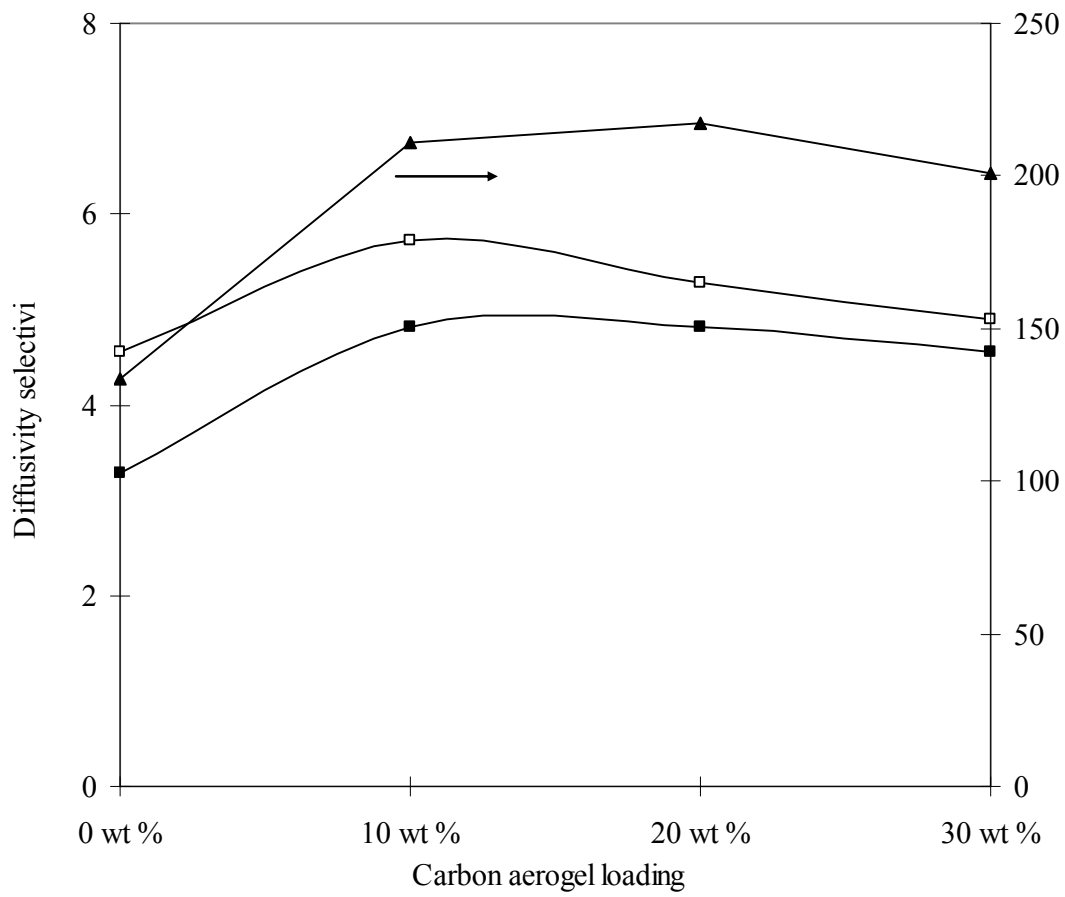
Figure 39. Diffusivity selectivity of carbon aerogel/Matrimid® membrane at different loadings
■ O_2/N_2, □ CO_2/CH_4, and ▲H_2/N_2.
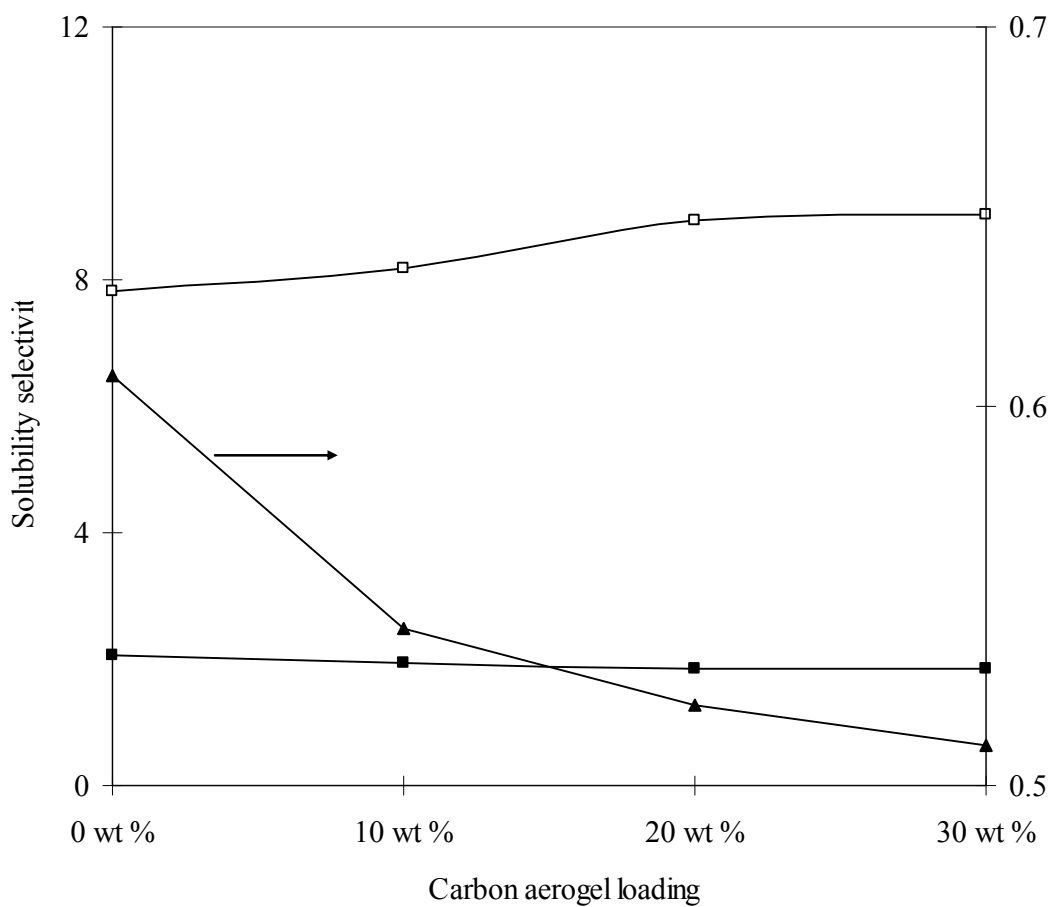
Figure 40. Solubility selectivity of carbon aerogel/Matrimid® membrane at different loadings
■ O_2/N_2, □ CO_2/CH_4, and ▲ H_2/N_2.
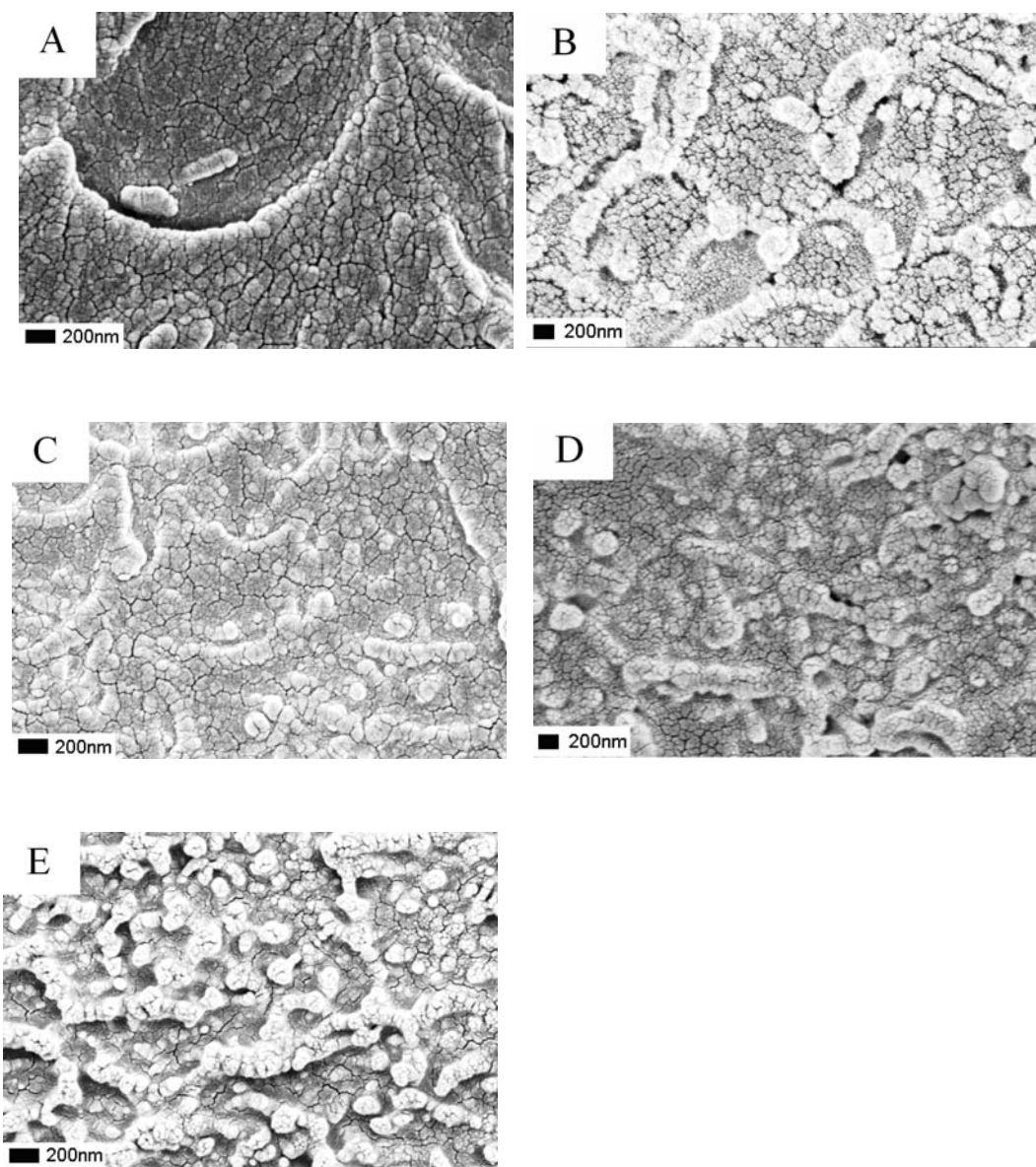
Figure 41. SEM cross-section images of Matrimid®-SWNT-COOH membranes, (a) 1.25 wt % (b) 2.50 wt % (c) 3.0 wt % (d) 4.2 wt % and (e) 10.6 wt %.
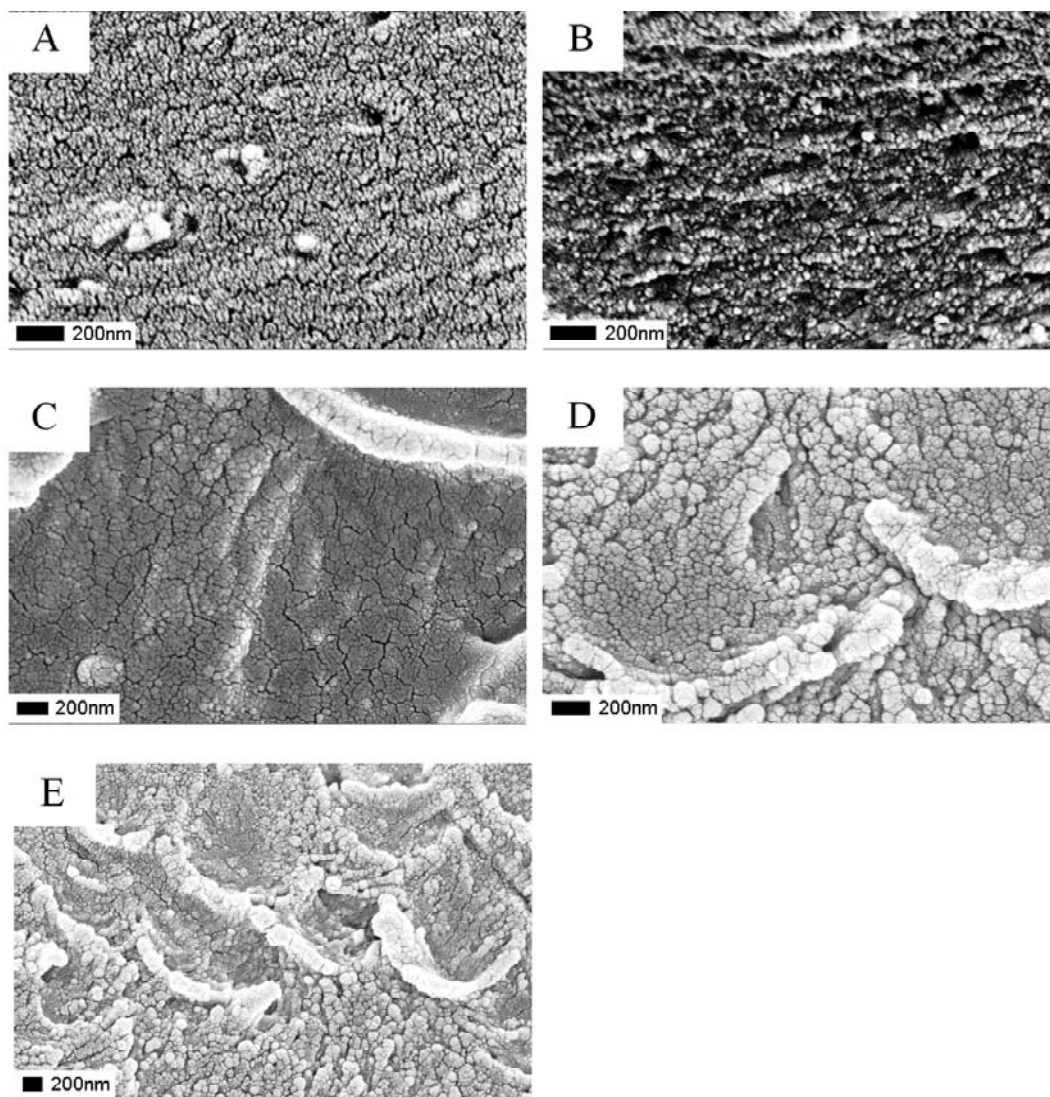
Figure 42. SEM cross-section images of Matrimid®-SWNT-short membranes, (a) 0.6wt % (b) 2.2 wt % (c) 3.2 wt % (d) 3.5 wt % and (e) 4.9 wt %.
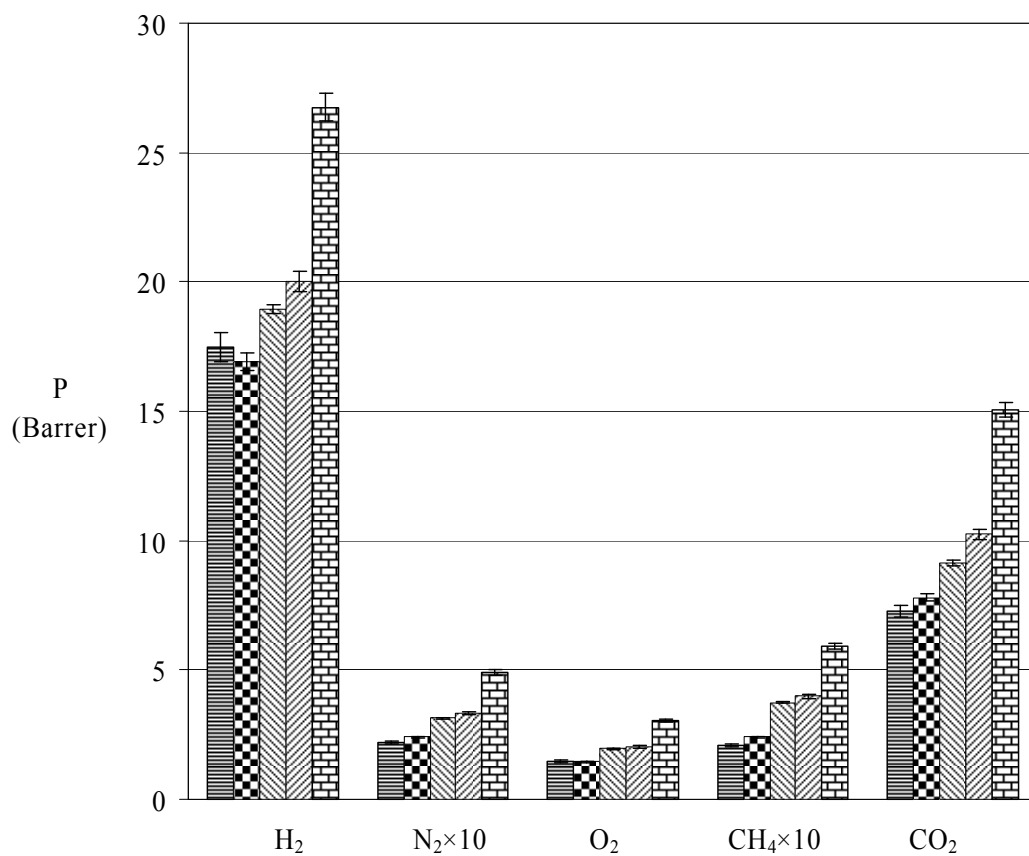
Figure 43. Pure gas permeability of Cu-BPY-HFS/Matrimid® membranes at different loadings, where ▤ Pure Matrimid®, ▨ 10 wt %, ▨ 20 wt %, ▨ 30 wt % and ▦ 40 wt % Cu-BPY-HFS.
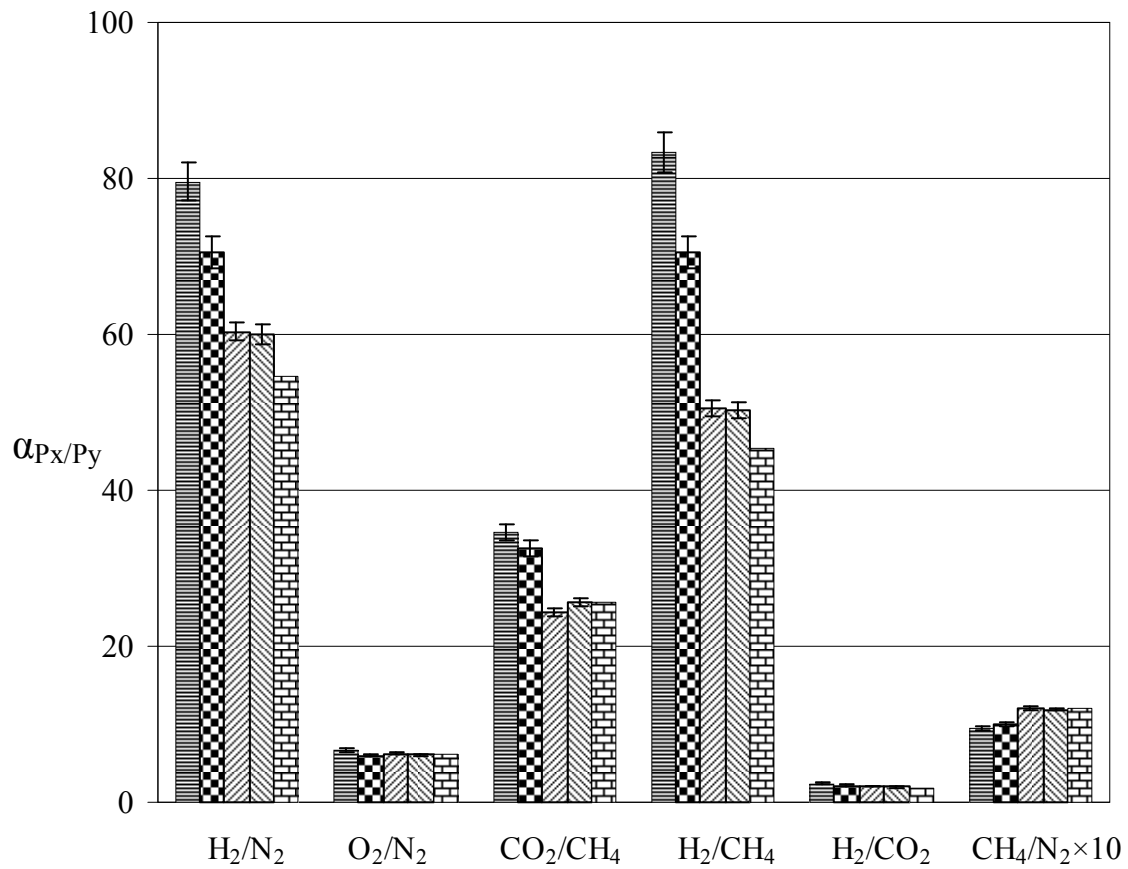
Figure 44. Ideal selectivity of Cu-BPY-HFS/Matrimid® membrane at different loadings, where ▤ Pure Matrimid®, ▨10 wt %, ▨ 20 wt %, ▨ 30 wt % and ⊞ 40 wt % Cu-BPY-HFS.
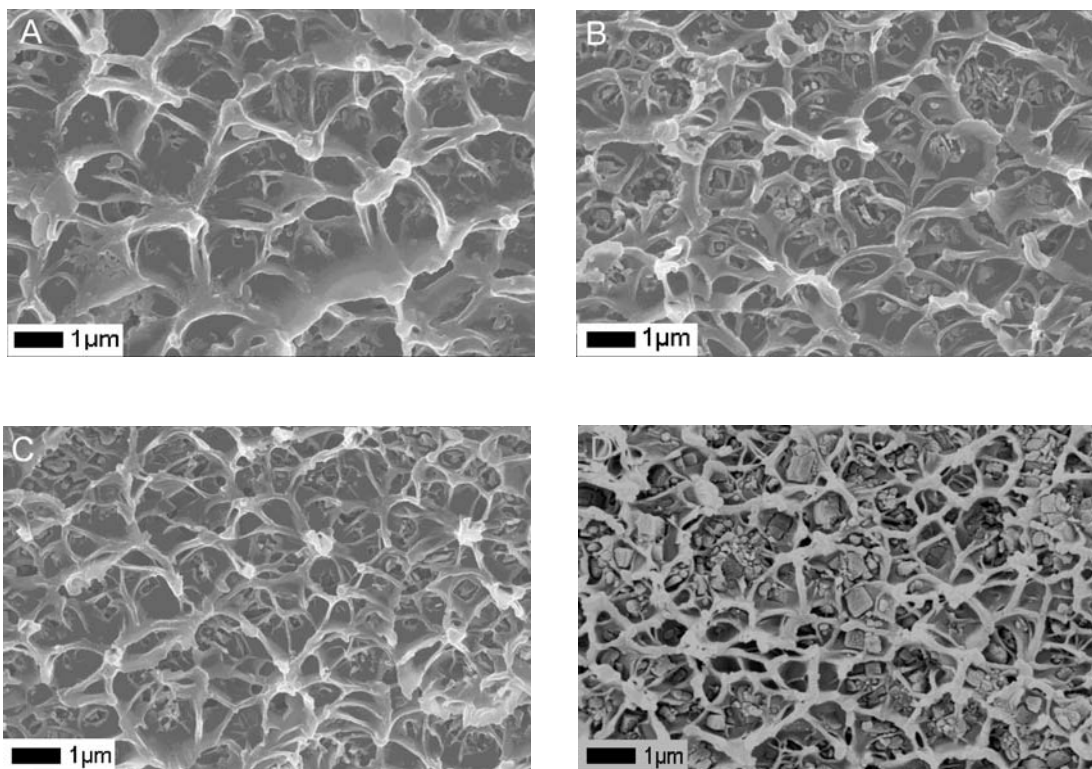
Figure 45. Cross-section view of Cu-BPY-HFS/Matrimid® membrane with different loading, (a) 10 wt %, (b) 20 wt %, (c) 30 wt % and (d) 40 wt %.
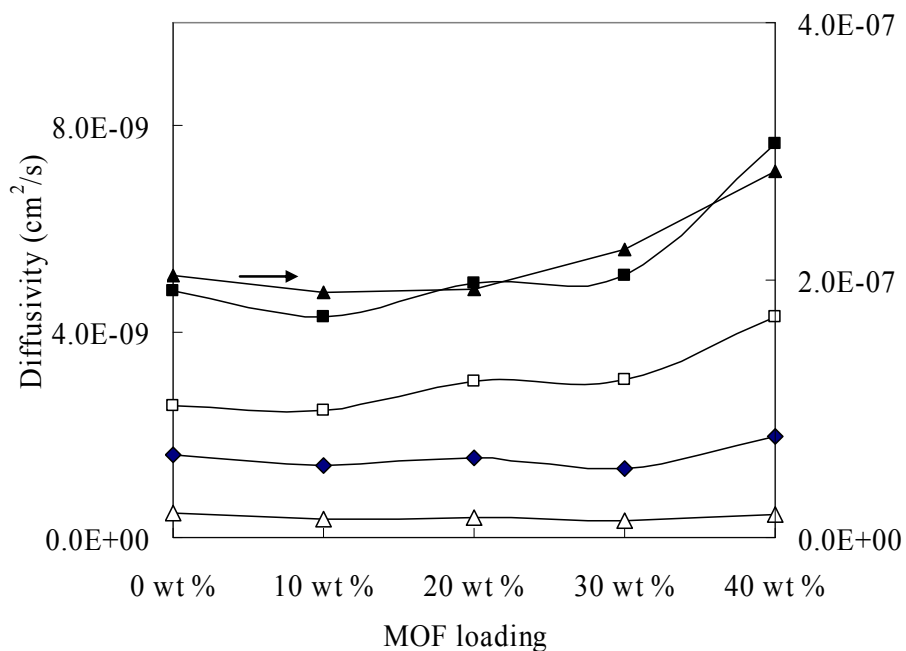
Figure 46. Diffusivity of gases in Cu-BPY-HFS/Matrimid® membranes at different loadings, where ■ O_2, □ CO_2, ▲ H_2, ♦ N_2 and Δ CH_4.
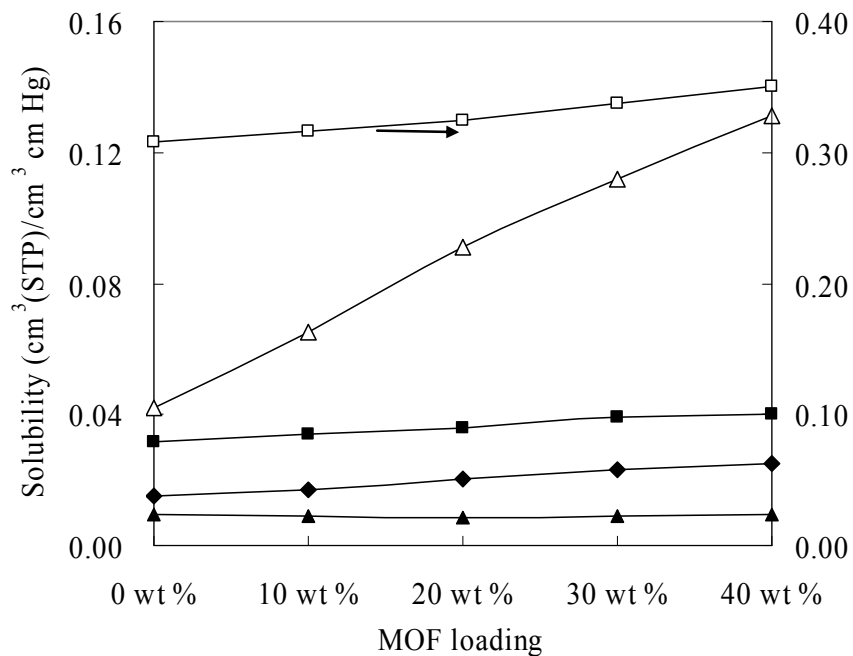
Figure 47. Solubility of gases in Cu-BPY-HFS/Matrimid® membranes at different loading, where ■ O_2, □ CO_2, ▲ H_2, ♦ N_2 and Δ CH_4.
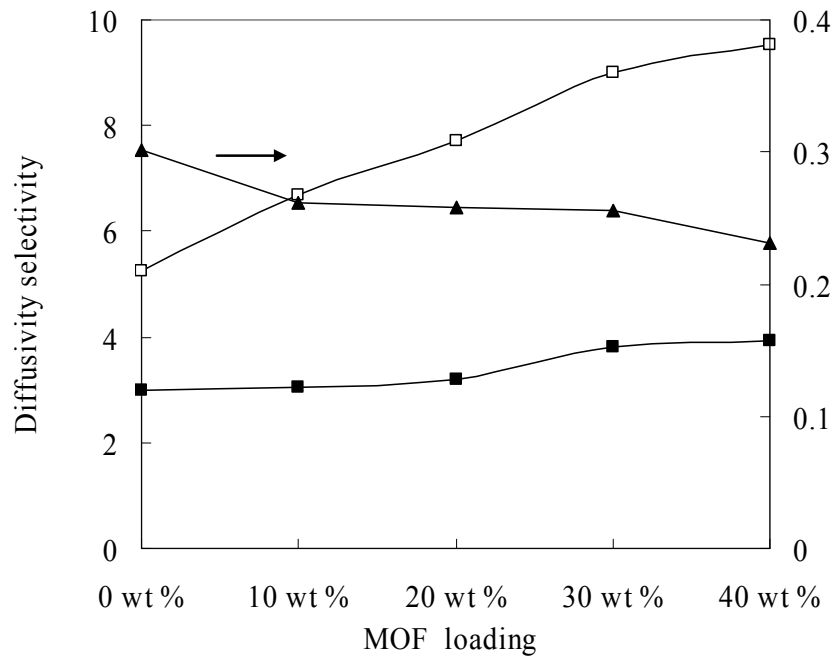
Figure 48. Diffusivity selectivity of Cu-BPY/HFS-Matrimid® membranes at different loadings, where ■ O_2/N_2, □ CO_2/CH_4 and ▲ CH_4/N_2.
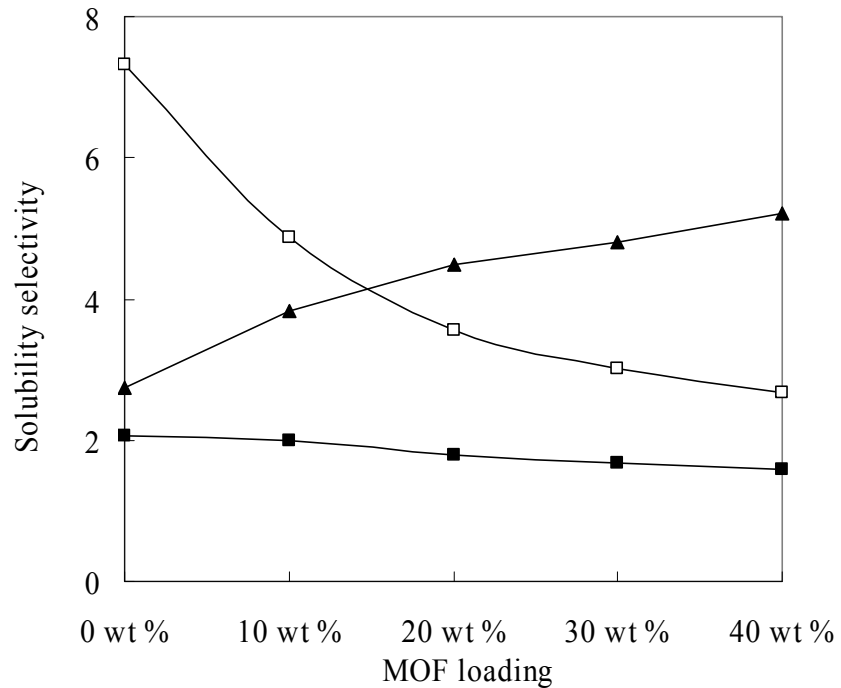
Figure 49. Solubility selectivity of Cu-BPY-HFS/Matrimid® membranes at different loadings, where ■ O_2/N_2 □ CO_2/CH_4 and ▲ CH_4/N_2.
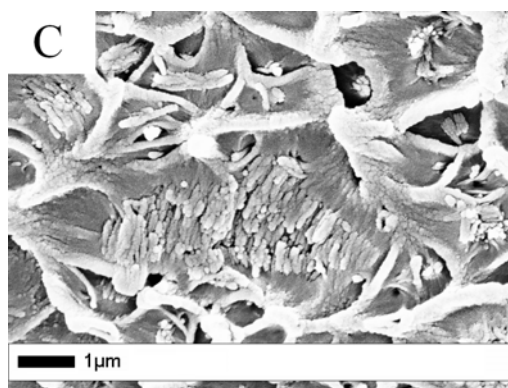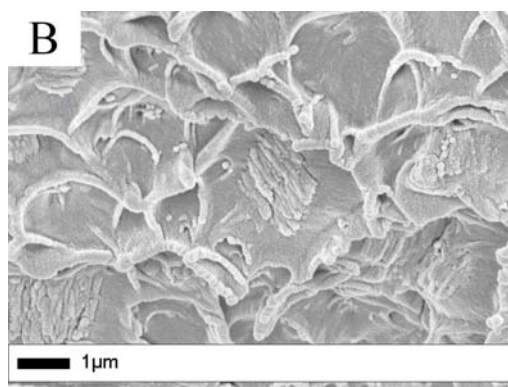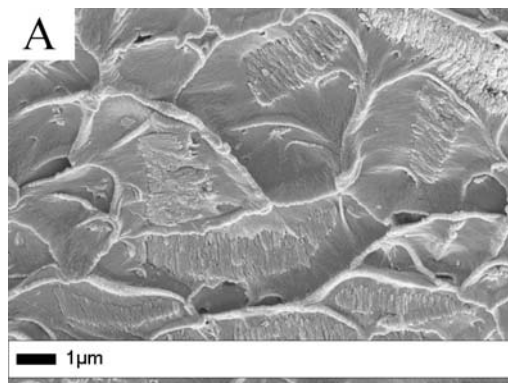
Figure 50. SEM images of MBS/Matrimid® membrane cross-sections, (a) 10 wt%, (b) 20 wt%, and (c) 30 wt%.
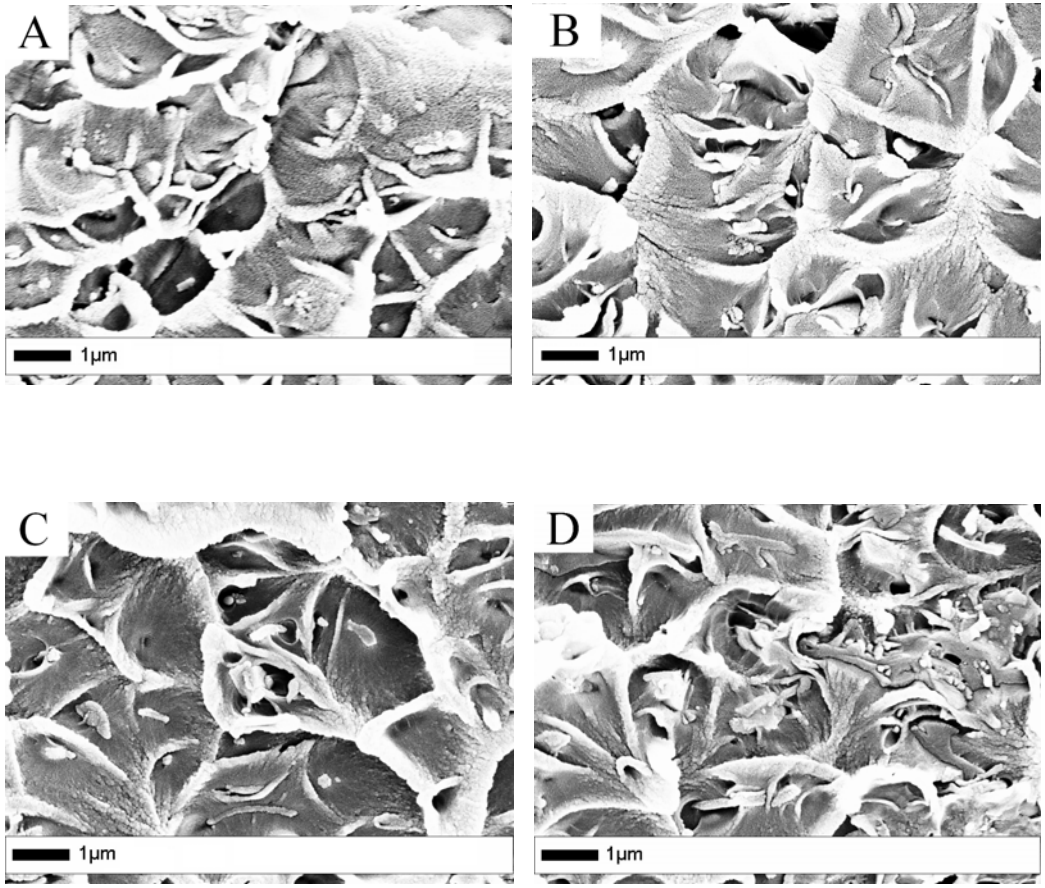
Figure 51. SEM images of PMO-/Matrimid® membrane cross-sections, (a) 10 wt% methylene silica, (b) 10 wt% ethylene silica, (c) 10 wt% ethenylene silica, and (d) 10 wt% phenylene silica.

Table 1. Pure gas permeabilities (Barrers) for MOF-5/Matrimid® mixed-matrix membranes at 35 °C and 2atm.

%MOF-5	P_{H_2}	P_{CO_2}	P_{O_2}	P_{N_2}	P_{CH_4}
0	24.4 ± 0.1	9.0 ± 0.1	1.90 ± 0.01	0.25 ± 0.04	0.22 ± 0.02
10	29.9 ± 4.8	11.1 ± 1.4	2.30 ± 0.30	0.28 ± 0.08	0.22 ± 0.04
20	38.3 ± 8.8	13.8 ± 2.8	2.90 ± 0.60	0.40 ± 0.01	0.34 ± 0.04
30	53.8 ± 3.9	20.2 ± 1.4	4.12 ± 0.37	0.52 ± 0.04	0.45 ± 0.06

Table 2. Pure gas ideal selectivities for MOF-5/Matrimid® mixed-matrix membranes at 35 °C and 2 atm.

%MOF-5	α_{H_2/CH_4}	α_{CO_2/CH_4}	α_{O_2/N_2}	α_{H_2/CO_2}	α_{CH_4/N_2}
0	113.0 ± 9.3	41.7 ± 3.3	7.6 ± 1.0	2.71 ± 0.01	0.86 ± 0.06
10	137.4 ± 43.6	51.0 ± 14.6	8.4 ± 1.3	2.68 ± 0.10	0.86 ± 0.37
20	112.0 ± 12.2	40.5 ± 3.5	7.2 ± 1.2	2.76 ± 0.10	0.85 ± 0.07
30	120.0 ± 7.7	44.7 ± 3.0	7.9 ± 0.1	2.66 ± 0.01	0.87 ± 0.05

Table 3. Separation of gas blends with Matrimid® and 30% MOF-5/Matrimid® mixed-matrix membranes at 35 °C and 2 atm.

Membrane	H_2/CO_2			CO_2/CH_4		CH_4/N_2	
	75/25	50/50	25/75	50/50	10/90	50/50	94/6
Matrimid	2.4 ± 0.3	2.3 ± 0.1	2.5 ± 0.2	38.0 ± 2.0	43.5 ± 1.5	0.82 ± 0.10	0.51 ± 0.05
30% MOF-5/Matrimid	2.2 ± 0.1	2.3 ± 0.2	2.1 ± 0.1	29.0 ± 0.4	38.8 ± 0.5	0.94 ± 0.05	0.50 ± 0.10

Table 4. Permeability (Barrers) of permanent gases and small organic vapors at 35 °C and 2000 Torr in Cu-MOF/Matrimid® MMMs.

wt% Cu-MOF	H_2	CO_2	O_2	N_2	CH_4	Propylene	Propane
0	17.1 ± 1.5	7.33 ± 0.76	1.49 ± 0.16	0.24 ± 0.03	0.22 ± 0.02	0.39 ± 0.03	0.3 ± 001
9	38.1 ± 2.1	20.54 ± 0.54	3.86 ± 0.09	0.66 ± 0.01	0.66 ± 0.04		
17	81.2 ± 9.2	38.27 ± 5.89	7.92 ± 1.05	1.33 ± 0.2	1.32 ± 0.21		
23	158.5 ± 60.0	74.08 ± 42.38	17.16 ± 8.2	3.44 ± 1.83	3.63 ± 2.19	5.13 ± 3.46	2.04 ± 0.77
29	381.2 ± 13.8	233.9 ± 4.84	62.19 ± 6.17	19.89 ± 3.86	24.63 ± 4.73	89.40	27.60
33	774.1 ± 2.5	465.0 ± 131.5	182.77 ± 16.4	102.3 ± 0.66	127.43 ± 24.14	293.5 ± 76.1	175.5 ± 38.8
45	4077.9 ± 387.3	3130.0 ± 170.5	1602.2 ± 417.8	1204.0 ± 714.2	1659.4 ± 1241.7	4984.5 ± 272.2	4170 ± 223.5
45-C_{60}	1224	986	265	92	131	1145	1785

Table 5. Facilitation ratios of permanent gases and small organic vapors in Cu-MOF/Matrimid® MMMs at 2000 Torr and 35 °C.

wt% Cu-MOF	H_2	CO_2	O_2	N_2	CH_4	Propylene	Propane
9	1.2	1.8	1.6	1.7	1.9		
17	3.8	4.2	4.3	4.5	4.9		
23	8.3	9.1	10.5	13.2	15.3	12.2	5.7
29	21.3	30.9	40.7	80.9	109.5	228.2	90.5
33	44.3	62.5	121.6	420.2	570.6	751.5	580.9
45	237.7	426.2	1074.0	4956.1	7442.4	12779.8	13829.8
45-C_{60}	70.6	134.1	176.9	417.2	594.5	2934.9	5949.0

Table 6. Ideal selectivities of permanent gases and small organic vapors at 35 °C and 2000 Torr in Cu-MOF/Matrimid® MMMs.

wt% Cu-MOF	H_2/CH_4	H_2/N_2	CO_2/CH_4	H_2/O_2	O_2/N_2	H_2/CO_2	CH_4/N_2	C_3H_6/C_3H_8	C_3H_6/N_2	C_3H_8/N_2
0	76.64 ± 0.47	70.46 ± 2.15	32.86 ± 0.07	11.47 ± 0.14	6.14 ± 0.11	2.33 ± 0.02	0.92 ± 0.02	1.29 ± 0.11	1.61 ± 0.07	1.25 ± 0.16
9	58.16 ± 6.41	58.05 ± 1.93	31.31 ± 0.89	9.85 ± 0.31	5.89 ± 0.01	1.86 ± 0.15	1 ± 0.08			
17	61.79 ± 3.93	61.2 ± 2.94	28.99 ± 0.39	10.27 ± 0.31	5.96 ± 0.11	2.13 ± 0.11	0.99 ± 0.02			
23	47.24 ± 11.96	48.23 ± 8.23	20.63 ± 0.76	9.48 ± 1.04	5.07 ± 0.31	2.28 ± 0.5	1.03 ± 0.09	2.37 ± 0.81	1.42 ± 0.25	0.62 ± 0.11
29	15.72 ± 2.46	19.46 ± 3.08	9.66 ± 1.66	6.15 ± 0.39	3.16 ± 0.3	1.63 ± 0.03	1.24 ± 0	3.24	3.95	1.22
33	6.18 ± 1.15	7.57 ± 0.07	3.62 ± 0.35	4.25 ± 0.37	1.79 ± 0.17	1.73 ± 0.48	1.25 ± 0.24	1.67 ± 0.07	2.87 ± 0.76	1.72 ± 0.39
45	3.41 ± 2.11	4.62 ± 3.33	2.66 ± 1.71	2.64 ± 0.62	1.63 ± 0.78	1.3 ± 0.05	1.36 ± 0.34	1.2 ± 0	3.27 ± 0.75	2.74 ± 0.63
45-C_{60}	9.37	13.33	7.54	4.62	2.89	1.24	1.42	0.64	12.46	19.43
Knudsen	2.82	3.74	0.60	4.00	0.93	4.70	1.32	1.02	0.81	0.79

Table 7. Separation of gas mixtures at 35 °C and 2000 Torr in Cu-MOF/ Matrimid® MMMs.

Gas Mixture	Matrimid	23 wt% Cu-MOF	33 wt% Cu-MOF	45 wt% Cu-MOF	45-C_{60} wt% Cu-MOF
H_2/CO_2	Ideal = 2.34 ± 0.02	Ideal = 2.28 ± 0.49	Ideal = 1.74 ± 0.49	Ideal = 1.3 ± 0.05	Ideal = 1.24
25%/75%	1.8 ± 0.14	2 ± 0.42	1.6 ± 0.42	1.5 ± 0.14	
50%/50%	1.75 ± 0.07	2.05 ± 0.64	1.8 ± 0.57	1.45 ± 0.21	1.4
75%/25%	2 ± 0.28	2.05 ± 0.35	1.65 ± 0.49	1.85 ± 0.64	
CH_4/N_2	Ideal = 0.92 ± 0.03	Ideal = 1.03 ± 0.08	Ideal = 1.25 ± 0.25	Ideal = 1.36 ± 0.34	Ideal = 1.42
50%/50%	1.04 ± 0.05	1.25 ± 0.24	1.63 ± 0.36	2.07 ± 0.24	1.63
94%/6%	0.61 ± 0.06	0.8 ± 0.08	0.99 ± 0.06	0.81 ± 0.18	
CO_2/CH_4	Ideal = 32.86 ± 0.07	Ideal = 20.63 ± 0.76	Ideal = 3.62 ± 0.35	Ideal = 2.66 ± 1.71	Ideal = 7.54
10%/90%	38.85 ± 2.62	28.4 ± 12.87	4.8 ± 3.25	5.3 ± 5.37	
50%/50%	44.8 ± 2.69	26.15 ± 6.15	4.2 ± 2.12	4.15 ± 4.31	6.7
C_3H_6/C_3H_8	Ideal = 1.3 ± 0.11	Ideal = 2.35 ± 0.78	Ideal = 1.67 ± 0.06	Ideal = 1.2 ± 0	Ideal = 0.64
50%/50%	6.1 ± 2.69	23.3 ± 25.74	1.13 ± 0.04	1.2 ± 0.28	1.4

Table 8.   Permeability (Barrers) of permanent gases and small organic vapors at 35 °C and 2000 Torr in MOP-18/Matrimid® MMMs.

wt% MOP-18	H_2	CO_2	O_2	N_2	CH_4	Propylene	Propane
0	17.1 ± 1.5	7.3 ± 0.7	1.49 ± 0.16	0.24 ± 0.03	0.22 ± 0.02	0.39 ± 0.03	0.3 ± 0.01
23	17.8 ± 1.9	9.4 ± 1.2	1.8 ± 0.2	0.34 ± 0.06	0.41 ± 0.05	0.66 ± 0.04	0.13 ± 0.04
33	22.3 ± 0.6	14.0 ± 1.3	2.6 ± 0.2	0.61 ± 0.01	0.65 ± 0.12	1.22 ± 0.33	0.23 ± 0.04
45	22.3 ± 0.6	15.6 ± 0.9	2.9 ± 0.2	0.60 ± 0.05	0.95 ± 0.04	3.40 ± 0.23	1.60 ± 0.42

Table 9. Facilitation ratios of permanent gases and small organic vapors in MOP-18/Matrimid® MMMs at 2000 Torr and 35 °C.

wt% MOP-18	H_2	CO_2	O_2	N_2	CH_4	Propylene	Propane
23	0.04	0.29	0.21	0.42	0.86	0.69	-0.57
33	0.30	0.92	0.74	1.54	1.95	2.13	-0.23
45	0.30	1.14	0.95	1.50	3.32	7.72	4.33

Table 10.   Ideal selectivities of permanent gases and small organic vapors at 35 °C and 2000 Torr in MOP-18/Matrimid® MMMs.

wt% MOP-18	H_2/CH_4	H_2/N_2	CO_2/CH_4	H_2/O_2	O_2/N_2	H_2/CO_2	CH_4/N_2	C_3H_6/C_3H_8	C_3H_6/N_2	C_3H_8/N_2
0	76.64 ± 0.47	70.46 ± 2.15	32.86 ± 0.07	11.47 ± 0.14	6.14 ± 0.11	2.33 ± 0.02	0.92 ± 0.02	1.29 ± 0.11	1.61 ± 0.07	1.25 ± 0.16
23	44.55 ± 0.55	53.65 ± 4.35	23.19 ± 0.31	9.60 ± 0.11	5.59 ± 0.39	1.90 ± 0.05	1.22 ± 0.08	5.45 ± 1.20	1.99 ± 0.25	0.37 ± 0.04
33	35.01 ± 5.35	36.66 ± 0.67	21.87 ± 2.00	8.53 ± 0.34	4.30 ± 0.25	1.60 ± 0.10	1.06 ± 0.18	5.24 ± 0.48	2.00 ± 0.57	0.38 ± 0.07
45	23.52 ± 0.38	38.10 ± 2.31	16.47 ± 0.20	7.74 ± 0.31	4.92 ± 0.10	1.43 ± 0.04	1.62 ± 0.07	2.18 ± 0.44	5.79 ± 0.13	2.71 ± 0.48
Knudsen	2.82	3.74	0.60	4.00	0.93	4.70	1.32	1.02	0.81	0.79

Table 11.   Separation of gas mixtures at 35 °C and 2000 Torr in MOP-18/Matrimid® MMMs.

Gas Mixture	Matrimid®	33 wt% MOP-18	45 wt% MOP-18
H_2/CO_2	Ideal = 2.34 ± 0.02	Ideal = 1.91 ± 0.05	Ideal = 1.43 ± 0.04
50%/50%	1.75 ± 0.07	1.6 ± 0.42	1.35 ± 0.07
CH_4/N_2	Ideal = 0.92 ± 0.03	Ideal = 1.22 ± 0.08	Ideal = 1.62 ± 0.07
50%/50%	1.04 ± 0.05	1.34 ± 0.03	
CO_2/CH_4	Ideal = 32.86 ± 0.07	Ideal = 23.27 ± 0.42	Ideal = 16.47 ± 0.20
50%/50%	44.8 ± 2.69	19.35 ± 1.06	11.55 ± 0.80
C_3H_6/C_3H_8	Ideal = 1.3 ± 0.11	Ideal = 5.71 ± 0.98	Ideal = 2.18 ± 0.44
50%/50%	6.1 ± 2.69	5.15 ± 1.63	1.2 ± 0.14

Table 12.   Young's Modulus and Tensile Strength of ZIF-8/Matrimid® MMMs.

	Young's Modulus	Tensile Strength(MPa)
0%	2.5 ± 0.17	109 ± 3.48
20%	3.5 ± 0.26	98.1 ± 13.35
30%	3.2 ± 0.15	93.4 ± 5.62
40%	3.1 ± 0.06	85.4 ± 11.49
50%	2.9 ± 0.14	67.1 ± 4.97
60%	2.2 ± 0.11	47.6 ± 3.30

Table 13.   Pure gas permeation result of mesoporous ZSM-5/Matrimid® membranes

	Permeability (barrer)[a]					Ideal selectivity				
	H_2	N_2	O_2	CH_4	CO_2	H_2/N_2	O_2/N_2	CO_2/CH_4	H_2/CH_4	H_2/CO_2
pure Matrimid®	17.50	0.22	1.46	0.20	7.29	79.6	6.64	34.71	83.3	2.40
10% meso-ZSM-5	19.78	0.14	1.38	0.12	8.27	142.6	9.97	67.19	160.9	2.39
10% meso-ZSM-5[b]	19.56	0.14	1.35	0.13	8.51	137.8	9.51	63.51	146.0	2.30
20%meso-ZSM-5	22.23	0.17	1.80	0.13	8.65	127.9	10.35	66.07	169.8	2.57
30%meso-ZSM-5	35.37	0.31	2.82	0.26	14.6	106.4	8.49	56.48	136.7	2.42
10% meso-ZSM-5 (uncalcined)	36.31	0.62	3.17	0.56	15.4	58.8	5.14	27.49	64.8	2.36
10% ZSM-5	22.04	0.34	1.70	0.30	9.01	64.8	5.00	30.03	73.5	2.45
10% MCM-48	23.14	0.30	1.94	0.28	9.35	76.1	6.38	33.39	82.6	2.47

[a] 1 Barrer = 10^{-10} cm^3 (STP) cm/cm^2 s cmHg [b] A upstream pressure of 1100 torr

Table 14. Pure gas permeation of carbon aerogel/Matrimid® membranes (35°C)

	Permeability (Barrers)					Ideal selectivity				
	H_2	N_2	O_2	CH_4	CO_2	H_2/N_2	O_2/N_2	CO_2/CH_4	H_2/CH_4	H_2/CO_2
Matrimid®	17.5	0.22	1.46	0.20	7.29	79.6	6.64	34.7	83.3	2.40
10% CA	20.6	0.18	1.68	0.17	7.98	115.8	9.41	47.8	123.6	2.58
10% CA[a]	20.1	0.18	1.65	0.17	7.68	113.2	9.29	46.0	120.6	2.62
20% CA	24.9	0.22	1.95	0.21	9.92	111.0	8.69	47.8	120.1	2.51
30% CA	34.9	0.34	2.86	0.30	13.3	102.0	8.36	45.1	117.8	2.61

[a]: Upstream pressure was 2000 torr. 1 Barrer = 10^{-10} cm^3 (STP) cm/cm^2 s cmHg

Table 15. Gas mixtures separation using 10% carbon aerogel/Matrimid® membrane

Selectivity	Mixture (mol%)	Matrimid®	10 wt% carbon aerogel	
N_2/CH_4	50% CH_4/ 50% N_2	1.11	1.06	Ideal selectivity 1.06
	94% CH_4/ 6% N_2	1.14	1.14	
CO_2/CH_4	50% CO_2/ 50% CH_4	36.3	51.9	Ideal selectivity 46.9
	10% CO_2/ 90% CH_4	35.1	48.4	
H_2/CO_2	75% CO_2/ 25% H_2	2.43	2.54	Ideal selectivity 2.59
	50% CO_2/ 50% H_2	2.56	2.61	

Table 16. Gas mixtures separation using 10% carbon aerogel-zeolite A and zeolite Y-Matrimid® membranes

Gas mixture (Molar ratio)	N_2/CH_4		Ideal selectivity	CO_2/CH_4		Ideal selectivity	H_2/CO_2		Ideal selectivity
	50%:50%	94%:6%		50%:50%	10%:90%		75%:25%	50%:50%	
Matrimid®	1.11	1.14	1.05	36.3	35.1	34.7	2.43	2.55	2.40
10% CA	1.06	1.14	1.06	51.9	48.4	46.9	2.54	2.61	2.59
10% CA-A	1.22	1.31	1.38	67.2	59.5	71.5	2.37	2.39	2.40
10% CA-Y	1.14	1.19	1.16	54.9	53.9	57.4	2.42	2.31	2.62

Table 17. Pure gas permeation of SWNT-short-Matrimid® membranes

	Permeability(Barrers)					Ideal selectivity				
	H_2	N_2	O_2	CH_4	CO_2	H_2/N_2	O_2/N_2	CO_2/CH_4	H_2/CH_4	H_2/CO_2
Matrimid®	11.58	0.11	0.76	0.08	3.45	105.27	69.09	45.39	152.37	3.36
1.25%SWNT-s	14.84	0.17	1.04	0.12	5.15	87.29	61.18	42.92	123.67	2.88
2.2%SWNT-s	16.15	0.18	1.05	0.13	5.00	92.29	60.00	39.68	128.17	3.23
3.2%SWNT-s	17.67	0.18	1.11	0.14	5.61	98.17	61.67	40.95	128.98	3.15
4.9%SWNT-s	19.79	0.19	1.41	0.14	6.95	104.16	74.21	49.64	141.36	2.85

Table 18. Diffusivity and solubility of various gases in the pure Matrimid® and SWNT-COOH-Matrimid® membrane.

	Diffusivity ($\times 10^{-8}$ cm^2/s)					Solubility (cm^3(STP)/cm^3 cm Hg)				
	H_2	N_2	O_2	CH_4	CO_2	H_2	N_2	O_2	CH_4	CO_2
Matrimid®	9.18	0.076	0.24	0.021	0.037	0.013	0.015	0.32	0.038	0.93
1.25 wt%	9.25	0.068	0.21	0.020	0.038	0.013	0.015	0.31	0.040	0.94
4.2 wt%	10.42	0.092	0.28	0.029	0.043	0.013	0.015	0.32	0.041	0.94

Table 19. Gas mixtures separation using SWNT-Matrimid® membrane

Selectivity	Mixture (mol%)	Matrimid®/IS[a]		4.2 wt% SWNT-COOH/ IS[a]		3.2 wt % SWNT-short /IS[a]	
CH$_4$/N$_2$	50% CH$_4$/ 50% N$_2$	0.69	0.73	0.81	0.85	0.71	0.78
	25% CH$_4$/ 75% N$_2$	0.72		0.78		0.77	
CO$_2$/CH$_4$	50% CO$_2$/ 50% CH$_4$	43.3	45.4	38.9	33.7	42.3	41.0
	10% CO$_2$/ 90% CH$_4$	46.2		39.7		43.5	
H$_2$/CO$_2$	75% CO$_2$/ 25% H$_2$	3.41	3.36	3.42	3.38	3.42	3.15
	50% CO$_2$/ 50% H$_2$	3.36		3.46		3.32	

[a] Ideal selectivity

Table 20. Gas mixture separation using 20 wt % Cu-BPY-HFS/Matrimid® membranes (35 ° C).

Selectivity	Mixture (mol%)	Matrimid®	20% Cu-BPY-HFS- Matrimid®	
CH_4/N_2	94% CH_4/ 6% N_2	0.88	1.6	Ideal selectivity
	50% CH_4/ 50% N_2	0.90	1.7	1.16
CO_2/CH_4	50% CO_2/ 50% CH_4	36.3	20.5	Ideal selectivity 27.6
	10% CO_2/ 90% CH_4	35.1	22.5	
H_2/CO_2	50% CO_2/ 50% H_2	2.56	2.6	Ideal selectivity
	75% CO_2/ 25% H_2	2.43	2.4	1.70

Table 21. Gas mixtures separation using 10% carbon aerogel/Matrimid® membrane.

Selectivity	Mixture (mol%)	Matrimid®	10 wt% carbon aerogel	
N_2/CH_4	50% CH_4/ 50% N_2	1.11	1.06	Ideal selectivity
	94% CH_4/ 6% N_2	1.14	1.14	1.06
CO_2/CH_4	50% CO_2/ 50% CH_4	36.3	51.9	Ideal selectivity
	10% CO_2/ 90% CH_4	35.1	48.4	46.9
H_2/CO_2	75% CO_2/ 25% H_2	2.43	2.54	Ideal selectivity
	50% CO_2/ 50% H_2	2.56	2.61	2.59

Table 22. Gas mixtures separation using 10% carbon aerogel-zeolite A and zeolite Y-Matrimid® membranes.

Gas mixture (Molar ratio)	N_2/CH_4 50%:50%	94%:6%	Ideal selectivity	CO_2/CH_4 50%:50%	10%:90%	Ideal selectivity	H_2/CO_2 75%:25%	50%:50%	Ideal selectivity
Matrimid®	1.11	1.14	1.05	36.3	35.1	34.7	2.43	2.55	2.40
10% CA	1.06	1.14	1.06	51.9	48.4	46.9	2.54	2.61	2.59
10% CA-A	1.22	1.31	1.38	67.2	59.5	71.5	2.37	2.39	2.40
10% CA-Y	1.14	1.19	1.16	54.9	53.9	57.4	2.42	2.31	2.62

Table 23. Gas mixtures separation using SWNT-Matrimid® membrane.

Selectivity	Mixture (mol%)	Matrimid®/IS[a]		4.2 wt% SWNT-COOH/ IS[a]		3.2 wt % SWNT-short /IS[a]	
CH$_4$/N$_2$	50% CH$_4$/ 50% N$_2$	0.69	0.73	0.81	0.85	0.71	0.78
	25% CH$_4$/ 75% N$_2$	0.72		0.78		0.77	
CO$_2$/CH$_4$	50% CO$_2$/ 50% CH$_4$	43.3	45.4	38.9	33.7	42.3	41.0
	10% CO$_2$/ 90% CH$_4$	46.2		39.7		43.5	
H$_2$/CO$_2$	75% CO$_2$/ 25% H$_2$	3.41	3.36	3.42	3.38	3.42	3.15
	50% CO$_2$/ 50% H$_2$	3.36		3.46		3.32	

[a] Ideal selectivity

Table 24. Critrical temperature and molecular dimension of gas molecules

Gas molecule	Critical temperature[a] (K)	Kinetic diameter[a] (nm)
H$_2$	32.2	0.289
CO$_2$	304.2	0.330
O$_2$	154.6	0.346
N$_2$	126.2	0.364
CH$_4$	190.6	0.380

Table 25. Pure gas permeability of Cu-BPY-HFS/Matrimid® membranes (35 ° C).

	Permeability(Barrers)					Ideal selectivity					
	H$_2$	N$_2$	O$_2$	CH$_4$	CO$_2$	H$_2$/N$_2$	O$_2$/N$_2$	CO$_2$/CH$_4$	H$_2$/CH$_4$	H$_2$/CO$_2$	CH$_4$/N$_2$
Matrimid®	17.50	0.22	1.46	0.20	7.29	79.55	6.64	34.71	83.33	2.40	0.95
10 wt %	16.91	0.24	1.44	0.24	7.81	71.04	6.04	31.93	69.15	2.17	1.03
20 wt %	16.75	0.31	1.77	0.36	9.88	54.46	5.76	27.62	46.82	1.70	1.16
20 wt %[a]	16.87	0.32	1.81	0.37	10.02	52.72	5.66	27.08	45.59	1.68	1.16
30 wt %	20.34	0.31	1.98	0.38	10.36	65.23	6.33	27.45	53.89	1.96	1.21
40 wt %	26.74	0.49	3.06	0.59	15.06	54.78	6.27	25.55	45.38	1.78	1.21

Table 26. Gas mixture separation using 20 wt % Cu-BPY-HFS/Matrimid® membranes (35 ° C).

Selectivity	Mixture (mol%)	Matrimid®	20% Cu-BPY-HFS- Matrimid®	
CH_4/N_2	94% CH_4/ 6% N_2	0.88	1.6	Ideal selectivity
	50% CH_4/ 50% N_2	0.90	1.7	1.16
CO_2/CH_4	50% CO_2/ 50% CH_4	36.3	20.5	Ideal selectivity 27.6
	10% CO_2/ 90% CH_4	35.1	22.5	
H_2/CO_2	50% CO_2/ 50% H_2	2.56	2.6	Ideal selectivity
	75% CO_2/ 25% H_2	2.43	2.4	1.70

Table 27. Pure gas permeability data of Matrimid® containing PMOs with different loadings (under 35 °C)

	Permeability(Barrers)					Ideal selectivity			
	H_2	N_2	O_2	CH_4	CO_2	H_2/N_2	O_2/N_2	CO_2/CH_4	N_2/CH_4
pure Matrimid®	17.5	0.22	1.46	0.21	7.29	79.55	6.64	34.71	1.05
10% MBS	26.54	0.32	2.55	0.24	13.83	82.94	7.97	57.63	1.33
20% MBS	36.33	0.52	2.96	0.40	16.35	69.87	5.69	40.88	1.30
30% MBS	40.12	0.63	3.57	0.46	19.99	63.68	5.67	43.46	1.37
10% ethenylene	21.62	0.28	1.68	0.24	8.86	77.21	6.00	36.92	1.17
10% phenylene silica	26.12	0.31	2.04	0.27	11.21	84.26	6.58	41.52	1.15
10% ethylene silica	38.54	0.46	3.01	0.39	15.01	83.78	6.54	38.49	1.18
10% methylene silica	35.1	0.43	2.78	0.37	14.2	81.63	6.47	38.38	1.16

Table 28. Diffusivity and solubility of various gases in the pure MBS/Matrimid® membranes.

Loading	Diffusivity ($\times 10^{-10}$ cm^2/s)					Solubility (cm^3(STP)/cm^3 cm Hg)			
	0%	10%	20%	30%		0%	10%	20%	30%
H_2	1884	2323	2489	3650	H_2	0.009	0.009	0.010	0.010
O_2	46.5	74.9	89.8	105.1	O_2	0.032	0.034	0.033	0.034
CO_2	22.1	32.0	36.1	40.3	CO_2	0.329	0.431	0.454	0.495
N_2	14.12	21.40	30.60	31.52	N_2	0.015	0.015	0.017	0.020
CH_4	4.87	5.58	9.62	9.87	CH_4	0.042	0.043	0.042	0.047
	Diffusivity selectivity					Solubility selectivity			
Loading	0%	10%	20%	30%		0%	10%	20%	30%
H_2/N_2	133.4	108.5	81.3	115.8	H_2/N_2	0.61	0.63	0.57	0.48
CO_2/CH_4	4.5	5.7	3.8	4.1	CO_2/CH_4	7.81	10.02	10.81	10.53
O_2/N_2	3.3	3.5	2.9	3.3	O_2/N_2	2.06	2.27	1.94	1.70

Table 29. Gas mixtures separation using 10% MBS/Matrimid® membrane.

Selectivity	Mixture (mol%)	Matrimid®	10 wt% MBS	
N_2/CH_4	50% CH_4/ 50% N_2	1.11	1.14	Ideal selectivity
	94% CH_4/ 6% N_2	1.14	1.17	1.23
CO_2/CH_4	50% CO_2/ 50% CH_4	36.3	47.3	Ideal selectivity
	10% CO_2/ 90% CH_4	35.1	46.2	57.6
H_2/CO_2	75% CO_2/ 25% H_2	2.43	2.39	Ideal selectivity
	50% CO_2/ 50% H_2	2.56	2.52	2.55

REFERENCES

1.   Huang, L.; Wang, H.; Chen, J.; Wang, Z.; Sun, J.; Zhao, D.; Yan, Y., "Synthesis, morphology control, and properties of porous metal–organic coordination polymers", *Microporous and Mesoporous Materials* **2003**, 58, 105.

2.   Li, H.; Eddaoudi, M.; O'Keeffe, M.; Yaghi, O. M., "Design and synthesis of an exceptionally stable and highly porous metal-organic framework", *Nature* **1999**, 402, 276.

3.   Mueller, T.; Schubert, M.; Teich, F.; Puetter, H.; Schierle-Arndt, K.; Pastre, J., "Metal-organic-frameworks-prospective industrial applications", *Journal of Materials Chemistry* **2005**, 16, 626.

4.   Seki, K., "Design of an adsorbent with an ideal pore structure for methane adsorption using metal complexes", *Chemical Communications* **2001**, 1496.

5.   Seki, K.; Mori, W., "Syntheses and characterization of microporous coordination polymers with open frameworks", *J. Phys. Chem. B* **2002**, 106, 1380.

6.   Mori, W.; Inouet, F.; Yoshida, K.; Nakayama, H.; Takamizawa, S.; Kishitat, M., "Synthesis of new adsorbent copper(II) terephthalate", *Chemistry Letters* **1997**, 26, 1219.

7.   Furukawa, H.; Kim, J.; Plass, K. E.; Yaghi, O. M., "Crystal structure, dissolution, and deposition of a 5 nm functionalized metal-organic great rhombicuboctahedron", *Journal of the American Chemical Society* **2006**, 128, 8398.

8.   Xia, Y.; Mokaya, R., "Are mesoporous silicas and aluminosilicas assembled from zeolite seeds inherently hydrothermally stable? Comparative evaluation of MCM-48 materials assembled from zeolite seeds", *Journal of Materials Chemistry* **2004**, 14, 3427.

9.   Li, W.-C.; Lu, A.-H.; Weidenthaler, C.; Schuth, F., "Hard-templating pathway to create mesoporous magnesium oxide", *Chemistry of Materials* **2004**, 16, 5676.

10.   Vankelecom, I. F. J.; Dotremont, C.; Morobe, M.; Uytterhoeven, J. B.; Vandecasteele, C., "Zeolite-filled PDMS membranes. 1. Sorption of halogenated hydrocarbons", *The Journal of Physical Chemistry B* **1997**, 101, 2154.

11.   Inagaki, S.; Guan, S.; Ohsuna, T.; Terasaki, O., "An ordered mesoporous organosilica hybrid material with a crystal-likewall structure", *Nature* **2002**, 416, 304.

12.   Burleigh, M. C.; Jayasundera, S.; Thomas, C. W.; Spector, M. S.; Markowitz, M. A.; Gaber, B.

P., "A versatile synthetic approach to periodic mesoporous organosilicas", *Colloid. Polym. Sci.* **2004**, 282, 728.

13. Reid, B. D.; Ruiz-Trevino, F. A.; Musselman, I. H.; Balkus Jr., K. J.; Ferraris, J. P., "Gas permeability properties of polysulfone membranes containing the mesoporous molecular sieve MCM-41", *Chemistry of Materials* **2001**, 13, 2366.

14. Riley, S. Gas permeability and selectivity studies of pure poly(3-[2,5,8-trioxynonyl]thiophene), PTONT, and PTONT/poly(ethylene oxide) polymer blend membranes. Ph.D. Dissertation, The University of Texas at Dallas, Richardson, TX, 2000.

15. Rong, M. Z.; Zhang, M. Q.; Zheng, Y. X.; Zeng, H. M.; Walter, R.; Friedrich, K., "Structure-property relationships of irradiation grafted nano-inorganic particle filled polypropylene composites", *Polymer* **2001**, 42, 167.

16. Zhang, M. Q.; Rong, M. Z.; Zhang, H. B.; Friedrich, K., "Mechanical properties of low nano-silica filled high density polyethylene composites", *Polymer Engineering and Science* **2003**, 43, 490.

17. Zhang, M.; Rong, M.; Friedrich, K., Application of non-layered nanoparticles in polymer modification. In *Polymer Composites*, Springer US: 2005; pp 25.

18. Vu, D. Q.; Koros, W. J.; Miller, S. J., "Mixed matrix membranes using carbon molecular sieves: I. Preparation and experimental results", *Journal of Membrane Science* **2003**, 211, 311.

19. Skoulidas, A. I.; Sholl, D. S., "Self-diffusion and transport diffusion of light gases in metal-organic framework materials assessed using molecular dynamics simulations", *J. Phys. Chem. B* **2005**, 109, 15760.

20. Yaghi, O. M.; Rosi, N. L.; Eckert, J.; Eddaoudi, M.; Vodak, D. T.; Kim, J.; O'Keeffe, M., "Hydrogen storage in microporous metal-organic frameworks", *Science* **2003**, 300, 1127.

21. Koros, W. J., "Model for sorption of mixed gases in glassy polymers", *Journal of Polymer Science: Polymer Physics Edition* **1980**, 18, 981.

22. Dhingra, S. S.; Marand, E., "Mixed gas transport study through polymeric membranes", *Journal of Membrane Science* **1998**, 141, 45.

23. Hafizovic, J.; Bjorgen, M.; Olsbye, U.; Dietzel, P. D. C.; Bordiga, S.; Prestipino, C.; Lamberti, C.; Lillerud, K. P., "The inconsistency in adsorption properties and powder XRD data of MOF-5 is rationalized by framework interpenetration and the presence of organic and inorganic species

in the nanocavities", *Journal of the American Chemical Society* **2007**, 129, 3612.

24.   Millward, A. R.; Yaghi, O. M., "Metal-organic frameworks with exceptionally high capacity for storage of carbon dioxide at room temperature", *Journal of the American Chemical Society* **2005**, 127, 17998.

25.   Eddaoudi, M.; Kim, J.; Rosi, N.; Vodak, D.; Wachter, J.; O'Keeffe, M.; Yaghi, O. M., "Systematic design of pore size and functionality in isoreticular MOFs and their application in methane storage", *Science* **2002**, 295, 469.

26.   Armatas, G. S., "Determination of the effects of the pore size distribution and pore connectivity distribution on the pore tortuosity and diffusive transport in model porous networks", *Chemical Engineering Science* **2006**, 61, 4662.

27.   Snyder, M. A.; Lai, Z.; Tsapatsis, M.; Vlachos, D. G., "Combining simultaneous reflectance and fluorescence imaging with SEM for conclusive identification of polycrystalline features of MFI membranes", *Microporous and Mesoporous Materials* **2004**, 76, 29.

28.   Bonilla, G.; Tsapatsis, M.; Vlachos, D. G.; Xomeritakis, G., "Fluorescence confocal optical microscopy imaging of the grain boundary structure of zeolite MFI membranes made by secondary (seeded) growth", *Journal of Membrane Science* **2001**, 182, 103.

29.   Park, K. S.; Ni, Z.; Cote, A.; Choi, J. Y.; Huang, R.; Uribe-Romo, F.; Chae, H.; O'Keefe, M.; Yaghi, O., "Exceptional chemical and thermal stability of zeolitic imidazolate frameworks", *Proc. Nat. Acad. Sci. USA* **2006**, 103, 10186.

30.   Saini, A. K.; Carlin, C. M.; Patterson, H. H., "Confirmation of the presence of imine bonds in thermally cured polyimides", *J. Polym. Sci. Part A: Polym Chem.* **1993**, 31, 2751.

31.   Merkel, T. C.; Freeman, B. D.; Spontak, R. J.; He, Z.; Pinnau, I.; Meakin, P.; Hill, A. J., "Ultrapermeable, reverse-selective nanocomposite membranes", *Science* **2002**, 296, 519.

32.   Moore, T. T.; Mahajan, R.; Vu, D. Q.; Koros, W. J., "Hybrid membrane materials comprising organic polymers with rigid dispersed phases", *AlChE* **2004**, 50, 311.

33.   Sterescu, D. M.; Stamatialis, D. F.; Wessling, M., "Boltron-modified polyimide gas separation membranes", *J. Membr. Sci.* **2008**, 310, 512.

34.   Suer, A. K.; Bac, N.; Yilmaz, L., "Gas permeation characteristics of polymer-zeolite mixed matrix membranes", *J. Membr. Sci.* **1994**, 91, 77.

35. Vu, D. Q.; Koros, W. J.; Miller, S. J., "High pressure CO_2/CH_4 separation using carbon molecular sieve hollow fiber membranes", *Ind. Eng. Chem. Res.* **2002**, 41, 367.

36. Zhang, M.; Rong, M.; Friendrich, K., *Polymer Composites: From Nano-to-Macro-Scale*. 2005; Vol. 22.

37. Mahajan, R.; Koros, W. J., "Factors controlling successful formation of mixed-matrix gas eparation materials", *Ind. Eng. Chem. Res.* **2000**, 39, 2692.

38. Jia, M. D.; Peinemann, K. V.; Behling, R. D., "Molecular sieving effect of the zeolite-filled silicone rubber membranes", *J. Membr. Sci.* **1991**, 57, 289.

39. Guliants, V. V.; Carreon, M. A.; Lin, Y. S., "Ordered-mesoporous and macroporous inorganic films and membranes", *J. Membr. Sci.* **2004**, 235, 53.

40. Lai, R.; Gavalas, G. R., "ZSM-5 synthesis with organic-free mixtures", *Micropor. Mesopor. Mater* **2000**, 38, 239.

41. Karger, J.; Ruthven, D. M., *Diffusion in zeolites and other microporous solids*. Wiley/Interscience, New York: 1992.

42. Jia, M. D.; Peinemann, K. V.; Behling, R. D., "Preparation and characterization of thin-film zeolite-PDMS composite membranes", *J. Membr. Sci.* **1992**, 73, 119.

43. Kim, G.-M.; Michler, G. H.; Gahleitner, M.; Fiebig, J., "Relationship between morphology and micromechanical toughening mechanisms in modified polypropylenes", *J. Appl. Polym. Sci.* **1996**, 60, 1391.

44. Pukanszky, B., "Influence of interface interaction on the ultimate tensile properties of polymer composites", *Composites* **1990**, 21, 255.

45. Stern, S. A., "Polymers for the gas separation: the next decade", *J. Membr. Sci.* **1994**, 94, 1.

46. Koros, W. J.; Mahajan, R. J., "Pushing the limits on possibilities for large scale gas separation: which strategies?" *J. Membr. Sci.* **2000**, 175, 181.

47. Koros, W. J.; Fleming, G. K., "Membrane-based gas separation", *J. Membr. Sci.* **1993**, 83, 1.

48. Kim, S.; Pechar, T. W.; Marand, E., "Poly(imide siloxane) and carbon nanotube mixed matrix membrane for gas separation", *Desalination* **2006**, 192, 330.

49. Kim, S.; Pechar, T. W.; Marand, E., "Polysulfone and functionalized crbon nanotube mixed matrix membranes for gas separation: Theory and experiment", *J. Membr. Sci.* **2006**, 294, 147.

50. Iijima, S., "Helical microtubules of graphitic carbon", *Nature* **1991**, 354, 56.

51. Wang, H.; Holmberg, B. A.; Yan, Y., "Homogeneous polymer-zeolite nanocomposite membranes by incorporating dispersible template-removed zeolite nanocrystals", *J. Mater. Chem.* **2002**, 12, 3640.

52. Jiang, L.; Chung, T.; Huang, Z.; Kulprathipanja, S., "Fundamental understanding of nano-sized zeolite distribution in the formation of the mixed matrix single- and dual-layer asymmetric hollow fiber membranes", *J. Membr. Sci.* **2005**, 252, 89.

53. Koros, W. J.; Coleman, M. R.; Walker, D. R. B., "Controlled permeability polymer membranes", *Annu. Rev. Mater. Sci.* **1992**, 22, 47.

54. Wang, Q. Y.; Challa, S. R.; Scholl, D. S.; Johnson, J. K., "Quantum sieving in carbon nanotubes and zeolites", *Phys. Rev. Lett.* **1999**, 82, 956.

55. Hummer, G.; Rasaiah, J. C.; Noworyta, J. P., "Water conduction through the hydrophobic channel of a carbon nanotube", *Nature* **2001**, 414, 188.

56. Yanag, H.; Sawada, E.; Manivannan, A.; Nagahara, L. A., "Self-oriented of short single-walled carbon nanotubes deposited on graphite", *Applied Physics Letters* **2001**, 78, 1355.

57. Liu, J.; Rinzler, A. G.; Dai, H.; Hafner, H. J.; Bradley, R. K.; Boul, P. J.; Lu, A.; Iverson, T.; Shelimov, K.; Huffman, C. B.; Rodriguez-Macias, F.; Shon, Y. S.; Lee, T. R.; Colbert, D. T.; Smalley, R. E., "Fullerene Pipes", *Science* **1998**, 280, 1253.

58. Skoulidas, A. I.; Ackerman, D. M.; Johnson, J. K.; Scholl, D. S., "Rapid transport of gases in carbon nanotubes", *Phys. Rev. Lett.* **2002**, 89, 185901.

59. Holt, J. K.; Park, H. G.; Wang, Y.; Stadermann, M.; Artyukhin, A.; Grigoropoulos, C.; Noy, A.; Bakajin, O., "Fast mass transport through sub-2-nanometer carbon nanotubes", *Science* **2006**, 312, 1034.

60. Hinds, B. J.; Chopra, N.; Rantell, T.; Andrews, R.; Gavalas, V.; Bachas, L., "Aligned multiwalled carbon nanotube membranes", *Science* **2004**, 303, 62.

61. Chen, H.; Scholl, D. S., "Predictions of selectivity and flux for CH4/H2 separations using single walled carbon nanotubes as membranes", *J. Membr. Sci.* **2006**, 269, 152.

62.   Chen, H.; Scholl, D. S., "Rapid diffusion of CH4/H2 mixtures in single-walled carbon nanotubes", *J. Am. Chem. Soc.* **2004**, 126, 7778.

63.   Ackerman, D. M.; Skoulidas, A. I.; Scholl, D. S.; Johnson, J. K., "Diffusivities of Ar and Ne in carbon nanotubes", *Mol. Sim.* **2003**, 29, 677.

64.   Paul, D. R.; Yampol'skii, Y. P., CRC Press: Florida, 1994.

65.   Hennepe, H. J. C. t.; Boswerger, W. B. F.; Bargeman, D.; Mulder, M. H. V.; Smolders, C. A., "Zeolite-filled silicone rubber membranes experimental determination of concentration properties", *J. Membr. Sci.* **1994**, 89, 185.

ACRONYMS AND ABBREVIATIONS

θ	Time lag
amu	Atomic mass unit
ATR	Attenuated total reflectance
BET	Brunauer-Emmett-Teller surface area
BPDA	Biphenyl-4,4'-dicarboxylic acid
BTEB	Bis(triethoxysilyl)methylene
CTABr	Cetyltrimethylammonium bromide
Cu-BPY-HFS	Copper(II) bipyridine hexafluorosilicate metal-organic framework
Cu-MOF	Copper(II) biphenyldiacetate triethylenediamine metal-organic framework
D	Diffusivity
DI	Deionized water
DMA	Dynamic mechanical analysis
DMF	Dimethylformamide
DSC	Differential scanning calorimetry
FEG	Field emission gun
FTIR	Fourier transform infrared
HK	Horvath-Kawazoe pore size
H-MeIM	Methylimidazolate
L	Thickness
MBS	Mesoporous benzene silica
MMM	Mixed-matrix membrane
MOF-5	Metal-organic framework 5
MOP-18	Metal-organic polyhedra 18
NMP	N-methylpyrrolidone
ODTMA	Octadecyltrimethylammonium chloride
P	Permeability
PDMS	Polydimethylsiloxane
PMO	Periodic mesoporous organosilicas
RGA	Residual gas analyzer
RT	Room temperature
S	Solubility
SBU	Secondary building unit
SEM	Scanning electron microscope
SWNT	Single-walled carbon nanotube
SWNT-COOH	Carboxylated single-walled carbon nanotube
TCE	1,1,2,2-tetrachloroethane
TEA	triethylamine
TED	Triethylenediamine
TGA	Thermogravimetric analysis

TPAOH	Tetrapropylammonium hydroxide
XRD	X-ray diffraction
ZIF-8	Zeolitic imidazolate framework 8